Functional Nanocomposites Formed by Two-step Back-filling Methods

Theodore J. Kramer

Submitted in partial fulfillment of the
requirements for the degree of
Doctor of Philosophy
in the Graduate School of Arts and Sciences

COLUMBIA UNIVERSITY

2013

Abstract

Functional Nanocomposites Formed by Back-filling Methods

Theodore J. Kramer

This thesis investigates the synthesis and properties of nanocomposite materials comprised of inorganic nanocrystals (NCs) combined with a complementary organic compound utilizing sequential two-step synthesis methods. We demonstrate an enhancement in the mechanical and optical properties of electrophoreticially deposited (EPD) cadmium selendide (CdSe) nanocrystal (NC) films through post-deposition addition of organic ligand molecules and polymeric precursor molecules (monomers). Specifically we show that when these organic compounds are added (i.e. back-filled) into the as-deposited, wet EPD NC film, that fracture in the dried film is suppressed and photoluminscent (PL) efficiency of the inorganic NC phase is greatly increased. We go on to study the synthesis and properties of a novel nanocomposite comprised of inorganic NCs back-filled into a mat of semiconducting poly(3-hexylthiophene) [P3HT] nanowires. P3HT nanowire films are synthesized using a novel method developed as part of this thesis; where P3HT is blended with a sacrificial polymer (polystyrene, PS), leading to spontaneous demixing of the two polymers upon casting, and upon selective removal of the PS phase exposes a dense mat of P3HT nanowires. When back filled with CdSe NCs the composite material exhibits photovoltaic (PV) performance and provides a flexible platform for low-cost, hybrid organic/inorganic NC PV device fabrication. We conclude by showing how the above methods, in conjunction with novel ligand chemistry and lithographic techniques, can be utilized to create a photo-active nanocomposite consisting of lithographically defined, micron-scale, electrodes that are selectively decorated with electron-accepting NCs using EPD, and subsequently back-filled with a complementary electron-donating NC phase. The device architecture and resulting nanocomposite material is capable of lateral exciton separation on a potentially low-cost substrate.

Table of Contents

List of Figures

Acknowledgments

I would like to thank all the individuals in my life that have helped me to complete this thesis. While much of the work was a personal endeavor, I relied constantly on the support of my friends and family to maintain a positive outlook on the daunting task at hand.

Of the many individuals at Columbia University who provided me with professional guidance, technical assistance, and financial support, I want to express particular thanks to my thesis advisor, Prof. Irving P. Herman. Prof. Herman has been tireless in his efforts to guide me in research, improve my scientific understanding, and to make me an effective scientific researcher. Without his support this thesis would not have been possible.

Members of the Herman group have also been critical to my success. My early work in the synthesis of nanocrystals and electrophoretic deposition was carried out under the patient guidance of Dr. Shennguo Jia. As I progressed in my research, I was immensely fortunate to have Dr. Chenguang Lu available to learn from and to teach me much of what I now know about nanocrystal synthesis and chemistry. I owe to Dr. Austin Akey my gratitude for training me to use many of the instruments used in this research, and for generally being a friend, lab mate, and endless source of miscellaneous knowledge. Fellow Ph.D. candidate Dae Kim has been welcome company on late nights in lab and was instrumental in the fabrication of the interdigitated electrode arrays presented in Chapter 6. Of the many undergraduate students with whom I worked, I want give particular credit to Annabel Chew for her intelligence, positive attitude, and determined work ethic; all of which contributed to the work presented in Chapter 5.

Other individuals within the Columbia University community have also played a crucial role in my research. One of the earliest contributors to the direction of this thesis was Dr. Michael L. Steigerwald of the Chemistry Department. It was a suggestion made by Dr. Steigerwald during the defense of a previous student that originally led to the concept of stabilizing EPD NC films through

infusion of a secondary compound. Prof. Ioannis Kymissis of the Electrical Engineering Department deserves special thanks for his technical expertise in the field of organic photovoltaics and his professional guidance throughout my time at Columbia. I also appreciate the valuable discussions with Prof. Sanat K. Kumar of the Chemical Engineering Department on the subject of polymer-stabilization of EP NC films. Prof. Jon Owen of the Chemistry Department was kind enough to provide NC samples used in Chapter 6. Finally, a personal thanks to Dr. Theanne Schiros, who has been both a friend and an invaluable collaborator in the area of material characterization using wide-angle x-ray scattering.

This work was supported by the National Science Foundation's Materials Research Science and Engineering Center at Columbia University (DMR-0213574), and the Department of Energy's Energy Frontiers Research Center at Columbia University (DE-SC0001085), and by the New York State Office of Science, Technology, and Academic Research.

Finally, I would like to pay homage to the great City of New York, the back-drop for the past six years of my life. At the best moments New York City has been a wonderful place to celebrate my successes, and at the lowest points it has provided me with the friends and adventures needed for me to escape and recover. While I may move on, I never expect to live in such a wonderful and dynamic city.

Publications of Theodore J. Kramer

[1] T. J. Kramer, A. R. Chew, T. Schirros, I. Kymissis, and I. P. Herman, *P3HT Nanowire Networks for Versatile Fabrication of Bulk Heterojunctions with Increased Active Volume*, Journal of Vac. Sci. & Tech. B (2013), **31**, 031209

[2] T. J. Kramer, S. K. Kumar, M. L. Steigerwald, and I. P. Herman, *Reducing Strain and Fracture of Electrophoretically Deposited CdSe Nanocrystal Films. I. Postdeposition Infusion of Capping Ligands*, J. Phys. Chem. B (2012), **117**, 1537

[3] T. J. Kramer, S. K. Kumar, M. L. Steigerwald, and I. P. Herman, *Reducing Strain and Fracture of Electrophoretically Deposited CdSe Nanocrystal Films. II. Postdeposition Infusion of Monomers*, J. Phys. Chem. B (2012), **117**, 1544

[4] T. J. Kramer, S. S. Babu, A. Saeki, S. Seki, J. Aimia and T. Nakanishi, *CdSe Nanocrystal/C60-liquid composite material with enhanced photoelectrochemical performance*, J. Mat. Chem. (2012), **22**, 42, 22370

[5] T. Schiros, S. Mannsfeld, C. Chiu, K. G. Yager, J. Ciston, A. A. Gorodetsky, M. Palma, Z. Bullard, T. Kramer, D. Delongchamp, D. Fischer, I. Kymissis, M. F. Toney, and C. Nuckolls, *Reticulated Organic Photovoltaics*, Adv. Funct. Mater. (2012), **22**, 1167

For my friends and family

1 Introduction and Background to Nanomaterials

Nanotechnology, defined as the design and study of physical systems with dimensions of less than 100 nm, is relatively new to the field of science. Driving the pursuit of nanotechnology is the desire by man-kind to harness and understand the unique properties of such small structures. At the nanometer scale it is possible to create materials that by virtue of their reduced volume and exceedingly high surface area exhibit high chemical activity useful for catalysis, excellent mechanical reinforcement (i.e. nanocomposites), and unique optoelectronic properties resulting from quantum confinement.

1.1 Historical Perspective on Nanotechnology

Although humans have only recently begun to scientifically explore the utility of nanotechnology, nature has utilized nanoscale structures for millions of years. The role of nanoscale structures in nature can be found throughout all stages of biological life; ranging from DNA-based reproduction to infection and death by virus, with all intervening life being sustained by photosynthesis made possible by naturally occurring nanoscale complexes.

One of the oldest examples of observed quantum confinement is the coloration of stained glass using noble metal NPs. In the First Century early glassmakers (without knowing it) utilized the phenomenon of discrete excited plasmon resonances at nanoscale metal-dielectric interfaces to tailor the optical absorption of stained glass. The art of producing stained glass was perfected in the middle ages but the nature of optical absorption in the material remained unknown.

In the early 20th Century scientists developed the mathematical understanding and experimental capabilities to predict and study the behavior of nanoscale systems. Newly emerging theories in quantum mechanics, electromagnetism, and statistical mechanics made it clear that

nanoscale materials possess unique physical properties. However the field of nanotechnology was constrained by a lack of experimental tools for characterization of nanoscale materials. This began to change in the 1930s with the advent of the electron microscope. After several years of improvement Ernst Ruska at the University of Berlin was able to demonstrate sub-100 nm resolution using a transmission electron microscope, beginning the era of electron microscopy. Over the subsequent 50 years a wide variety of nanoscale structures were discovered and investigated, eventually leading to the discovery of carbon nanotubes, the C_{60} molecule, and various other nanomaterials with previously unexplored properties.

However, it was only through advances in materials synthesis occurring in the 1980s did nanotechnology emerge as a robust discipline including theory, synthesis, and characterization. For the past three decades scientist and engineers have utilized these tools to predict and deliberately engineer materials with precision currently reaching the atomic scale.

Today nanotechnology is one of the most widely studied and utilized subjects in the field of modern science. The most visible example of nanotechnology is the modern integrated circuit: nanoscale transistors and random-access memory arrays are now fabricated with dimensions of less than 20 nm and at densities exceeding 10^8 devices per square centimeter. It is difficult to find an aspect of human society that has not been revolutionized by the development of these fantastically advanced nanoscale machines. Although less obvious, the impact of nanotechnology on fields as diverse as medicine, energy, transportation, and warfare has also changed forever the way humans live and die.

It is therefore not surprising that the study of nanotechnology is preeminent in the academic fields of physics, chemistry, and engineering. Colloidal chemistry in particular has proven a rich subject in which a steady stream of previously unobserved nanoclusters and nanocrystals are

constantly created. Modern engineering has been similarly prolific in generating new nanomaterials through the development of processing techniques such as chemical vapor deposition (CVD), molecular beam epitaxy (MBE), and electron-beam lithography. Complementing the creation of each new nanomaterial is an ever-expanding suite of nanoscale characterization techniques such as scanning-tunneling microscopy (STM), wide-angle x-ray scattering (WAXS), and nanoindentation. The interpretation of results from these advanced characterization techniques rely heavily on theories developed in solid-state physics, optics, and quantum mechanics. Although much work remains to be done, the field of nanotechnology has now reached a relatively mature state that extends beyond academia and is now finding industrial application.

1.2 "Bottom-up" vs. "Top-down" Nanoscale Design

Nanoscale engineering can roughly divided into two approaches: one in which the nanostructure(s) are fabricated by deliberate (and commonly sequential) placement of material, with attention to the absolute position of the resulting nanoscale structures, while the other entails a process in which nanoscale structures evolve through the spontaneous assembly of matter under carefully chosen environmental conditions. The former is called a "top-down" approach to nanoscale engineering while the latter is called "bottom-up" nanoscale engineering.

Top-down nanoscale fabrication methods are frequently employed when each individual device or structure has a high value (if only to the scientific community). Such is the case in many academic applications, as well as the modern integrated circuit industry. In both cases it is common to employ time consuming and expensive techniques such as high-vacuum deposition, electron beam writing, or reactive ion etching. The reward for this expenditure of time, money, and effort are one or more nanostructures that are reliably located and possess properties determined precisely by the fabrication process employed.

More commonly however, such expenditure of time and effort on individual nanostructures is impractical. Despite the many physical advantages of utilizing nanostuctures in applications such as catalysis or mechanical reinforcement, it is only through the collective performance of billions upon billions of such nanoscale structures that it is possible to achieve an aggregate performance that surpasses the existing (and highly optimized) micro and macroscopic technology. Bottom-up fabrication methods address the need to rapidly and economically create nanoscale systems in a massively parallel manner by harnessing the natural tendency of many materials to self-organize at the nanoscale provided the appropriate conditions. Some of the best examples of bottom-up nanoscale engineering can be found in nature: the spontaneous yet highly accurate folding of proteins and enzymes is accomplished by the appropriate interaction of amino acid sequence, pH, and temperature. Similarly humans can harness and direct nanoscale bottom-up assembly of matter through manipulation of parameters such as elemental composition (spinodal decomposition of alloys), vapor pressure (self-assembly of nanocrystal superlattices), or magnetic fields (alignment of ferromagnetic nanoforests).

In this thesis several strategies for bottom-up and top-down assembly of nanostructures are explored, with an emphasis on utilizing two-step back-filling methods to rationally control the location and morphology of NC/organic interfaces and the overall structure of the composite material. By employing sequential processing steps, both bottom-up and top-down fabrication techniques can be used to create nanocomposite materials with a range of novel and useful properties. Bottom-up methods discussed will include EPD of CdSe NCs (Chapters 3 – 4) and growth of organic nanowires through spontaneous demixing of polymers (Chapter 5). In Chapter 6 we will show that top-down lithographic techniques can be used to control the structure of a nanocomposite structure with micron-scale precision, while EPD is again used for nanoscale

bottom up assembly of NCs. Relevant to each of the above studies will be the use of NC synthesis methods that are bottom-up in nature and enable molecular-level control of the NC/organic interface through use of small organic ligands.

1.3 Inorganic Nanoparticles

Inorganic nanoparticles (NPs) are an important category of nanotechnology and exemplify the ability of nanotechnology to bridge the gap between chemistry (the rational design of molecules) and engineering (the rational design of micro and macroscopic structures). The design and characterization of NPs has been an area of prolific experimentation over the past two decades because it has allowed researchers to probe the behavior of materials that have composition and structure similar to that of bulk materials which exhibit spatial localization traditionally found only in molecular structures. NPs can range in size from ~ 1 nm up to 100 nm and exhibit physical properties that are a function of size, shape, and composition. When a NP has a crystalline core it is typically called a nanocrystal (NC), a particularly common designation when discussing crystalline semiconducting NPs.

As described above, the fabrication of NPs can be accomplished using top-down as well as bottom-up techniques. Top-down synthesis of NPs typically utilizes lithographic techniques in conjunction with a material deposition technique such as electron-beam evaporation to yield "quantum dots" on a planar surface. Quantum dots (QDs) have proven useful for scientific studies by virtue of their fixed spatial location and the absence of surface ligands. The primary drawback to top-down synthesis of QDs is the relatively low throughput of their production: to generate the lithographic pattern needed for one billion 5 nm diameter QDs it would take over ten days using a current state-of-the-art electron beam writer. By contrast, using bottom-up techniques based on

spontaneous de-wetting of a continuous thin film from a substrate can produce QDs in large numbers, but without precise spatial control of QD location.

Alternatively, NPs can be made in much larger numbers through bottom-up solution-phase ("wet") chemistry. Using solution-phase techniques it is common to synthesize up to 10^{17} NPs per milliliter of reaction solution for volumes as large as 1000 ml per synthesis.[1] By appropriate selection of precursor concentration, temperature, and surfactant the size, shape, and composition of NPs can be precisely controlled. As will be discussed in detail later, organic surfactants comprise an important component of the reaction mixture; serving to direct NP growth and prevent individual NPs from aggregating. The presence of these surfactant molecules ("ligands") at the NP surface can have a variety of consequences that influence NP solubility, charge transfer phenomenon, as well as NP mobility during various deposition techniques.

Solution-processed inorganic NPs are one of the most important and well-studied types of nanomaterial by virtue of their facile synthesis, stability, and the ability to precisely control many of their physical characteristics. These qualities have facilitated a wide range of studies exploring the optical, electronic, and magnetic properties of NPs. Many such studies have revealed novel properties that emerge in nanoscale particles by virtue of their reduced size and high surface area.[2-4] Of particular scientific interest are the optical, magnetic, and mechanical properties of crystalline NPs (NCs).

1.3.1 Quantum Confinement in Semiconducting Nanocrystals

In order to motivate the discussion of quantum confinement in nanocrystals (NCs), it is first useful to discuss the properties of a bulk semiconductor. A bulk semiconductor is crystalline by definition (crystal symmetry being a fundamental aspect of a "bandgap"), and its electronic band structure is a function of the "unit cell", the smallest volume-filling repeat unit of the crystalline

lattice structure. Properties such as bandgap, direct vs. indirect band transitions, and effective carrier mass can all be predicted by consideration of the unit cell (geometry, symmetry, composition, etc.) assuming that the unit cell is repeated an infinite number of times in all directions. Applying this bulk assumption, the energetic distribution of excited states, called the density of states (DOS), in a bulk semiconductor needs only to satisfy the diffraction criteria of the Brillouin zone corresponding to a single unit cell (i.e. must exhibit constructive interference with its self upon reflection from the Brillouin zone boundary). Provided this criterion is met, upon sufficient thermal or optical excitation an electron will be promoted from the valence band to the conduction band (leaving behind a "hole" in the valence band) and become spatially delocalized over many unit cells. The physical extent of this delocalization, called the Bohr radius (a_0), is described by the equation $a_o = \frac{4\pi\epsilon_o\hbar^2}{m_e e^2}$, where m_e is the effective mass of the electron in that material. Depending on the material, the Bohr radius may be several nanometers in size; sufficiently large that Coulombic interactions between the electron and hole effectively vanish.

According to quantum mechanics, the wavefunction (Ψ_i) of an electron will possess an energy described by the eigenstates (E_i) of the Schrodinger Equation ($H\Psi_i = E_i\Psi_i$) where H is the Hamiltonian. Assuming tight binding (i.e. expansion of the eigenvalue equation about a central nucleus) and utilizing the linear combination of atomic orbitals (LCAO) model the wave function wave function for an electron can be expressed as $\psi(r) = \sum_j c_j \phi_j(r - R_j)$ and where the Hamiltonian is given by $H_{ij} = \langle \phi_i | H \phi_j \rangle$.[5] When an electron in a NC is excited such that its characteristic wave function is larger in extent than the physical size of the NC it becomes possible to observe "quantum confinement" phenomena.

Due to its size, a NC may consist of only several dozen unit cells, and as a result the DOS in a NC can be different than those of the equivalent bulk material. Unlike a bulk material, an excited

electron in a NC must simultaneously satisfy the diffraction criteria of the unit cell Brillouin zone as well as the physical boundary conditions of the NC itself. Simply put, the wave function of the excited state must exhibit a node at the outer limit of the NC (i.e. cannot exist outside of the material). As a material becomes nanoscale in one or more dimension there arise a finite and energetically distinct set of electronic states that simultaneously satisfy the diffraction requirements of the Brillouin zone and the boundary conditions of the nanoscale material volume. Such is the case for 2-D quantum wells ($2D: \rho \propto E^0$), 1-D quantum wires ($1D: \rho \propto E^{-1/2}$), and 0-D NPs [$0D: \rho \propto \delta(E)$], where E is the energy of the electron, ρ is the density of states (cm^{-1}) and δ is the delta-function. According to this relationship the DOS plots in Figure 1.1 can be drawn. 2-D and 1-D structures such as graphene and carbon nanotubes (CNTs) respectively exhibit a series of "bands" each of which possess a continuum of energetic states. However, when a charge carrier is confined in all three dimensions (as is the case for an approximately spherical NC), a discrete series of energetic states similar to atomic transitions is observed.

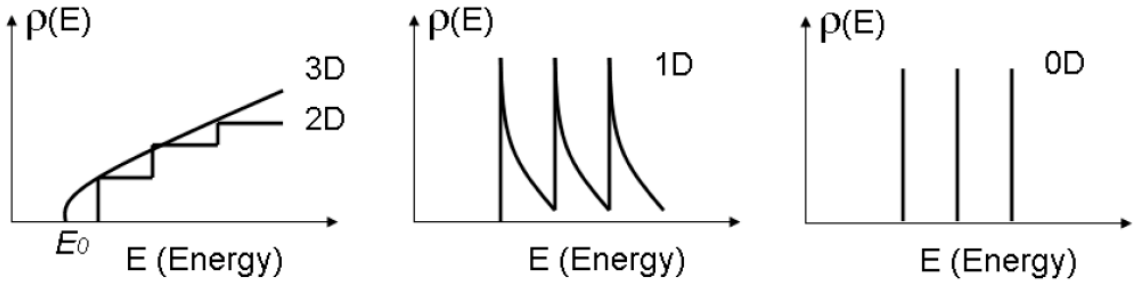

Figure 1.1: Density of states in confined nanostructures as a function of energy and dimensionality.

The degree to which spatial confinement leads to separation of the energetic states in a NC is a function of the Bohr radius in the bulk material. If one or more dimensions of the NC are smaller than the Bohr radius, the NC is said to be in the "strong confinement" regime. Under these conditions the Coulombic interaction between the excited electron and hole remains significant and

the bound electron-hole pair is called an exciton. Table 1.1 provides an illustrative example of how the confinement energy in several common NCs changes when the NC size is equal to the Bohr radius as well as when the NC size is substantially smaller than the Bohr radius.

Table 1.1: Comparison of quantum confinement in various semiconducting materials.

Material	Bulk E_g (eV)	Bohr Radius (nm)	E_g ($r = r_{Bohr}$) (eV)	E_g ($r = 0.5*r_{Bohr}$) (eV)
ZnSe	2.7	3.8	3.26	3.54
CdSe	1.74	4.9	2.04	2.48
PbS	0.41	18	0.51	0.64

Brus was the first to develop a theoretical model for the effect of quantum confinement in a semiconducting NC.[2] Assuming a spherical NC volume the Brus Equation (Equation 1.1) effectively predicts the first excitonic transition in a semiconducting NC by taking into account the intrinsic bandgap of the bulk material, the quantum confinement of the exciton, and the Coulombic interactions of the bound exciton and hole.

$$E_g(r) = E_{bulk} + \frac{h^2}{8r^2}\left(\frac{1}{m_e^*} + \frac{1}{m_h^*}\right) - \frac{1.8e^2}{4\pi\varepsilon_o\varepsilon_\alpha r} \qquad \textbf{Equation 1.1}$$

In the above equation the first term is the bandgap of the bulk material and describes the energy difference between the valence band and conduction band of the bulk semiconducting material. The second term, where *h* is Planck's constant, *r* is the NC radius, and m_e^* and m_h^* are the effective mass of an electron and hole respectively, describes the increased exciton energy that arises from spatial confinement: by application of Schrodinger's equation to a particle in a box, energy is found to be inversely proportional to L^2 where L is the length the box edge. The third

term, where e is the elementary charge, ε_o is the permittivity of vacuum, and ε_a is the relative high-frequency dielectric constant, reflects a decrease in exciton energy resulting from shielded Coulombic attraction between the electron and hole in the confined NC volume. It is immediately apparent that the r^{-2} dependence of exciton energy will dominate the absorption of a semiconducting NC.

In reality the wave function of an electron is able to extend outside of the NC core, to an extent proportional to the bandgap and dielectric constant of the surrounding medium. When the NC core is surrounded by an insulating organic ligand shell exciton confinement can be relatively efficient. The degree of confinement can be increased or decreased by addition of an inorganic shell surrounding the NC core. NCs of this type are called "core-shell" NCs.[6]

The choice of shell material is strongly dependent on the application in which the NC will be used. If the NC will be used as a fluorophore to emit light, it is desirable to have an insulating (large bandgap) shell that confines the excitons within the core. This type of core-shell structure is called "Type-I". As shown in Figure 1.2 the shell material's wide bandgap prevents the electron and hole from escaping the core, resulting in enhanced exciton recombination efficiency and photoluminescent emission. Alternatively, if the NC will be used as a source of electrons (as is the case for photovoltaic devices) it is preferable to facilitate exciton separation and transfer of charge out of the NC and into a surrounding material. This can be achieved using "Type-II" core-shell NCs in which the band structure of the material leads to confinement of either electrons or holes in the core, facilitating transfer of an unbound carrier.

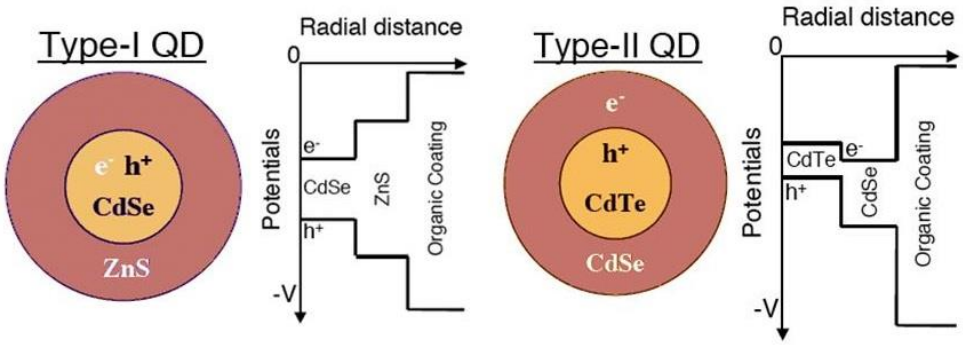

Figure 1.2: Structure and band position of core-shell NCs.[7]

1.3.2 Surface Area Effects in NPs

By virtue of their size NPs exhibit a variety of novel properties that arise from their exceedingly high surface area-to-volume ratio. As seen in Table 1.2 the fraction of atoms located at the surface of small NCs can exceed 50 % and the surface-area-to volume ratio can exceed 220 m^2/g. By contrast, a powder of 1 μm diameter CdSe particles is expected to have a specific surface area of only 0.5 m^2/g. The unparalleled specific surface area of nanoparticles poses certain challenges as well as advantages in technological applications. The most profound challenge is the high surface energy and tendency toward aggregation that results from having a large number of dangling atomic bonds at the NP surface. For this reason NPs are not thermodynamically stable and the use of surfactants at the NP surface is necessary to kinetically hinder the aggregation process.

Table 1.2: Surface area effects as a function of CdSe NC size.

CdSe NC diameter	Total # atoms	Fraction of surface atoms	Specific surface area (m^2/g)
2.3	226	54 %	224
3.2	616	42 %	161
5.0	2378	28 %	103

The high surface area to volume ratio found in NPs is advantageous for applications such as catalysis and mechanical reinforcement of composite materials where the amount of surface area for a given quantity of material impacts the performance and cost of the final product. To illustrate this effect we will consider the specific surface area (m^2/g) of platinum, one of the most widely used industrial catalysts: In order to attain 1 m^2 of platinum catalyst surface area using 1 μm diameter platinum clusters, approximately $50 worth of platinum (at current market prices [~$1450/oz.]) would be required. By contrast, using 20 nm particles, 1 m^2 of platinum catalyst surface area could be attained for only $2 (at current market prices).

The high surface area of NPs has interesting optical implications as well, one of which is the phenomenon of Mie scattering: in addition to absorption (proportional to the volume fraction of NC core material) there is substantial elastic scattering of visible light (proportional to the NC surface area per unit volume). In the Mie scattering regime elastic scattering is found to scale with r^6, where r is the NC radius. As empirically demonstrated by Yu et. al,[8] the apparent extinction coefficient of semiconducting NCs is strongly correlated with size. As seen in Figure 1.3 the extinction coefficient of CdSe, CdS, and CdTe can be described using a third-order polynomial.

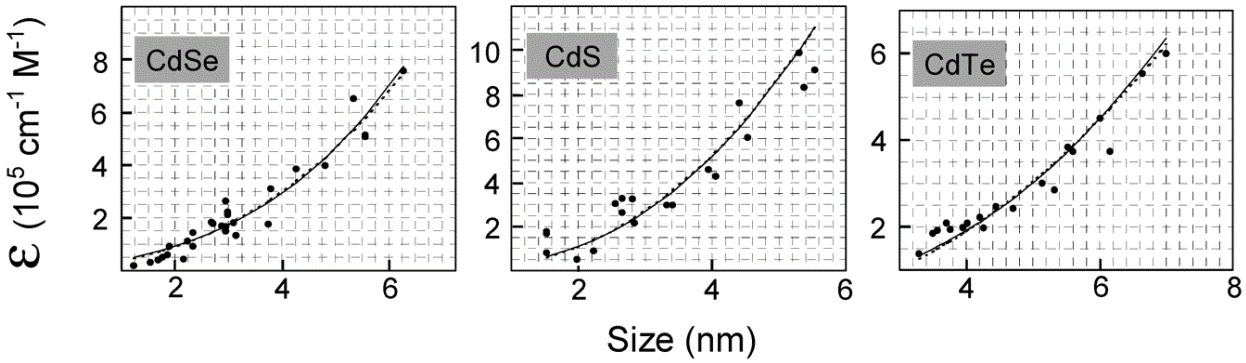

Figure 1.3: Experimentally determined extinction coefficient for various NCs as a function of NC diameter.[8]

1.3.3 Size and Shape Control in Nanoparticle Synthesis

The majority of inorganic NPs share a common structure consisting of an inorganic core surrounded by an organic surfactant layer; the ligand shell. The core of a NP can be crystalline (i.e. nanocrystals) or amorphous and may take on a variety of geometries such as spheres, cubes, disks, and rods.[9] As previously mentioned, ligands serve the crucial role of preventing NP aggregation. The ligand itself has up to three important components: the head-group which binds to the inorganic core, the functional-group which faces away from the core and strongly influences the NP's interactions with surrounding media, and the intervening tail or chain which tends to provide steric repulsion with other NPs. A depiction of this generic NP structure is presented in Figure 1.4.

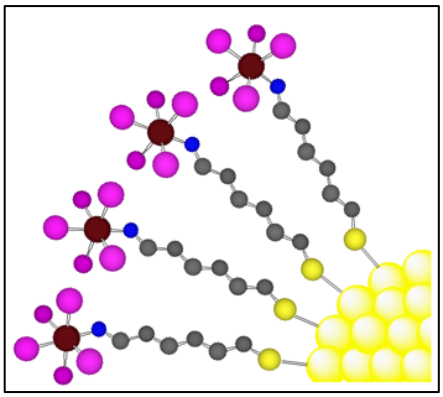

Figure 1.4: Depiction of generic NC structure depicting core and ligand molecules.

Many synthetic routes exist for the production of NPs, but in general the precursor materials for the inorganic core are combined in a heated solvent in the presence of an appropriate ligand. Frequently the inorganic precursor is an organo-metallic complex such as an oleate, silane, or phosphonate. A solvent is chosen that is stable at the reaction temperatures and provides good solvation to the host chemicals (inorganic precursor and ligands). The ligand in turn must be chosen such that it has a head group that binds strongly to the eventual inorganic core and prevents macroscopic growth of the NP.

A successful NP synthesis reaction generally includes three distinct growth stages. Immediately following addition of the inorganic precursor(s), commonly at high temperature, precursor concentration rapidly increases above a critical nucleation concentration (C_{min}) leading to rapid nucleation of new NP cores (Figure 1.5, Region I-II). Nucleation rapidly consumes the inorganic precursor causing the precursor concentration to decrease to a level at which further nucleation events do not occur; however, provided there is sufficient thermal energy, precursor material will continue to combine with existing nuclei, causing clusters of precursor material to grow into NP cores (Figure 1.5, Region II).[10] Finally, after a period of diffusion-limited growth the precursor concentration drops below the precursor solubility (C_s) the precursor in solution reaches an equilibrium with the NC core (i.e. material leaving the cores equals the reverse addition reaction), at which point NC growth stops (Figure 1.5, Region III).[11] During the nucleation and growth stages the ligand plays a crucial role in limiting the growth rate and size of NPs by hindering precursor addition to existing cores and preventing separate cores from undergoing aggregation.[12] The solvent too can affect NP growth by influencing precursor solubility and acting to kinetically limit precursor movement.

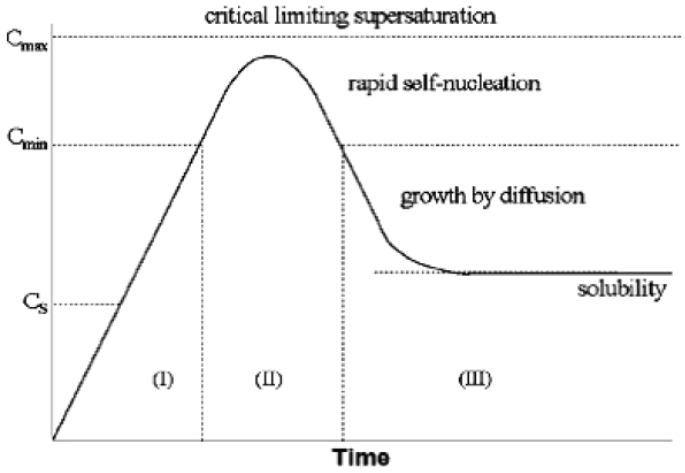

Figure 1.5: Monomer concentration vs. time during NC synthesis.[13]

Through extensive experimentation synthetic routes have been developed that enable precise control of size, geometry, and composition of NPs.[14] The initial precursor concentration and reaction temperature have a strong influence on the number of NP nucleation events and therefore the number of particles. The size of particles can often be controlled through reaction time, temperature, as well as precursor concentration.[15] Selection of a strongly binding ligand will tend to produce small particles, but in some cases the ligand can also increase precursor solubility and indirectly promote Ostwald ripening, yielding larger particles. The shape of NPs can be tailored by utilizing the tendency of some ligands to bind more strongly to certain crystalline facets than others, promoting anisotropic growth and yielding geometries such as wires, tetrapods, and disks.[14, 16]

The shape evolution and growth kinetics of the elongated nanocrystals have been well studied and suggest a diffusion-limited growth mechanism. The monomer concentrations after the initial nucleation stage has a strong influence on the size and shape of the resulting nanocrystals. The ligand type has also been shown to play a critical role during the growth of colloidal CdSe nanorods.[17] A recently reported systematic study of the ligand functionality on the colloidal synthesis of CdSe nanorods clarified the role of the length of the organic capping ligands on the growth kinetics of colloidal CdSe nanorods and the stability of the nanorod solution.[10] There exist clear trends showing that the shorter the alkylphosphonic acid ligand, the more elongated are the resulting nanorods and the more the branching. Further, using mixtures of alkylphosphonic acids indicates the higher the molar fraction of the shorter ligand, the more elongated and branched are the nanorods

NPs are frequently synthesized according to their intended application. Applications requiring strong selective absorption and emission[18] may require a semiconducting core with highly insulating ligands or possibly an insulating inorganic shell (i.e. type-I core-shell).[19]

Alternatively, if the NPs are to be used in a photovoltaic device in which exciton separation and charge transfer is desirable, a type-II core shell architecture combined with short conductive ligands could be appropriate.[20] High aspect ratio nanostructures such as nanowires or nanoplatelets are commonly employed if electrical percolation or mechanical reinforcement is important.[21]

1.3.4 Conductive Ligand Terminated Nanocrystals

For almost a decade following their discovery in the early 1980's NC research focused on synthesis and characterization of NCs with high-molecular weight, insulating organic ligands. The choice of such ligands was a logical one in light of the function ligands are intended to serve: to form a protective monolayer at the NC surface which prevents aggregation (via steric or electrostatic repulsion) and facilitates NC solubility. The majority of NC synthetic routes require high-temperature decomposition of precursor materials in a nonpolar organic solvent, dictating the choice of organic ligands such as trioctylphosphine oxide, dodecanethiol, and hexadecylamine to name a few. Each of these ligands accomplished the important function of making NCs stable under a wide range of experimentally useful conditions.

As scientific understanding of NC properties increased, so did the interest in utilizing NCs in devices such as transistors, sensors, and photovoltaic devices (PVs).[22] By the 1990's it was understood that many NC applications would require NCs to efficiently exchange energy with a surrounding medium by transfer of electrons into and out of the inorganic core. This motivated a search for organic ligands that facilitate charge transfer between the NC core the surrounding environment.[23] As will be discussed in this thesis, ligands composed of conjugated organic molecules (as depicted in Figure 1.6) can facilitate charge transfer between NCs and their surroundings and can enable NCs to be used in a variety of electronic applications.[24, 25] Recently

there has also been substantial progress in the use of inorganic conductive ligands,[26] but that work is beyond the scope of this thesis.

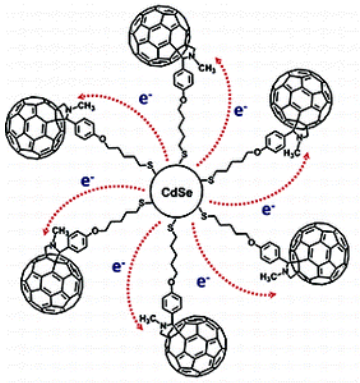

Figure 1.6: Depiction of CdSe NC with fullerene ligands.[24]

In this thesis we will explore the use of novel synthetic procedures for generating NCs capped with organic ligands capable of conducting electrical charge into and out of the inorganic NC core.[27] Building on work developed by Owen et. al,[28] solution-phase synthetic routes for the production of benzene terminated (phenylphosphonic acid) CdSe NCs and naphthalene terminated (naphthoic acid) lead sulfide (PbS) have been developed and studied. This capability greatly enhances the potential utility of NC composite materials for applications involving inter-phase energy transfer such as photovoltaic devices and sensors. Furthermore, the absorption spectrum of CdSe and PbS NCs together span virtually the full range of the visible (CdSe) and near-IR (PbS) spectra and could therefore be combined in a PV device to yield efficient broad-band performance. In this thesis we will discuss synthetic routes for producing NCs with potentially conductive ligands, the optical-electronic properties of these NCs, and performance of composite organic/NC PV devices incorporating these NCs.

1.3.5 Cadmium Selenide Nanocrystals

Bulk cadmium selenide (CdSe) is a II-VI direct bandgap semiconductor with a wurtzite structure capable of efficient optical absorption and luminescence throughout much of the optical spectrum (E_g = 1.73 eV) . In 1983 Brus and coworkers[2] showed that nanocrystals of CdSe could be grown using solution-phase synthesis techniques. Methods for growing CdSe NCs are now highly optimized, reliably yielding NCs of many sizes and shapes and making CdSe NCs an important platform for the study of optical and electronic properties in nanoscale semiconductors.

The synthesis of CdSe NCs consists of thermally-induced precipitation of cadmium and selenium precursors in a carefully chosen solution of solvent and surfactant. There are two important types of CdSe NC synthesis: one utilizing dimethylcadmium as the cadmium precursor [29] and the other using cadmium oxide (CdO) as the cadmium precursor. [30] Both methods will be discussed in detail in Chapter 2.

The CdO synthesis route involves the addition of CdO to a solvent containing an organic acid (commonly an alkyl-phosphonic acid or alkyl-carboxcylic acid). The solvent is always selected to have a high boiling point and to be nonpolar, but may be coordinating (such as trioctylphosphine oxide) or non-coordinating (such as octadecene). This mixture is heated to an elevated temperature (> 200 °C) at which time the acidic species undergoes a condensation reaction with CdO, producing an acid-coordinated cadmium ion and a water molecule (Mechanism 1.1).

$$2\ R\text{-}HPO_3 + CdO \rightarrow Cd(R\text{-}PO_2)_2 + H_2O$$ **Mechanism 1.1**

After a degassing step used to drive off the water product, the solution is heated to ~300-350 °C, at which point a selenium precursor (typically trioctylphosphine-selenide) is rapidly injected. The

process of NC nucleation and growth that follows injection of the selenium precursor will be discussed after introducing details of the dimethylcadmium synthetic route.

The dimethylcadmium route to CdSe NC synthesis differs from the CdO synthesis route in that both cadmium and selenium precursors are added to the reaction mixture simultaneously. Specifically, a solution of dimethylcadmium and trioctylphosphine-selenium are injected together into a hot solution (~350 °C) of coordinating solvent (TOPO) containing a small amount of alkylphosphonic acid (~1 wt. %). Following injection of the inorganic precursors several distinct stages of nucleation, growth, and aging occur. Immediately following the combination of the cadmium and selenium precursors, heat from the reaction solution provides the activation energy necessary for the cadmium and selenium precursors to break their organic coordination and react with one another to form a population of NC nuclei, often consisting of only a few cadmium and selenium atoms. The process of CdSe nucleation is strongly influenced by the concentration of inorganic precursor material, and persists for only a short time after injection.

After only several seconds, the concentration of inorganic precursor decreases to a level below the critical nucleation concentration (also significant is the decrease in temperature that accompanies the addition of the room-temperature precursors). Although nucleation events cease, CdSe nuclei that have exceeded a critical size continue to grow by addition of inorganic precursor material. In a parallel process, nuclei that have not reached a critical size are prone to dissolution, providing a source of inorganic material that will be added to the larger and still-growing nuclei. During this process the acid species acts like a ligand, binding to the NC surface, slowing the growth process and preventing the aggregation of NC cores. A second and less intuitive role of the ligand species is to increase the solubility of the inorganic precursor and facilitate the dissolution of

smaller NC nuclei. Depending on reaction conditions the growth stage of a typical CdSe NC synthesis may take between 5 seconds to 10 minutes.

The final stage of a typical CdSe NC synthesis is an annealing step, sometimes called "aging". During the aging stage of a synthesis the concentration of precursor in solution has been sufficiently depleted and the reaction temperature reduced (~ 280 °C) such that NC growth is minimal. However, by virtue of their small size each NC contains a large fraction of under-coordinated surface atoms, which increases the thermodynamic energy of the CdSe material above that of a bulk material, and lending substantial mobility to the individual atoms. So despite the fact that 280 °C is well below the melting temperature of bulk CdSe, it is possible for the crystallinity of CdSe NCs to be improved by "aging" them for ~20-60 minutes during the final stage of a synthesis.

Although both the CdO and dimethylcadmium synthetic routes can yield high-quality CdSe NCs, the dimethylcadmium route is rapidly being replaced by the CdO synthetic route as well as newer methods[31] due to the extreme toxicity of dimethylcadmium.

Through appropriate synthetic routes the diameter of CdSe NCs can be precisely controlled between approximately 1.5 – 12 nm.[12] As previously mentioned, the Bohr radius in CdSe is 4.9 nm, causing NCs with a diameter of less than ~5 nm to exhibit strong confinement of excited states. Optical absorption in CdSe NCs can therefore be tuned from 700 nm (NC diameter > 10 nm) to approximately 390 nm (1.5 nm NC diameter).[32] This range represents a large fraction of the optical spectrum visible to humans, and therefore makes CdSe NCs suitable for experimentation as well as utilization in technologies such as emissive displays.

1.3.6 Lead Sulfide Nanocrystals

Lead sulfide (PbS) NCs are an increasingly important category of inorganic NC due to their ability to absorb and emit light in the near-IR spectrum. In the bulk form PbS has a bandgap of 0.41

eV and can efficiently absorb light at wavelengths shorter than 3025 nm. From a technological perspective the small bandgap of bulk PbS limits its utility; however, because PbS has a Bohr radius of 18 nm it is possible to increase the effective bandgap of PbS NCs through quantum confinement.[33] By controlling the size of PbS NCs between 1 – 5 nm it is possible to tune the bandgap such that absorption falls between approximately 600 – 1400 nm.[32] This is a technologically important portion of the near-IR spectrum; enabling efficient absorption and power conversion of an energy-rich portion of the terrestrial solar spectrum.

The synthesis of PbS NCs is similar to that of CdSe NCs.[34, 35] In the most commonly utilized synthesis, a lead precursor such as lead acetate ($Pb[Ac]_2$) or lead oxide (PbO) is first reacted with an alkylcarboxcylic acid (oleic acid or steric acid).[35, 36] At an elevated temperature (> 150 °C) the acetate or oxygen of the lead precursor binds to the proton of the acid species and forms a volatile product that can be removed under vacuum, leaving only the complexed lead ion in solution (lead oleate or lead stearate). The reaction mixture is then heated (> 200 °C) at which point a reactive sulfur precursor is added. Typically the sulfur compound is trimethylsilane-sulfur (TMS-S) but it can also be trioctylphosphine-sulfur (TOP-S) or any other nucleophilic ligand species. At these elevated temperatures the lead and sulfur precipitate into nanocrystals with growth mediated by the presence of the acidic ligand species. As previously mentioned, the ligand concentration can act to increase the solubility of free lead monomer (i.e. Pb^{2+}) in the reaction mixture. For this reason it is found that adding an excess of ligand (i.e. carboxcylic acid) can lead to digestion of smaller NCs and lead to an increase in average NC size.

1.4 Macroscopic Nanoparticle Films

While the physical properties of individual NPs is of academic interest, it is the collective behavior of NP ensembles that is of greatest importance to many technological NP applications. 2-D

films are by far the most common macroscopic NP structure and have been used to create a variety of useful materials with applications including magnetic memory, photovoltaic devices (PVs), light-emitting diodes (LEDs), and chemical sensors. When discussing the characteristics of a NP film it is common to describe the thickness, density, and uniformity. A fourth property that will not be discussed in this thesis is order; the characteristic of some NP films to develop long-range NP periodicity.

1.4.1 Drop-cast Nanoparticle Films

The most basic technique for creating 2-D NP films is drop-casting. As the name suggests the NPs are applied to a stationary substrate by application of a solution containing NPs in a volatile carrier solvent. As the solvent evaporates the NPs form a 2-D film that can range in thickness from a few monolayers to thousands of monolayers. As mentioned above, there is a subcategory of drop-cast NP films that form ordered "superlattices"; however, the vast majority of drop-cast NP films are disordered. One drawback to drop-cast NP films is that as the film gets larger in lateral extent and/or thickness, the variability in film properties also increases. Differences in evaporation rate and NP solubility across the wetted substrate area lead to fluctuations in film thickness and density, sometimes leading to film cracking. Drop-casting of NP films also does not offer spatial selectivity, which restricts its use to applications that can tolerate non-specific NP decoration.

1.4.2 Spin-cast Nanoparticle Films

Spin-casting of NP films utilizes NPs suspended in a volatile carrier solvent, which is then applied to a rotating substrate. The additional shear forces present during the deposition and evaporation process enables the formation of NP films that are uniform (thickness and density) over centimeter length-scales. According to Equation 1.2 the thickness of such films (h) can be

carefully controlled by adjustment of the solution viscosity (ν), solvent evaporation rate (E) and substrate angular velocity (ω) during deposition.[37-39]

$$\frac{\partial h}{\partial t} = -2\left(\frac{\omega^2}{3\nu}\right)h^3 - E \qquad \textbf{Equation 1.2}$$

However, spin-cast films also do not provide in-plane deposition selectivity. For applications such as LEDs in which only discrete areas of a substrate require decoration this can lead to wasted or cross-talk between closely spaced components.

1.4.3 Electrophoretically Deposited Nanoparticle Films

Electrophoretic deposition (EPD) has been used for many years to deposit films of colloidal particles on conductive substrates from aqueous and polar organic solutions.[40-43] Typically these particles have been micron-scale and produced through milling or grinding processes.[42] More recently it has been found that EPD can also be used to deposit NCs from nonpolar organic solvents.[44-46] In both cases the EPD process offers the unique capability of creating a dense, conformal, and spatially-selective coating on a conductive substrate. Charged NPs in solution migrate under electrostatic force to the electrodes, eventually reaching an electrode, and depositing at the time of charge transfer. Under appropriate conditions (field strength, solvent type, and NP characteristics) it is possible to deposit films with micron-scale lateral selectivity with nanometer precision in the out-of-plane direction.

Traditionally EPD is carried out in an aqueous environment with particles deposited on a work piece under the influence of an applied field on the ionic double-layer surrounding the charged colloid particle. Islam et al.[45, 47, 48] demonstrated that EPD could also be used to deposit cadmium selenide (CdSe) NCs from a nonpolar solution. Since that time, EPD has been used to

deposit a wide variety of inorganic NCs including ZnO, PbS, Au, and many more. More recently Singh et al. have shown that the same electric field used to move particles to the electrode surface can simultaneously align CdSe nanorods (NRs) with an intrinsic dipole, leading to dense films of well aligned NRs with novel anisotropic optical properties.[49]

When discussing EPD of NCs from an organic solvent it is useful to examine the differences with traditional aqueous-phase EPD of colloids. In an aqueous environment colloidal particles are traditionally stabilized by repulsive electrostatic interactions. Specifically, the colloid particle exhibits a net charge that is balanced by a surrounding layer of compensating counter-ions called a double layer (Figure 1.7). This phenomenon is made possible by the high dipole moment and dielectric constant of water and its ability to support charged ionic species. There is of course a requirement for over-all charge neutrality in the aqueous deposition solution, suggesting that the original charge on the colloid core results from a charge conserving process such as the reduction/oxidation of an ionic species, charge transfer with the surrounding system (containment vessel and atmosphere) or partial solvation of the colloid core.

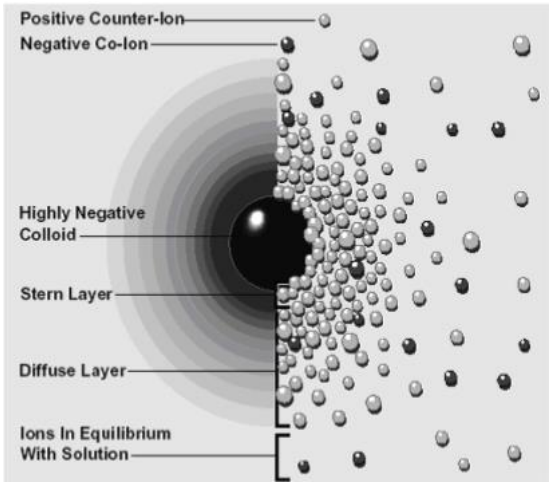

Figure 1.7: Depiction of stabilized colloid particle.[50]

To understand how a charged colloid (with a surrounding shell of counter ions) can respond to an applied electric field, it is important to examine the structure of the double layer and electric potential in a dielectric medium. The work piece to be coated and counter electrode can be roughly approximated to behave like the plates of a capacitor across which a voltage is applied. We assume that the electric potential is the sum of the potential resulting from a continuous distribution charge in the medium (i.e. charged colloids) and the charge present on each plate arising from the applied voltage. We can then apply what is known as the diffuse double layer model to predict the potential distribution in the EPD system and how charged colloid particles will move in response to an applied electric field.[50]

Although the mechanism of EPD in an aqueous environment is relatively well understood (i.e. movement of charged particles in a strong DC electric field), the phenomenon of NC EPD in nonpolar organic solvents remains an area of active research. In particular the origin of the observed NC charge and the ability of the nonpolar solvent to solvate a charged NC is unclear. There exist two distinct populations of thermally-charged NPs: some positively charged and others negatively charged.[51] Zeta-potential measurements reveal a strong correlation between particle "washing" and NC charge, suggesting that NCs develop a net charge at their surface resulting from vacant ligand binding sites. [46] With increased washing the zeta-potential of CdSe NCs can be shifted toward negative values, at which point EPD becomes possible. The charged NCs are presumably stabilized by the van der Waals interaction of the remaining ligands with the organic solvent. Charge neutrality can be explained by the presence of trace impurities in the deposition solvent (originating from the synthesis process) that form the charged double layer. The final step of NC deposition may be explained by local depletion (or exclusion) of these stabilizing counter ions near the electrode surface, leading to charge transfer and NC precipitation (i.e. deposition).

While EPD is experimentally straightforward to accomplish, a rigorous understanding of NC EPD requires careful consideration of interconnected processes, including NC synthesis, NC processing, and deposition. The subtlety of tuning these processes lies in controlling the interconnected NC characteristics of solubility, charge, mobility, and charge transfer. When a suitable combination of processing steps and deposition conditions are chosen, it is possible to deposit dense, uniform NC films of varying thickness onto a patterned conductive substrate. For nanocomposites this offers the potential to locate NC filler material at strategic locations in a potential product.

1.5 Hybrid Composite Organic/NC Materials

Materials composed of only NCs can exhibit a range of interesting and useful physical properties, but are ill-suited for direct utilization in devices and functional materials. In the absence of a stabilizing medium individual NCs are prone to aggregation and oxidation, while macroscopic NC structures are vulnerable to mechanical damage and can produce hazardous air-born dust. The vast majority of functional NC materials are therefore composite structures in which the NC phase is supported by a matrix material that lends mechanical and chemical stability. Depending on the application the matrix material may also be chosen it exhibit complementary optical or electronic properties. Hybrid organic-NC composites of this type have emerged as an important new class of material that can exhibit electrical, optical, and mechanical properties that cannot be attained using traditional composites (i.e. > 1 micron scale fillers) or monolithic materials.

1.5.1 Nanocomposite Materials from Back-filled EPD NC Films

Posing a challenge to the direct application of EPD NC films is the observation that upon removal of an EPD NC film from the deposition solution, the evaporation of deposition solvent

causes a volumetric contraction of the film, and, in the case of CdSe NC films over approximately 600 nm in thickness, leads to film fracture.

The phenomenon of EPD film contraction results from the change of inter-NC spacing in the wet (i.e. with deposition solvent present) and dry film states. For a more precise understanding it becomes necessary to understand what forces determine inter-NC spacing in the two states (wet and dry). At this point one assumption will be made: that attractive inter-particle forces are constant and attributed entirely to van der Waals interaction between NC cores. It is then a question of understanding the origin of inter-NC repulsive forces and how they vary with the films solvent content.

Two processes are expected to be dominant when considering inter-NC repulsive forces: ligand-ligand steric interference and capillary pressure acting on the deposition solvent. The former will scale from one finite positive value to another finite positive value as the solvent leaves the film, while the latter is expected to approach zero as the film reaches a fully dry state. We can therefore say that in the as-deposited (wet) state inter-NC spacing will correspond to a balance between attractive van der Waals forces and the sum of repulsive steric interference (between ligands) and positive capillary pressure exerted by the deposition solvent. In the dry state inter-NC a balance between van der Waals forces and steric forces will determine spacing only. In Chapter 3 we will discuss theories developed in the field of polymer science and apply conservation of volume arguments to examine how the change of inter-NC equilibrium spacing leads to strain (and frequently fracture) in the dried EPD NC film.

Because EPD film fracture exposes the underlying substrate and leads to nonuniformity in film properties, it is important to prevent film fracture in order to arrive at a useful and uniform composite material. The above discussion of factors contributing to EPD NC film fracture suggests

two mechanisms by which fracture of NC EPD films can be avoided: replacing the deposition solvent with a non-volatile substance and/or maintaining a high degree of steric interference between ligands on adjacent NCs by increasing their persistence length in the dry state.

For the first mechanism, solvent replacement, there are two apparently conflicting criteria. The filling agent that replaces the deposition solvent should be small enough to thoroughly infiltrate the interstitial regions of the film and reach all locations originally occupied by the deposition solvent. Simultaneously the filling agent should be composed of molecules large enough to be completely nonvolatile under standard conditions. One way in which both criteria can be met is to add a small functional monomer to the as-deposited film and subsequently polymerize the monomers into high molecular weight molecules that will not evaporate and can resist compressive stress. As will be discussed in Chapter 4 the use of monomer infiltration and subsequent polymerization can lead to crack-free EPD NC films with enhanced mechanical properties.

Alternatively it should also be possible to increase ligand persistence length by increasing the density of ligands at the NC surface. As described above, during drying ligands contract and assume a more ball-like conformation that reduces surface energy at the expense of persistence length. Since as-deposited NCs have relatively sparse ligand coverage there is ample room adjacent to each ligand to permit this condensed ligand conformation. However, if ligand density is increased there is expected to be steric interference between adjacent ligands bound to the same NC such that all ligands must maintain a rod-like conformation even in the dried state.

It would be convenient to deposit NCs with sufficient ligand coverage to avoid ligand contraction and subsequent EPD film cracking, however, as previously discussed, it is typically necessary to deposit NCs with sparse ligand coverage, which leads to a net NC zeta-potential and may increase the probability of NC adhesion to the substrate. We therefore must deposit NCs via

EPD that do not have high ligand coverage, and then modify their surfaces with new ligands after they have been deposited. In Chapter 3 we will explore a technique where by fracture of EPD CdSe NC films is prevented through treatment with the ligand molecule trioctylphosphine oxide after deposition but prior to drying. The resulting EPD CdSe NC film is crack free and exhibits enhanced PL efficiency.

1.6 Nanocrystal Composites for Electronic Applications

As described above the optical and electronic properties of NCs are potentially useful in electronic applications such as emissive displays and PV devices. In order to effectively harness the useful physical attributes of NCs it is common to embed them in a host material that lends mechanical strength, chemical stability, and electronic coupling. In this thesis we will explore one such nanocomposite material that has potential application for PV devices. This hybrid nanocomposite material is comprised of an organic semiconducting film that has undergone a novel nanoscale templating process to yield a nanowire morphology, which is then back-filled with an inorganic NC phase. In order to understand the aggregate performance of this hybrid organic/inorganic composite material it is important to understand the properties of each constituent phase and how the two phases interact.

1.6.1 Organic Semiconducting Materials

In recent years there has been a proliferation of new semiconducting organic materials that exhibit novel semiconducting properties by virtue of carefully engineered conjugated structures. Through manipulation of symmetry and elemental composition organic semiconducting materials have emerged that have potential application in emissive displays, low-cost logic circuits, and photovoltaics. Although present day manufacturing costs of many organic semiconductors is

relatively high ($100-1000/gram), the abundance of precursor elements creates the potential for low-cost mass production. Organic semiconductors also offer the unique characteristics of low density, mechanical flexibility, solution-phase processing, and environmentally friendly disposal.

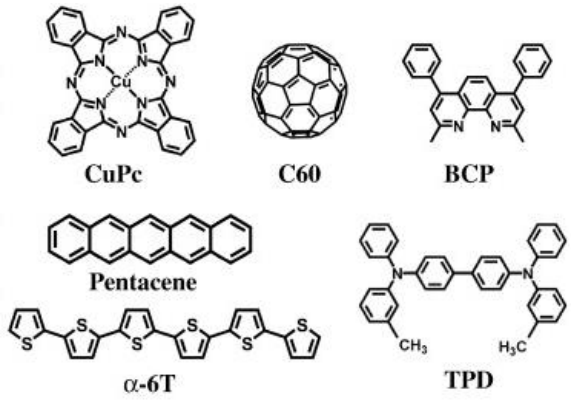

Figure 1.8: Molecular structure of various semiconducting organic materials.[52]

As depicted in Figure 1.8 organic semiconductor are predominantly composed of carbon, sulfur, and nitrogen. Common to all such materials is a molecular structure consisting of alternating single and double carbon bonds, a conjugated structure. Each carbon atom in a conjugated structure possesses three covalently bonded sp^2 hybridized electrons and a single electron residing in the p_z orbital extending perpendicular to the plane of the other three electron orbital's (i.e. plane of conjugation). As depicted in Figure 1.9 the p_z electrons of adjacent carbon atoms form a resonant sp^2 molecular orbital in which each electron becomes delocalized over the entire conjugation center. A single organic semiconducting molecule may be composed of many conjugation centers, typically linked through short covalent bonds forming what is called a "π-system".

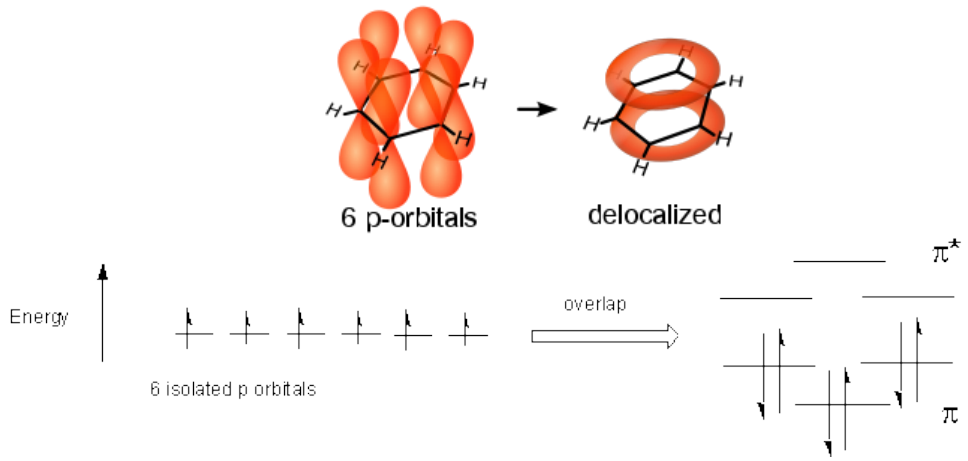

Figure 1.9: sp^2 hybridization of p-orbitals in benzene ring.[53]

1.6.2 Electronic Properties of Organic Semiconductors

Similar to inorganic semiconductors, organic semiconductors possess a bandgap across which electrons must be promoted in order to become free charge carriers. However, unlike bulk inorganic (crystalline) semiconductors, which are described by extended valence and conduction bands, organic semiconductors are more accurately described by a localized molecular band structure. Within each conjugation center there exists a highest occupied molecular orbital (HOMO) analogous to the valence band and a lowest unoccupied molecular orbital (LUMO) analogous to a conduction band. Electrons residing in the HOMO level (designated π-electrons) are excited to the LUMO level (π^*-electrons) where they become delocalized over the conjugation center.

Immediately following excitation of an electron from the HOMO level to the LUMO level an electron and corresponding hole reside on the same conjugation center and are tightly bound by Coulombic effects (a result of the low dielectric constant of most organic materials). As depicted in Figure 1.10, the bound electron-hole pair, known as an exciton, does not possess a net charge and does not respond to an external electric field. These excitons do however respond to concentration gradients, and diffuse toward regions of low exciton concentration.[54]

Figure 1.10: Depiction of exciton localized on a conjugation center of an organic semiconducting polymer.[55]

In order to separate the exciton into its respective electron and hole it is necessary to provide sufficient energy to overcome the Coulombic binding energy. This can be accomplished thermally, or more commonly by providing an interface with another semiconducting material that has a lower LUMO level (facilitating electron transfer) or higher HOMO level (facilitating hole transfer). Figure 1.11 depicts the creation of a bound exciton arising from photo-absorption, followed by the formation of a charge transfer (CT) state following electron transfer to an acceptor phase. Following exciton dissociation the electron and hole physically reside on different molecules. However, their close proximity and the low dielectric constant of the organic medium leads to a CT state in which the electron and hole remain bound by electrostatic attraction.[56]

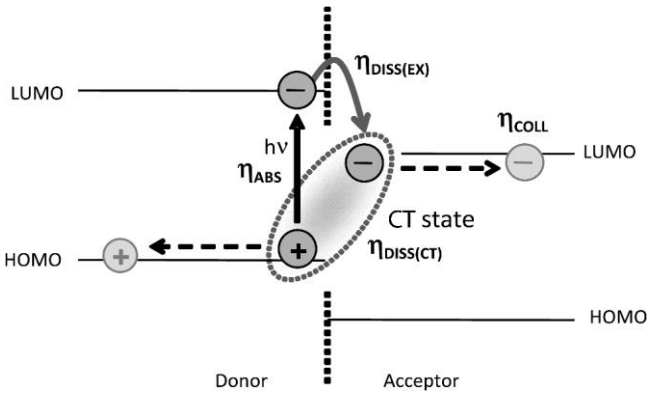

Figure 1.11: Charge transfer at an organic donor-acceptor interface.[56]

If the binding energy of the CT state is overcome, generating a free electron and hole, charge carrier movement through an organic material occurs via "hopping"; a process whereby a charge carrier residing on one conjugation center moves in a discrete event to an adjacent conjugation center. Free carriers in an organic semiconductor are frequently referred to as "polarons" due to

the local dipole and the molecular distortion they create in the soft organic host material.[57, 58] The process of charge hopping must act to lower the free energy of the mobile species in the form of reduced chemical potential energy (i.e. moving down a concentration gradient) or reduced Coulombic energy (i.e. under the influence of an electric field). The rate of conduction via charge hoping is often mediated by the need for thermal activation, leading to the uncommon observation that conductivity in organic semiconductors often increases with temperature.[57, 59]

An important factor influencing the efficiency of a PV device is the fraction of *absorbed* photons that lead to a free carrier entering an external circuit. This ratio is described by the internal quantum efficiency (IQE, Equation 1.3) of a device and is the product of the efficiency with which excitons reach a donor-acceptor interface (η_{ED}) , the dissociation efficiency of bound excitons ($\eta_{DISS,EX}$), the separation efficiency of the CT state ($\eta_{DISS,CT}$), and the efficiency with which free carriers are collected by an external circuit (η_{CC}).[60]

$$IQE = \eta_{ED} * \eta_{DISS(EX)} * \eta_{DISS(CT)} * \eta_{CC} \qquad \textbf{Equation 1.3}$$

The efficiency with which the CT state is separated (η_{CT}) is a major limitation in organic photovoltaic (PV) performance. If the CT state is not separated quickly (< 500 ps)[60] recombination between the original electron and hole (geminate pair recombination) as well as recombination between electrons and hole originating from different excitons (non-geminate recombination) become likely. Additional energy is required to efficiently break the CT state and efficiently generate free carriers. An applied device bias in addition to thermal energy (possibly from the $LUMO_D$-$LUMO_A$ transition) must supply approximately 300 meV to overcome the CT bond and create free carriers.

Other commonly used definitions for the efficiency of a PV device include external quantum efficiency (EQE), and photoconversion efficiency (PCE). The EQE of a device reflects the fraction of *incident* photons that lead to a free carrier entering an external circuit, and can be expressed by Equation 1.4, where η_{ABS} reflects the fraction of photons, of a given energy, that are absorbed. EQE, like IQE is a wavelength-specific value.

$$EQE = \eta_{ABS} * IQE \qquad \textbf{Equation 1.4}$$

The most inclusive measure of PV device efficiency is the PCE, which according to Equation 1.5 reflects the ratio of electrical power extracted from a PV device verse the solar energy incident on the device,[61, 62]

$$PCE = \frac{P_{electrical}}{P_{solar}} = \frac{V_{MPP} * I_{MPP}}{\int_0^\infty P(\lambda) EQE(\lambda) d\lambda} \qquad \textbf{Equation 1.5}$$

where the maximum electrical power of the device ($P_{electrical}$) is the product of the output current (I_{MMP}) and voltage (V_{MMP}) at the maximum-power-point of the device (see Figure 1.16). The power density of irradiance on the device (P_{solar}) can in turn be expressed as the product of the solar power at each wavelength, multiplied by the device EQE at that wavelength, integrated over all wavelengths of incident light.[61]

1.6.3 Poly(3-hexylthiophene), P3HT

Presenting the expansive topic of organic materials beyond the scope of this thesis, so we will limit the scope of the discussion to the widely used organic semiconducting polymer poly(3-hexylthiophene) (P3HT), which is studied in Chapter 5. Thiophenes are a widely studied and utilized class of organic semiconductor.

Polymers such as P3HT reflect an effort by chemists and material scientists to modify the physical characteristics (solubility, miscibility, crystallinity, etc.) of the polythiophene molecule without negatively affecting the conjugated electronic structure of the polymer. By adding pendant groups to the thiophene repeat unit, it has been found that the device performance of polythiophenes can be greatly improved.[63, 64] In the case of P3HT, the addition of a six-carbon alkyl chain to the conjugated repeat unit produces a polymer that exhibits excellent miscibility characteristics and enhanced crystallinity, thereby improving charge transport in photovoltaic devices.[63]

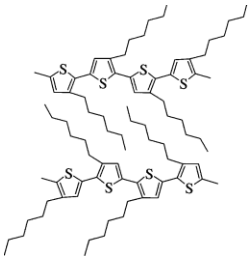

Figure 1.12: Depiction of P3HT molecules exhibiting side-chain stacking in the (h00) crystalline axis.[65]

P3HT has a HOMO level located at approximately -4.65 eV (relative to vacuum) and a bandgap of bandgap of between 2.2-2.5 eV [65, 66]. Conduction in P3HT is dominated by hole transport through the valence band, with reported mobility values as high as 10^{-4}–10^{-3} cm^2 V^{-1} s^{-1}.[67] When paired with an electron acceptor material such as C_{60} or CdSe NCs, P3HT acts as an efficient electron donor and hole conductor. The optical absorption of P3HT is shown in Figure 1.13.

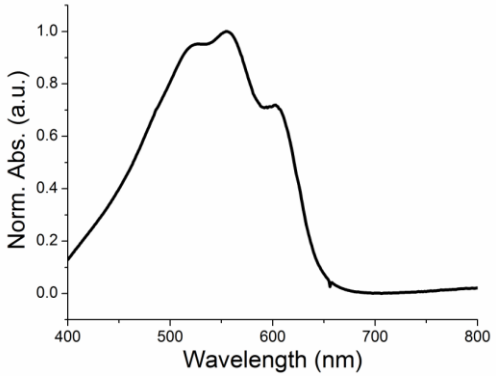

Figure 1.13: Absorption spectrum of typical P3HT film cast on a glass substrate.

1.6.4 Crystallinity and Morphology of P3HT in Multi-phase Organic Blends

P3HT is widely used in PV devices as the electron donating species in a donor-acceptor blend. The relatively high hole mobility, moderate bandgap, and position of the LUMO level in P3HT all make it an attractive material for pairing with electron accepting species such as fullerenes and inorganic NCs. One of the most unique and advantageous characteristics of P3HT is its tendency to crystallize into elongated nanoscale crystallites. In the presence of a poor or marginal solvent, P3HT nanowires form spontaneously due to intermolecular stacking of adjacent π-systems (π-π stacking). The results are P3HT nanowires composed of P3HT chains aligned in the direction of the wire axis [001] and with π-π stacking occurring perpendicular to the nanowire axis. Orthogonal to the direction of π-π stacking [010] is a crystalline axis characterized by lamellar side-chain stacking (Figure 1.12), designated [100].

The nanowire morphology of P3HT can be advantageous for device performance. As discussed above, in order to efficiently extract free charge carriers from P3HT (or any other organic semiconductor) the exciton must diffuse to a donor-acceptor interface where a favorable band off-set between the LUMO levels of the acceptor and donor phases facilitates exciton separation. Studies have shown that for exciton dissociation to occur efficiently in P3HT, an exciton must reach

an interface within approximately 400 ps, corresponding to a diffusion distance of ~ 8-12 nm at room temperature. [54, 60]

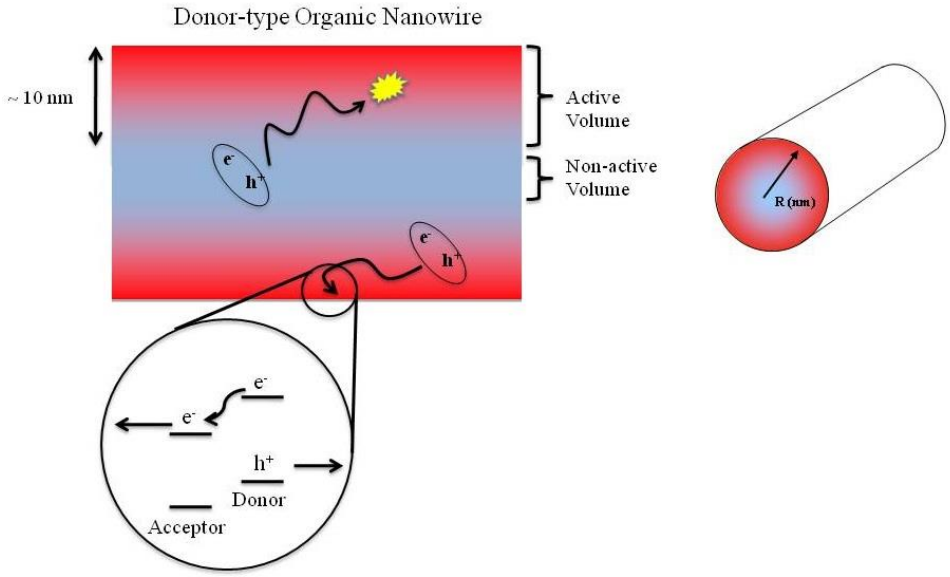

Figure 1.14: Active volume within a nanowire structure.

The optimal morphology of an organic PV device often correlates to a geometry exhibiting the greatest "active volume fraction": the volume fraction of absorbing material within an exciton diffusion length of a donor-acceptor interface. Excitons generated outside of this volume are expected to undergo recombination before being separated into free electrons and holes, and therefore do not contribute to the performance of the PV device. In most organic semiconductors, excitons are able to diffuse ~ 10 nm prior to recombination. An exciton in an inorganic CdSe NC film is also highly localized (typically located on a single NC core),[68] but unlike an organic material, an exciton in a NC may persist for up to ~1 μs. These length scales suggest several morphologies that offer a high active volume fraction: densely packed spheres or cylinders of the donor (acceptor) material with diameters of ~ 20 nm embedded in the acceptor (donor) phase or a laminar morphology of alternating donor/acceptor layers which are ~ 20 nm thick (~10 nm thick if a

bilayer). However, the requirement for continuous electron and hole conduction pathways to the cathode and anode of a PV device suggest that only nanowires embedded in the complementary phase or a bilayer donor/acceptor morphology will yield a useful PV device. The need for significant absorption by the composite material (i.e. a satisfactory optical depth) greatly reduces the utility of a bilayer device in which each phase may be only ~10 nm thick. A nanowire morphology of intermixing donor and acceptor materials is therefore the most likely structure to yield an efficient composite NC/P3HT PV device.

1.7 Hybrid NC-P3HT Composites for Photovoltaic Device Applications

For the reasons described above, a composite material consisting of an inorganic semiconductor such as P3HT and inorganic NCs (such as CdSe or PbS) offers the potential to yield a material with good photovoltaic performance. In order to rationally design a composite material of this type it is necessary to consider the physical process of generating photovoltaic energy and how materials and processing can be harnessed to produce an efficient hybrid organic-NC PV device.

1.7.1 Introduction to Photovoltaic Devices

A photovoltaic device is characterized by the intimate junction of two semiconducting materials (or phases); one or both of which absorbs light and generates excited electron-hole pairs (i.e. excitons). In the case of an organic PV device at least one of the photoactive materials will be an organic semiconductor and exhibit the various physical properties discussed above. By virtue of off-sets in the conduction (LUMO) and valence (HOMO) bands of the respective phases, excitons which reach the interface of the two materials will be separated into free carriers. As depicted in Figure 1.15 the material that accepts and conducts electrons is called the “acceptor” phase (n-type), while the material that accepts and conducts holes is called the “donor” phase (p-type). Typically it

is the donor phase in which the majority of optical absorption occurs, however in Chapter 5 of this thesis we will investigate hybrid NC/P3HT composite materials in which both phases are expected to absorb incident light and generate excitons.

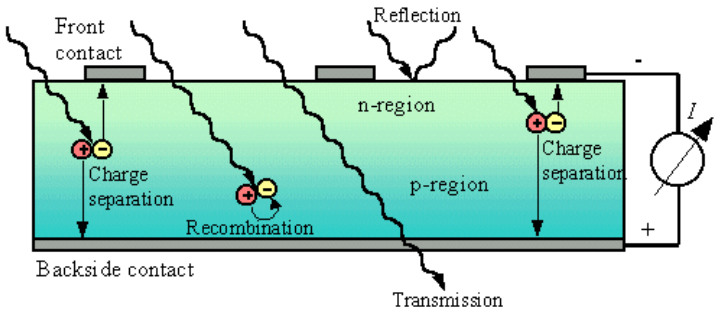

Figure 1.15: Schematic of charge collection in a photovoltaic device.[69]

The performance of a PV device is often modeled using a circuit diagram of the type depicted in Figure 1.16.[70, 71] The various circuit elements are intended to capture the various physical phenomenon that occur in a PV device. I_l represents the sum of all excitons that reach a donor-acceptor interface. The diode element is included parallel to the current source to account for events such as recombination of carriers in the CT state and annihilation of free carriers that encounter other free carriers of the opposite charge (geminate and non-geminate recombination respectively). The R_{SH} circuit element (shunt resistance) reflects the fact that free carriers can undergo further recombination with oppositely charged carriers at the unintended electrode if shunt pathways are present. Finally, R_S (series resistance) represents the average resistance encountered by electrons and holes within the device as they travel from their point of origin to the cathode or anode respectively.

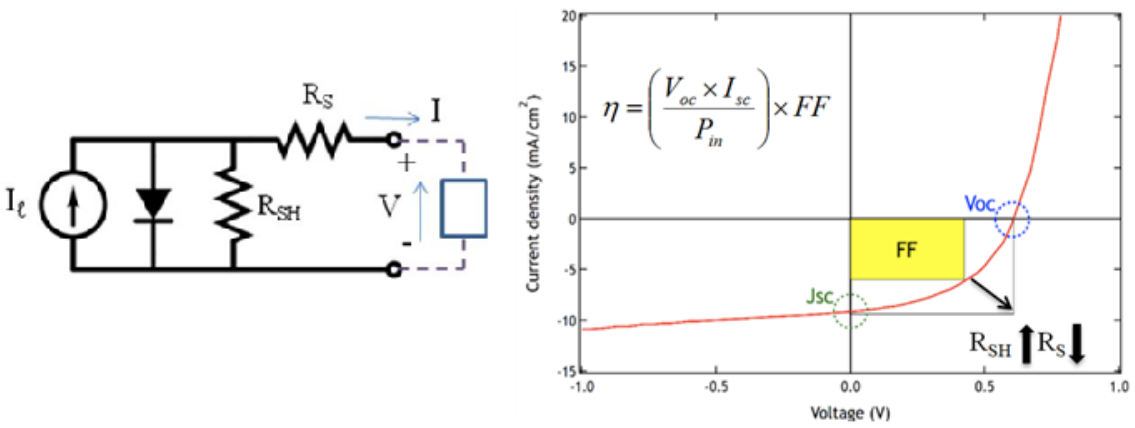

Figure 1.16: Circuit diagram representing a PV device and corresponding I-V curve under illumination.

When the circuit diagram in Figure 1.16 is applied to a constant current source (such as an ideal PV device) the resulting device current-voltage (I-V) response can be described using Equation 1.6 and Equation 1.7, where I = I_{SC} when there is no load across the terminals of the PV device (i.e. "short circuit current") and V_{OC} is the voltage across the terminals of the device when no current is allowed to exit the circuit (i.e. "open circuit voltage").[72]

$$I = I_l - I_0 \exp\left(\frac{q(V + I_l R_s)}{nkT} - 1\right) - \frac{V + I_l R_s}{R_{SH}} \qquad \textbf{Equation 1.6}$$

$$V_{OC} = \frac{1}{e}[E(HOMO)^{Donor} - E(LUMO)^{Acceptor}] - 0.3V \qquad \textbf{Equation 1.7}$$

The I-V curve corresponding to Equations 1.6 and 1.7 can be seen in Figure 1.16. From Equations 1.6 and 1.7 it is possible to write an alternative expression for PCE (than that given by Equation 1.5). By employing the concept of fill-factor (FF), which describes the geometry of the I-V curve and the ideality of the PV device performance, we can use Equation 1.8 to calculate the PCE of a PV device.

$$PCE = \frac{FF(V_{OC} * I_{SC})}{P_{solar}}$$ **Equation 1.8**

It is immediately apparent that optimal PCE of a PV device will correspond to a large V_{OC}, a high I_{SC}, and a FF approaching unity. These conditions will be satisfied when R_{SH} is large (infinite) R_S is low (zero).

In order to determine an optimal combination of materials and processing techniques for a PV device it is useful to consider the above circuit diagram and four physical parameters that correlate with good PV performance: (1) Bound electron-hole pairs (excitons) must originate from optical absorption throughout an energetic portion of the solar spectrum (~1.0-1.6 eV)[73, 74] within a diffusion length (~ 10 nm) of a donor-acceptor interface, maximizing I_I, (2) the band energy off-set of the donor-acceptor interface ($LUMO_{donor}$-$LUMO_{acceptor}$) should facilitate efficient exciton separation into free carriers (without unnecessarily reducing the voltage of the PV device, $HOMO_{donor}$ - $LUMO_{acceptor}$), minimizing the apparent diode losses, (3) the electron and hole conducting phases must offer continuous conduction pathways (with minimal tortuosity) to the cathode and anodes respectively, minimizing R_S, and (4) continuous donor or acceptor pathways between the cathode and anode (i.e. shunt pathways) must be avoided to minimize R_{SH}.

Meeting these optical, morphological, and electrical requirements is a difficult task that requires careful consideration of materials and processing. Here we will quantify the above criteria in order to motivate the selection of materials and processing used to fabricate the hybrid composite material(s) described in this thesis.

The band structure of each constituent phase (organic and inorganic NC) influences both the absorption spectrum and exciton separation efficiency within a composite PV material. The energetic difference between the valence (HOMO) and conduction band (LUMO) within each

material (i.e. bandgap, E_g) determines the longest wavelength (lowest energy) photon that phase can absorb. In the absence of other criteria, this characteristic of absorption would suggest that selection of materials with the smallest bandgaps are preferable by virtue of their ability to absorb the widest portion of the solar spectrum. However, much of the photon energy in excess of E_g is lost to thermal energy, so optimal efficiency of a PV device (based on a single absorber) occurs when E_g ~1.0-1.6 eV.[73, 74] Moreover, the relative positions of the electron and hole conducting bands (conduction/LUMO and valence/HOMO respectively) directly influence exciton separation efficiency as well as the voltage output by a PV device.

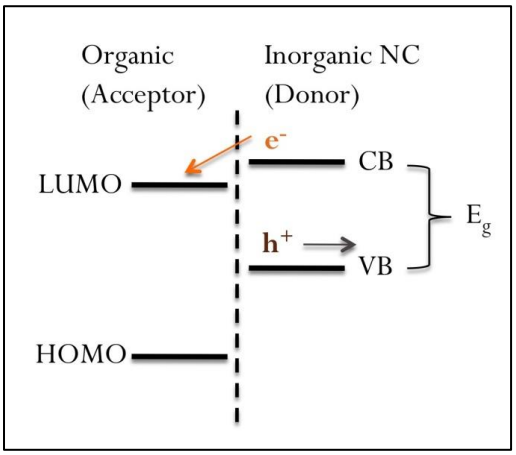

Figure 1.17: Depiction of inorganic NC donor-organic acceptor interface.

In order to harness the favorable electronic and morphologic properties of P3HT, it is mixed with an acceptor phase that has appropriate electronic and miscibility characteristics. Desirable electronic characteristics of the acceptor phase include high electron mobility, a bandgap greater than that of P3HT (assuming P3HT to be the primary absorber), and a LUMO level at a more negative value than that of P3HT. An acceptor phase LUMO level ~300 meV below that of P3HT has been reported to promote efficient separation of the CT state resulting from initial exciton dissociation across the donor-acceptor interface.[60, 72] Traditionally, the acceptor phase must also

exhibit certain good solubility in a common P3HT solvent such as toluene, chlorobenzene, or chloroform and only moderate miscibility with P3HT in the absence of solvent, promoting growth of the P3HT nanowire morphology.

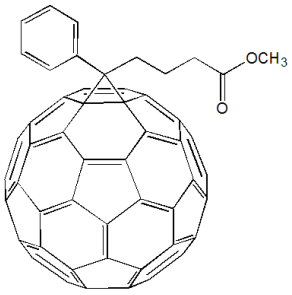

Figure 1.18: Chemical structure of PCBM molecule.

With the above criteria in mind it is not surprising that fullerenes have emerged as a common type of acceptor material for pairing with P3HT in PV applications. [75, 76] Specifically [6,6]-phenyl-C_{61}-butyric acid methyl ester (PCBM) with a C_{60} moiety has proven to exhibit a good combination of electronic and miscibility characteristics (Figure 1.18). PCBM has a HOMO level of -6.18 eV and a LUMO level of -3.17 eV, corresponding to a bandgap of approximately 2.48 eV.[77] This places the LUMO level of PCBM approximately 800 meV below that of P3HT, facilitating exciton dissociation at the P3HT/PCBM interface. Furthermore, PCBM has excellent solubility in many of the same solvents used to dissolve P3HT, and upon removal of these solvents it is observed that P3HT grows into highly crystalline nanowires surrounded by a PCBM rich matrix.

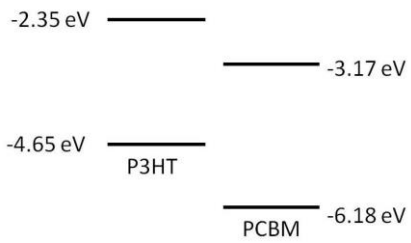

Figure 1.19: Band structure of P3HT-PCBM interface.

1.7.2 The Bulk Heterojunction Architecture for Organic Photovoltaic Devices

The term bulk-heterojunction (BHJ) is used to often used to describe a donor-acceptor blend with nanoscale phase separation, such as the type found in blends of P3HT and PCBM. As the name suggests the key attribute of this structure is an abundance of dissimilar material interfaces occurring throughout the volume of a bulk (or microscale) material. This structure stands in contrast to more traditional bilayer or solid-solution materials in which the phase interfaces are precisely located or entirely absent respectively. A depiction of a BHJ structure is given in Figure 1.20.

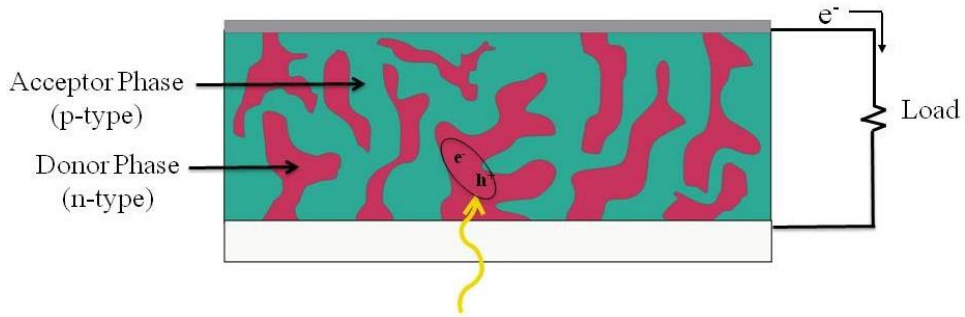

Figure 1.20: Depiction of bulk-heterojunction architecture.

The use of P3HT with various fullerene derivatives (including PCBM) was one of the first material combinations shown to spontaneously generate a BHJ structure that proved efficient for use in PV devices.[72, 78, 79] Typically P3HT and the fullerene species are mixed in a common solvent that fully dissolves both species. The solution is then spin-cast on a transparent conductive substrate. As the carrier solvent evaporates during (and following) the spinning process, the concentration of the donor (P3HT) and acceptor (fullerene) species increase and eventually exceed the solubility limit of the remaining solvent at which time precipitation of solid material occurs. A fraction of the P3HT forms nanowires suspended in a matrix of fullerene. The fullerene species tends to fill the regions between P3HT crystallites but is also known to form pure crystalline

regions of its own. While not optimized, this spontaneous demixing of the donor and acceptor phases is the first step in the formation of a BHJ structure that can be used in the production of efficient organic PVs.

Post-deposition treatment of the deposited donor-acceptor BHJ structure can lead to dramatic improvement of crystallinity, morphology, and eventual PV device performance.[80-83] Thermal annealing of as-deposited BHJ films is the most important processing step in the formation of optimized BHJs.[84] Grazing-incidence wide-angle x-ray scattering (GIWAXS) experiments have shown that annealing of the as-deposited film at temperatures between 70-180 °C can dramatically increase the crystallinity of the donor and acceptor phases.[80, 83] The crystallization process is accompanied morphological changes such as growth of P3HT crystallites and redistribution of fullerene.[80, 82, 83] While it is difficult to deconvolute the effects of crystallinity and morphology on PV device performance, it has been conclusively demonstrated that thermal annealing improves PV device performance.

The work of Loos and Ade has attempted to isolate the importance of changes in morphology during the annealing process.[82, 85, 86] Work by Nelson and coworkers has found that crystallization of the P3HT phase concludes at relatively short annealing times (< 5 min) while nanoscale morphology continues to evolve over longer time scales during annealing.[80] Specifically they have shown that annealing leads to changes in morphology associated with migration of the fullerene species.[80] In recent years it has been proven that an optimal BHJ device does not consist of only two distinct donor and acceptor phases, but also a third phase that is an amorphous solution of the two materials. Mass-contrast transmission electron microscopy has proven a powerful tool in monitoring the evolution of BHJ morphology during annealing. The work of Loos has been particularly powerful in demonstrating that upon annealing PCBM diffuses into regions of

amorphous P3HT creating a mixed phase containing up to 25 wt. % PCBM.[81, 85, 86] This work has been complemented by investigation of BHJ films using dynamic secondary ion mass spectrometry (DSIMS). Using DSIMS, Treat et al. have shown that intercalation of PCBM into amorphous regions of P3HT is thermally activated and can lead to diffusion of PCBM through the full thickness of a 200 nm thick planar P3HT film.[83] Characterization of the same films with GIWAXS confirms that this redistribution of PCBM does not disrupt P3HT crystallites (the size of P3HT crystallites is observed to increase) and is instead driven by intermixing of PCBM with amorphous regions of P3HT.

Although less widely employed, vapor-phase solvent annealing of as-deposited BHJ films with a low boiling point solvent such as toluene or chloroform has also been found to facilitate crystallization and phase separation, leading to improved PV device performance.[87, 88] Typically this process is employed prior to thermal annealing.

Through advances in materials and processing it has become possible to reliably produce all-organic BHJ materials with excellent PV performance. The highest reported PCE for such devices are now over 9%.[89-91] Due to the low cost of the precursor materials, their high active-volume fractions (i.e. film volumes within an exciton diffusion length of a donor-acceptor interface), and their potential for high-throughput production (i.e. roll-to-roll processing) organic BHJs are an attractive platform for low-cost solar energy conversion.

1.7.3 Photovoltaic Nanocomposites with a Bulk Heterojunction Morphology Formed by Back-filling of P3HT Nanowires with Inorganic NCs

Attaining higher efficiencies from organic PV devices will likely require new materials systems that absorb in the infrared (IR) portion of the solar spectrum. In particular, the use of inorganic IR sensitizing materials in conjunction with organic materials holds promise for enhancing the efficiency of low-cost PV devices.[92-94] Inorganic NCs have desirable optical and

electronic properties and could serve as an optical sensitizing agent within a hybrid BHJ.[95-97] As seen in Figure 1.21, inorganic NCs such as PbS could effectively sensitize a hybrid PV device to the mid-IR portions of the terrestrial solar spectrum (740-2500 nm), representing up to 43% of the solar energy reaching the earth's surface.[98]

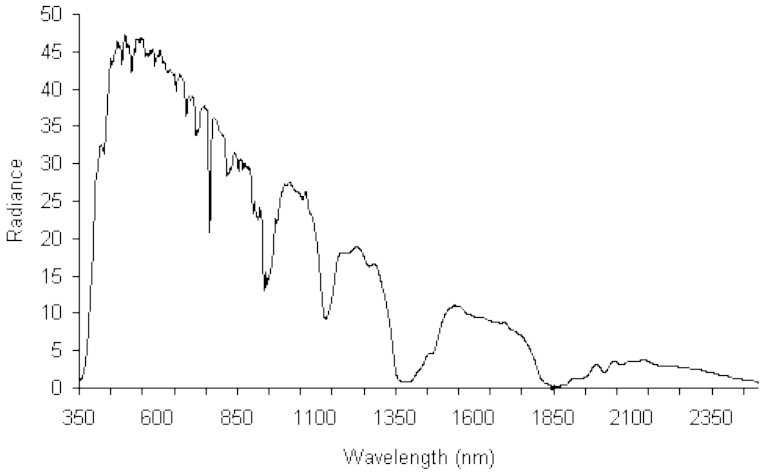

Figure 1.21: ASTM 1.5AM terrestrial solar spectrum.

Hybrid organic/inorganic PV devices are an enticing platform for solar energy conversion due to the potentially low cost of the precursor materials as well as the possibility for high-throughput production (i.e. roll-to-roll processing). The incorporation of an inorganic semiconducting material into organic PV devices could increase the PCE of such devices by increasing infrared (IR) light absorption [$\eta_{ABS}(\lambda_{IR})$, Equation 1.4]. Semiconducting inorganic NCs are a good candidate this application due to their broad size-dependent absorption and high internal quantum efficiency (approaching 100%). Figure 1.22 shows that a 4 nm CdSe NCs with a band gap slightly less than that of P3HT will, by virtue of its band structure,[32] act as an effective electron acceptor when in contact with P3HT. Furthermore, NCs can be processed using solution-

phase techniques similar to those used for organic semiconductors and are amenable to similar high-throughput processing techniques.

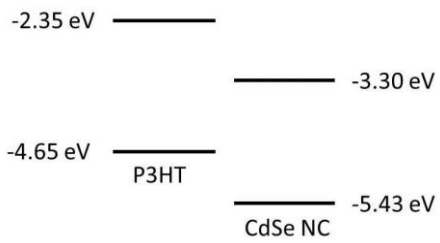

Figure 1.22: Position of HOMO and LUMO levels of P3HT compared to valence and conduction band levels of a 4 nm diameter CdSe NC.

However, if traditional one-step casting methods are to be used, it is crucial that NCs have a specific set of solubility and miscibility criteria that promote the formation of a BHJ architecture with the organic phase (Figure 1.23). In reality it is found that the simultaneous requirements of NC stability (i.e. avoidance of aggregation), good electrical conductivity (i.e. short conductive ligands), and miscibility are difficult to attain; yielding hybrid NC/organic materials that lack an efficient BHJ morphology. Specifically, it is observed that NCs with short conductive ligands tend to aggregate within an organic donor material, resulting in an inefficient donor-acceptor morphology. Attempts to improve NC/polymer miscibility have centered on the use of exotic conjugated ligands that hinder hole transport through NC-rich regions of the material.[24] The use of traditional one-step casting techniques, such as spin casting NCs simultaneously with organic semiconducting materials, have therefore met with limited success and modest device performance.[3, 99, 100]

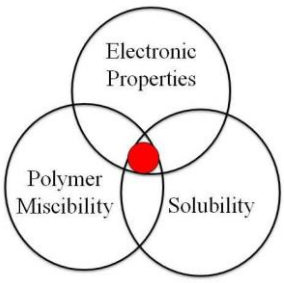

Figure 1.23: Criteria for the formation of an efficient BHJ PV material.

One strategy for attaining a BHJ morphology in a composite NC-organic material is to structure one phase of the composite first and then backfill the second phase.[101] For photovoltaic devices it is particularly desirable to generate a nanowire morphology which results in a high volume fraction of material within an exciton diffusion length[58] of a donor-acceptor interface (i.e. active-volume). In Chapter 5 we show a novel technique for employing this strategy and demonstrate how it can be used to improve the PCE of NC-sensitized organic PV devices.

Considerable research has been dedicated to the development of low-dimensional structures composed of organic semiconductors.[102-104] Previous work has shown that it is possible to deposit a mat of P3HT nanowires on a variety of substrates utilizing rigid templates[105-108] and electrospinning,[109, 110] as well as by growing P3HT nanowires in a marginal solvent and casting these fibers on a substrate.[111-113] Using such techniques it is possible to backfill a high active-volume P3HT morphology with a complementary acceptor material, in some cases yielding photovoltaic devices with external quantum efficiencies (EQEs) of over 3%.[111, 112] More recently it has been shown that various organic nanowires (including P3HT) can be decorated with NCs while still in solution prior to casting on to a substrate.[114-116] Although solution-phase methods for generating P3HT nanowires can yield efficient BHJ structures, their reliance on relatively large volumes of dilute P3HT nanowire solutions is undesirable from a production standpoint. The need for careful filtration of unwanted byproducts further limits the utility of solution-phase nanowire production.

1.8 Work Explored in this Thesis

The increased importance of nanoscale materials is being driven by the need for advanced materials with new optical, electronic, magnetic, and mechanical properties. As will be discussed in this thesis, the utility of these nanoscale structures is only as great as their ability to influence the

macroscopic world that we live in. It is often necessary for nanomaterials such as those used in photovoltaics or structural composites to incorporate > 10^{12} nanoparticles per cubic centimeter in order to yield an aggregate performance that is competitive with existing (i.e. micro or macroscopic) technologies. The question then arises: how can billions of individual nanostructures (NCs, NWs, etc.) act in unison to accomplish a common purpose? In many cases, the answer to this question is that these individual nanostructures must interact with a common macroscopic medium that in some way pools their collective performance to yield a useful effect. As the reader may realize, this is the classic description of a composite material.

It will be shown in this thesis that nanocomposite materials are an important topic in nanotechnology by virtue of their physical properties arising from the collective behavior of nanoscale structures (i.e. NCs, nanowires, etc.) located in a common unifying medium. An important characteristic of any such composite materials is the location and morphology of the interface between the filler material (typically the NC phase) and the matrix phase (typically an organic material). There are, however, problems inherent to nanocomposites that are not present in conventional composites utilizing macroscopic filler materials: the inability to selectively place nanoscale structures (such as NCs) within a final product, and, in the case of electrically active nanocomposites, the insulating nature of organic binder materials. The theme of this thesis will be to study mechanisms by which these two problems can be mitigated in NC/organic nanocomposites through sequential processing using back-fill methods.

Throughout this thesis, two-step back-filling techniques will be used to control the location, morphology, and chemistry of NC-organic interfaces within nanocomposite materials. By separating the synthesis of the nanocomposite into multiple processing steps it is possible to utilize fabrication techniques that are well suited to a single phase, while avoiding conditions that might

damage the other phase. Figure 1.24 depicts how a two-step fabrication process of a hybrid NC/organic composite can expand the range of viable process conditions, thereby improving material quality and expanding the range of potential composite structures.

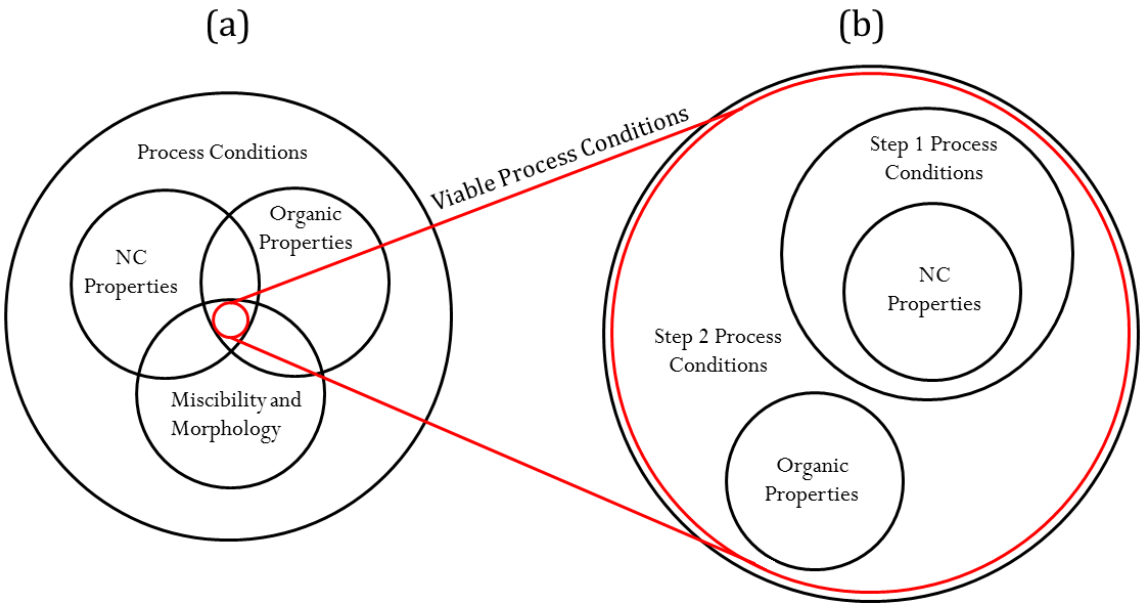

Figure 1.24: Depiction of increased process flexibility through (b) two-step nanocomposite fabrication compared to (a) single-step fabrication.

Often the first step in the design of a nanocomposite material containing NCs is the choice of NC ligand. As described in Chapter 2 and applied in Chapter 6, the surface properties of a NC can be controlled at the molecular scale by application of synthesis methods resulting in deliberately chosen ligand molecules chemisorbed to the NC core surface. These ligands represent a crucial component of a NC composite and will dictate NC solubility and mediate the exchange of energy (electrical, thermal, mechanical) between the NC core and the binder material, resulting in changes to the mechanical, optical, and electronic properties of the composite. When chosen correctly, ligands will protect NCs from degradation (such as oxidation) and facilitate subsequent processing steps such as EPD, solution casting, etc. We will present several NC synthesis methods for the preparation of NCs with ligands that facilitate EPD, improve energy transfer, or both.

EPD of NCs is a process that is sensitive to not just ligand type, but also ligand density. In Chapter 2 we will describe the post synthesis "washing" of NCs that is necessary prior to EPD. An unfortunate side-effect of this washing procedure and the associated loss of ligands is that as-deposited EPD NC films contain a substantial amount of deposition solvent and undergo substantial contraction upon drying. If the EPD NC film is thick (~ 600 – 800 nm), fracture of the dried film typically occurs. We show in Chapter 3 and Chapter 4 that back-filling methods can be applied to EPD NC films to create mechanically robust and highly photoluminescent nanocomposite.

Chapter 3 will examine the implications of back-filling EPD NC films with excess ligand material and the properties of the composite film that results. We will show that by controlling the amount of ligand material added to the as-deposited EPD NC film it is possible to suppress fracture of the dried film while adjusting the film thickness, elastic modulus, and PL efficiency.

In Chapter 4 we find that fracture in dried EPD NC films can also be suppressed by addition of polymeric precursor molecules (monomers), followed by UV-polymerization to create a NC/polymer composite. In addition to being free of cracks, these composite films are found to have improved elastic recovery and are highly photoluminescent (compared to untreated EPD NC films).

In Chapter 5 we demonstrate the versatility of two-step back-filling methods by reversing the roll of organic and inorganic phases presented in Chapters 3 and 4: organic nanostructures are back-filled with inorganic NCs to create a nanocomposite for PV applications. Films of organic semiconducting nanowires are first generated by manipulating the phenomenon of spontaneous phase separation in hetero-polymeric blends. After removal of one polymeric phase, a film of semiconducting P3HT nanowires is exposed. The nanowire films are then back-filled with a complementary phase of CdSe NCs passivated with small ligand molecules (pyridine). By separate

application of the organic and NC phases using back-fill methods we are able to create a bulk-heterojunction nanostructure that is well suited to PV applications.

Finally, in Chapter 6, exploratory studies are conducted that employ the full set of tools discussed above (ligand chemistry, EPD, and back-fill methods) in conjunction with electron beam lithography to create novel photoactive materials. We first show that fracture of thick EPD NC films can be avoided when the lateral dimension of the NC film is limited by selective deposition on micron-scale patterned electrodes. An interdigitated electrode architecture is then selectively decorated with small-molecule terminated NCs using EPD; leading to dense, crack-free NC films with micron-scale lateral dimensions. These patterned EPD NC films are subsequently back-filled with a complementary NC film applied via spin-casting. The resulting nanocomposite material (overcoating an appropriate patterned electrode) represents a device architecture that is capable of lateral (in-plane) exciton separation and potential application as a low-cost platform for PV devices.

The ability to control the location and morphology of nanocomposite interfaces through two-step back-filling methods will be explored from multiple directions to create hybrid nanocomposite materials with enhanced functionality. Various size scales of interfacial engineering will be utilized. It will be shown that at the molecular scale control of the nanocrystal interface through choice of ligand enables control of nanocrystal growth (i.e. size and shape), solubility, and energy transfer. At the nanometer length scale we will show that EPD of inorganic NCs and growth of organic nanowires through demixing of polymeric blends can be used to create nanostructures with unique mechanical, optical, and photovoltaic performance. At the micron length scale we will employ lithographic techniques to create device architectures for novel photovoltaic devices. In each case the selected mechanism for interfacial control within the nanocomposite will be

employed as part of sequential processing method utilizing back-filling techniques to achieve a nanocomposite structure with the desired physical attributes.

2 Experimental Methods

2.1 Synthesis of Inorganic Nanocrystals

Inorganic nanocrystal (NC) synthesis is typically a high-temperature chemical reaction carried out under inert atmophere conditions. Using an apparatus similar to the one depicted in Figure 2.1. The contents of a three-neck flask are heated using an electric heating mantle positioned beneath the flask, while a thermocouple with a vacuum-tight seal inserted through one of the flask openings monitors temperature. Using a digital temperature controller, the temperature of the reaction mixture can be carefully controlled. The atmosphere of the flask is controlled utilizing a vaccum/nitrogen manifold. Typically the flask is placed under vacuum, then filled with an inert gas (nitrogen). This process is repeated several times until very little oxygen or moisture is left in the head-space of the flask. Reactants can be added to the flask (even at high temperature) through a septum using a syringe equiped with an hypdermic needle without disturbing the inert atmpshpere.

Following the specific synthetic prcodure corresponding to each particular NC type, NCs are typically “washed” in a process of precipitation by a poor solvent, followed by centrifugation, and redispersal in a good solvent. This washing procedure can be carried out multiple times, and, the resulting NCs will be designated “1X”, “2X”, etc. based on the number of washing cycles they have undergon.

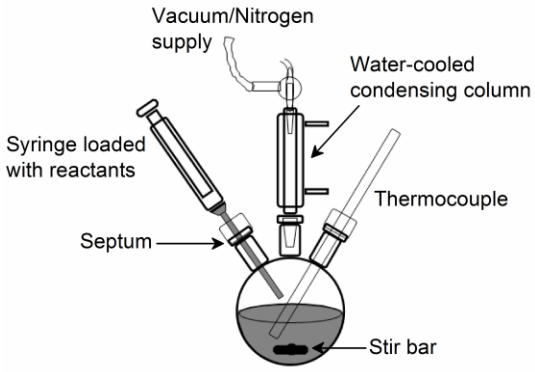

Figure 2.1: Diagram of NC synthesis apparatus.

2.2 Synthesis of Cadmium Selenide Nanocrystals

Synthesis of highly monodisperse cadmium selenide (CdSe) nanocrystals (NCs) was carried out using technique adapted from Murray et. al[29] and Yu et. al.[30] Common to all synthetic routes discussed below are four reaction components: a cadmium precursor, a selenium precursor, a coordinating solvent, and a ligand species. We will employ two categories of CdSe NC synthesis that utilize dimethylcadmium and cadmium oxide (CdO) respectively as the cadmium precursor. We will also explore the use of various coordinating solvents, which include 90 % purity TOPO (Sigma), 99 % purity TOPO (Sigma), and 90 % purity HDA (Sigma). The ligand species may be introduced deliberatley in the form of tetradecylphosphonic acid (TDPA, 97%, Strem Chemicals) or oleic acid (CdO precursor synthesis). Alternatively, if 90 % pure TOPO is used as the coordinating solvent, impurities such as phophonic acids [117], can be the source of ligand material. The selenium precursor in all cases is trioctylphosphine-selenium (TOP-Se).

2.2.1 Synthesis of CdSe NCs using Dimethylcadmium

The following synthetic technique was used to produce the CdSe NCs studied in Chapter 3 and Chapter 4. In a typical synthesis 12 g of coordinating solvent [90 % purity TOPO (Sigma), 99 %

purity TOPO (Sigma), or 90 % purity HDA (Sigma)] was added to a 50 mL three-neck flask. Depending on the exact synthesis, various mixtures of the above coordinating solvents were used, including 100 % TOPO (90%), 1:1 (by weight) TOPO (90 %)/ HDA (90 %), or 1:1 (by weight) TOPO (99 %)/ HDA (90 %). If 99 % purity TOPO was used, it was always necessary to add 0.75 wt. % of tetradecylphosphonic acid to act as an active ligand species (similar imipurities are know to already be present in 90 % purity TOPO)[117]. The contents of the flask were heated to 110 °C for 2 hours under vacuum. The solution was then heated to approximately 355 °C under a nitrogen atmosphere.

Separately, in an nitrogen-filled glove box, a solution of 1.0 M selenium (99.999%, Sigma) dissolved in trioctylphosphine (97%, Strem Chemicals) was prepared by stirring at 70 °C for 8 hours. 1.555 g of this TOP-Se solution was then mixed with 4.986 g trioctylphosphine and 0.15g of dimethylcadmium (99%, Strem Chemicals). The combined solution was loaded into a syringe and transferred out of the glove box. The TOPO/tetradecylphosphonic acid solution was allowed to cool and when the solution reached 350 °C the mixture of TOP/TOP-Se/$(Me)_2Cd$ was rapidly injected, causing the contents of the flask to change from clear to dark orange over the course of approximately 5 minutes, indicating the presence of CdSe nanocrystals. The temperature was allowed to stabilize at 280 °C and the solution held at this temperature for 20 minutes before cooling.

Approximately 10 mL of toluene was added to the flask at ~60 °C. The contents of the flask were then withdrawn and placed in two 50 mL centrifuge tubes. To each tube, 20 mL of methanol and 10 mL of acetone were added, causing floculation of the CdSe NC phase. The CdSe NCs were precipitated under centrifugation and redispersed in hexane.

2.2.2 Synthesis of CdSe NCs using Cadmium Oxide

This synthesis procedure was used to produce some of the CdSe NCs studied in Chapter 3. A solution of cadmium oleate was prepared by adding 0.2056 g (1.6 mmol) cadmium oxide, 4 mL of oleic acid (12.6 mmol) and 1 mL of octadecene to a 25 mL three-neck flask. The solution was degassed at 100°C for 30 minutes before heating to 240 °C under nitrogen. Above approximately 200 °C the oleic acid complexes with the cadmium ions and the solution turns clear. The optically clear solution was held at 240°C for 10 min and then cooled to room temperature.

7 g of TOPO (90%) and 7 g of HDA (hexadecylamine) (90%) were added to the original flask containing the cadmium oleate. The solution was then degassed at 100°C for 2 h. In order to reduce the presence of water generated from condensation of excess oleic acid with TOPO and HDA, the solution was heated to 210 °C under nitrogen for 5 min and then cooled to 100°C for an additional 1 hour of degassing. Finally, the solution was heated to approximately 310°C before removing heat and allowing the solution to cool. As the solution passed through 300°C, 8 mL of TOP-Se solution was rapidly injected. Heat was applied to the solution immediately after injection of TOP-Se and after an initial temperature drop the temperature was raised to 280°C and the solution is held at this temperature for 8 min before cooling.

When the NC solution reached 60°C approximately 10 mL of toluene was added and the combined liquid was withdrawn and divided between two 50 ml centrifuge tubes, each containing 5 ml of butanol (to prevent solidification of the now cool NC solution). 10 ml of acetone and 10 ml of methanol were added to each tube and then centrifuged. The precipitate was redissolved in hexane and once again centrifuged. The supernatant was recovered and filtered through a 0.2 micron pore size PTFE filter and stored in a nitrogen filled glove box. The final diameter of the CdSe NCs was determined using UV-vis absorption spectroscopy and confirmed with TEM analysis.

2.2.3 Synthesis of Phenylphosphonic Acid Terminated CdSe NCs

This synthetic procedure was used to produce the CdSe NCs studied in Chapter 6. Phenylphosphonic acid was used as a ligand for CdSe NCs by adapting the procedure described above for the synthesis of CdSe NCs via the dimethylcadmium route. 0.09 g (~0.75 wt. %) of phenylphosphonic acid (Sigma, 99%) was added to 12 g of TOPO (Sigma, 99%) in a 50 mL three-neck flask and heated to 110 °C for 2 hours under vacuum. The solution was then heated to approximately 305 °C under a nitrogen atmosphere.

Separately, in an nitrogen-filled glove box, a solution of 1.0 M selenium (99.999%, Sigma) dissolved in trioctylphosphine (97%, Strem Chemicals) was prepared by stirring at 70 °C for 8 hours. 1.555 g of this TOP-Se solution was then mixed with 4.986 g trioctylphosphine and 0.15 g of dimethylcadmium (99%, Strem Chemicals). The combined solution was loaded into a syringe and transferred out of the glove box. The TOPO/phenylphosphonic acid solution was allowed to cool and when the solution reached 300 °C the mixture of TOP/TOP-Se/$(Me)_2Cd$ was rapidly injected, causing the contents of the flask to change from clear to dark orange over the course of approximately 5 minutes, indicating the presence of CdSe nanocrystals. The temperature was allowed to stabilize at 250 °C and the solution held at this temperature for 20 minutes before cooling.

Approximately 10 mL of toluene was added to the flask at ~60 °C. The contents of the flask were then withdrawn and placed in two 50 mL centrifuge tubes. To each tube, 30 mL of methanol were added, causing precipitation of the CdSe NCs under centrifugation. These NCs could be redispersed initially in either toluene or hexane, however repeated washing results in a dramatic change of NC solublity and provides evidence of of the ligand population.

Two washing procedures were developed in order to elucidate the origin of the observed change in NC solubility with washing. If successive steps of methanol precipitation followed by (clean) hexane dispersion were carried out it was observed that 3X particles were no longer soluble in non-polar alkane solvents but are highly soluble in aromatic solvents such as chlorobenzene or toluene. This indicates that methanol washing gradually removes the alkylated TOP molecule (probably by oxidation of the phosphine head group), leaving a population of predominanlty phenylphosphonic acid ligands. When the TOP ligands are absent it is found that the NCs are stable for several hours and deposit well by EPD, but do not have a long shelf-life.

An alternative washing procedure was used in which the particles were dispersed in a solution of 2 vol. % TOP in hexane after each methanol precipitaiton step. Using this washing technique the NCs remain soluble in alkane solvents such as hexane indefinitely (> 10 X). We attribute the persistent solubility of NCs in hexane using this technique to the replenishment of the alkylated TOP molecule during each washing step. A similar technique may be used in which the TOP is substituted for diphenylphosphine (DPP), resulting in particles that are only soluble in aromatic solvents but exhibit a longer self life associated with improved surface pacivation.

2.2.4 Pyridine Ligand Exchange with CdSe NCs

Pyridine ligand exchange of CdSe NCs was carried out and the resulting NCs used to fabricate the NC-sensitized photovoltaic (PV) devices studied in Chapter 5. CdSe NCs synthesized via the dimethylcadmium route were first dispersed in hexane and precipitated with methanol under centrifugation. The solid precipitate was dispersed in pyridine (99% Sigma) under sonication at 60 °C over the course of 4 h. n-Hexane was added to the clear CdSe NC-pyridine solution leading to a cloudy suspension of flocculated NCs. This solution was centrifuged and the precipitate was again dispersed in fresh pyridine under sonication resulting in a clear solution. For NCs used in P3HT

photovoltaic devices n-hexane was added a final time to precipitate the CdSe NCs under centrifugation and the NCs were redispersed in a solution 1:2 solution of DCB/dibenzyl ether (DBE) (99%, Sigma).

2.3 Synthesis of Lead Sulfide NCs

2.3.1 Synthesis of Lead Sulfide NCs with Naphthoic Acid Ligands

In Section 6.1.2 we investigate films of naphthoic acid-terminated (-NA) lead sulfide (PbS) NCs deposited using EPD. These PbS-NA NCs were produced using a technique adapted from a procedure previously reported by Owen et al. for the synthesis of naphthoate-terminated CdSe NCs. First, a solution of lead naphthoate was prepared by combining 0.303 g of lead acetate trihydrate (0.8 mmol) with 0.414 g of 2-naphthoic acid (2.4 mmol) in 20 ml of dibenzylether in a three-neck reaction flask. The solution was heated to 130 °C under vacuum for 2 hours to remove water and the acetic acid byproduct before heating to 190 °C for 20 minutes under nitrogen. The contents of the reaction flask was cooled and the cloudy solution transferred to a 50 ml centrifuge tube and spun at 9000 RPM for 6 minutes to isolate the lead-naphthoate precursor from unreacted lead oxide and napthoic acid which precipitate as a solid pellet (to be discarded). After centrifugation the supernatant was placed in a clean 50 ml 3-neck flask, and heated to 70 °C under vacuum for one hour.

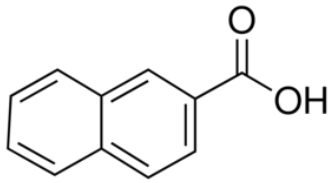

Figure 2.2: Molecular structure of 2-naphthoic acid.

Separately, in a nitrogen-filled glove-box a 1.0 M solution of tributylphosphine sulfide (TBP-S) was prepared by dissolving elemental sulfur in pure TBP. A 0.2 M solution of TBP-S was prepared by dilution of the 1 M stock solution with anhydrous DBE. 1 ml of the 0.2 M TBP-S/DBE solution (0.2 mmol) was then loaded into a syringe and transferred out of the glove box where it was immediately injected into the lead-naphthoate solution held at 70 °C. The reaction mixture gradually turns from brown to black over the course of approximately 10 minutes at which time the reaction is quenched by removal of the heating mantle and injection of 10 ml of anhydrous DBE.

The resulting naphthoate-terminated PbS NCs can be precipitated with methanol or ethylacetate and isolated with centrifugation. Toluene or chlorobenze were used to redisperse the NC precipitate and the resulting solution was stable for weeks.

2.4 Synthesis of Ammonium-terminated Zinc Oxide Nanoparticles

In Section 6.3 we show that zinc oxide (ZnO) NCs can be selectively deposited on lithographically defined electrodes using EPD to create structures useful for photovoltaic device applications. The ZnO NCs were synthesized using a technique adapted from Schwartz et al.[118, 119]. In a 250 ml Erlenmeyer flask 1.667 g of zinc acetate [$Zn(Ac)_2$] was added to 90 ml of dimethylsulfoxide (DMS) at room temperature with constant stirring to yield 0.101 M solution. A rubber stopper with an 8 mm diameter hole in the center was placed in the flask mouth. Through the 8 mm hole the drain of a 100 ml separation flask was inserted. A nitrogen blanket was applied through two needles (supply and exhaust) inserted through the same stopper.

Separately, a 0.552 M solution of ammonium hydroxide (NH_4OH) in ethanol (30 ml) was also prepared under nitrogen. The ammonium chloride solution was transferred to the 100 ml separation funnel (positioned over the $Zn(Ac)_2$ solution) and purged with nitrogen.

Under continuous stirring, the NH_4OH solution was added drop-wise to the $Zn(Ac)_2$ solution over a period of ten minutes, yielding a slightly cloudy white solution. The solution was stirred for an additional 40 minutes before being transferred to a glass vial for storage.

2.5 Characterization of Inorganic NCs

UV and visible absorption spectra of CdSe NCs were measured using an Agilent model 8453 UV-visible spectrometer. The PL spectra of CdSe NCs were recorded by excitation of solutions and films with a CW argon-ion laser (Melles Griot 400-A06) operated at 488 nm and detection by a Princeton Instruments Spectra Pro® 2300i spectrometer equipped with a model 7509-0001 liquid nitrogen cooled silicon CCD. Infrared absorption and PL by PbS NCs required use of a Princeton Instruments Spectra Pro® 2300i spectrometer equipped with a model 7498 liquid nitrogen cooled InGaAs photodiode array. For absorption measurements, PbS NC samples were illuminated by a Thor Labs model HPLS-30 white-light LED. Transmission electron microscopy (TEM) was carried out on a JEOL JEM 100CX operated at 100 kV.

2.6 Preparation and Treatment of Electrophoretically Deposited NC Films

In Chapter 3 and Chapter 4 of this thesis we will discuss the properties of films generated by the EPD of CdSe NCs using techniques described below. While the treatment of EPD films was kept constant, several different techniques were used to synthesize the CdSe NCs that comprise the EPD films themselves. For clarity, we will define here three separate techniques, described in Section 2.1, used to synthesize the various CdSe NCs examined in Chapter 3 and Chapter 4:

- **Batch I**: Cadmium oxide synthetic route using a 1:1 mixture (by weight) of TOPO (90%) and HDA (90%) as coordinating solvent. Oleic acid (from the cadmium oleate precursor) and TOPO impurities are expected to act as active ligand species. These NCs were found to have an average diameter of 3.5 nm using UV-vis spectroscopy and confirmed with TEM analysis.

- **Batch II**: Dimethylcadmium synthetic route using 1:1 (by weight) TOPO (99%) and HDA (90%) as coordinating solvent and 0.1 wt. % tetradecylphosphonic acid (TDPA) as the active ligand species. These NCs were found to have an average diameter of 3.2 nm using UV-vis spectroscopy and confirmed with TEM analysis.

- **Batch III**: Dimethylcadmium synthetic route using TOPO (99%) as coordinating solvent and tetradecylphosphonic acid (TDPA) as the active ligand species. These NCs were found to have an average diameter of 4.0 nm using UV-vis spectroscopy and confirmed with TEM analysis.

The EPD CdSe NC films studied in Chapter 3 and Chapter 4 were primarily produced using NCs from Batch III described above. Duplicate experiments and other miscellaneous studies [such as treatment of dried EPD films with TOPO solutions (Section 3.5)], utilized CdSe NCs from Batch I and Batch II described above.

2.7 EPD Electrode Fabrication

2.7.1 Unpatterned Electrode Fabrication

Unpatterned electrodes for EPD (Chapters 3-4, and Chapter 6) were fabricated using ~ 1" x 3" pieces of Si <100> wafers as the substrate. These substrates were cleaned via sonication in acetone, followed by IPA, and finally blown dry with nitrogen. 5 nm of chrome, followed by 50 nm of gold were then deposited on the polished side of the cleaned substrates using thermal evaporation.

2.7.2 Patterned Electrode Fabrication

The patterned electrodes for EPD of NCs discussed in Sections 6.2 and 6.3 were fabricated from Si <100> wafers with a 500 nm thick thermal oxide layer (SiO_2). The substrates were cleaned via sonication in acetone, followed by IPA, and finally blown dry with nitrogen. Using a spin-coater low molecular weight polymethylmethacrylate (PMMA, $M_N \sim 5k$) was applied from a solution of anisole to the clean oxide surface. The substrate was then baked at 130 °C for 20 minutes prior to spin-casting an additional layer of PMMA ($M_N \sim 96k$), followed by baking at 150 °C for 30 minutes. Electron-beam lithography (30 kV accelerating voltage) was used to expose selected regions of the PMMA film. After electron-beam writing the substrate was immersed in a developing solution of methyl isobutyl ketone to remove the regions of PMMA exposed to the electron beam. The patterned PMMA film (and substrate) was dried, and then loaded into a thermal evaporator where 5 nm of chrome, followed by 50 nm of gold were then deposited. Finally, the gold-coated substrate was immersed in a heated (70 °C) bath of acetone to remove the PMMA and over-lying metal, leaving behind the patterned gold on top of the thermal oxide layer.

2.7.3 Electrophoretic Deposition

EPD, used to produce the CdSe NC films studied in Chapter 3 and 4, was carried out under ambient conditions using ACS grade solvents as-received without further purification. 2 ml of stock 1X CdSe NC solution containing ~ 10 mg/ml NC was combined with 3 ml of clean hexane and then precipitated/dissolved in methanol/hexane three additional times in order to create a solution of NCs that had been reprecipitated a total of four times (4X). The multiple washing steps are known to reduce the number of ligands bound to the NC core surface and facilitate the EPD process.[46, 48] The 5X solution (5 ml) was combined with 40 ml of clean hexane in a 60 ml beaker open to air. Two pre-scored silicon electrodes (~7.6 cm × ~2.5 cm) coated with 50 nm Au and 10 nm Cr were

immersed in the deposition solution and held 2 cm apart (Au surfaces facing). A DC bias of 800 V was applied to the two electrodes for 10 minutes resulting in NC films on both electrodes.

2.7.4 TOPO Treatment of CdSe NC EPD Films

The EPD CdSe NC films studied in Chapter 3 were prepared according to the following procedure: Immediately after deposition, both positive and negative electrodes were quickly moved from the deposition solution to separate 30 mL baths of clean hexane. While fully submerged in hexane both electrodes were cleaved along preexisting score lines. Individual pieces of each electrode (~1 cm × ~1 cm) were rapidly moved from the clean hexane bath to new baths containing various concentrations of TOPO in hexane. Each sample remained in its respective bath (covered to prevent evaporation) for 30 minutes. Each sample was then removed from its respective bath and allowed to air dry.

2.7.5 Monomer Treatment and Polymerization of EPD CdSe NC Films

In Chapter 4 we investigate the properties of EPD CdSe NC films that were treated with various monomers and subsequently polymerized. To accomplish this, the as-deposited (wet) EPD NC films from one or both electrodes were quickly moved to baths of clean hexane. In most runs, the electrode was split along predefined score lines. One portion of the electrode was removed from this bath and allowed to dry in air under ambient conditions, and called the untreated film. The other portions were moved to separate baths of the given monomer (MMA, styrene, DVB, BDMA, HDMA, or DDMA) with 3 wt. % Irgacure 819 UV-initiator already dissolved in the monomer (monomer and initiator solutions were filtered using a 0.2 μm PTFE filter prior to EPD film addition). These films were allowed to soak in their monomer bath for 12 h, and after removal were spun for 6000 RPM for 1 min to remove excess monomer. Each film was subjected to UV radiation

from a high-pressure mercury lamp for 10 min under a nitrogen atmosphere. Polymerized samples were placed in the dark under vacuum for 24 h to remove any unpolymerized monomer.

2.7.6 Charaterization of EPD Films

The thickness of EPD CdSe NC films studied in Chapter 3 and Chapter 4 were measured with a Dektak mechanical profilometer. The elastic moduli and phase angles of films were measured using an Agilent G200 nanoindenter equipped with a standard diamond Berkovich tip oscillated at 40 Hz and driven to a depth of 1000 nm, with a tip advancement of 0.2 nm per cycle (8 nm/s). Elastic moduli were averaged from 200-250 nm into the films and were determined assuming a film Poisson ratio $\nu = 0.18$, but the obtained moduli were insensitive to the choice of ν used for data analysis. The PL spectra of EPD CdSe NC films was recorded by excitation of films with CW argon-ion laser (Melles Griot 400-A06) operated at 514 nm and detection by a Princeton Instruments Spectra Pro® 2300i spectrometer equipped with a model 7509-0001 liquid nitrogen cooled silicon CCD.

2.7.7 Preparation of P3HT Nanowire films

The P3HT nanowire films discussed in Chapter 5 were produced using the following procedure: a solution of highly monodisperse polystyrene (used as received from Polymer Standard Services) and poly-(3)hexylthiophene (used as received from Luminescent Technologies) was dissolved in dichlorobenzene (DCB) under an inert atmosphere conditions (in a nitrogen filled glove box). The P3HT content was held constant at 15 mg/mL while the PS:P3HT ratio was varied from 1 to 4. Unless otherwise stated, the molecular weight (MW) of PS was 10.4 kg/mol. After stirring for ~8 h at room temperature, the solution was spin-cast (1000 rpm for 60 s) on poly(3,4-ethylene dioxythiophene):poly(styrene sulphonate) [PEDOT:PSS] coated substrates. Silicon wafers

with native oxide were used as substrates for morphology studies. Glass substrates with patterned indium tin oxide (ITO, 5-15 Ω-cm-1) films were used for device measurements.

Immediately after spin-casting, films were subjected to solvent annealing with a DCB-rich atmosphere at room temperature for 1 h. The films were then baked at 135 °C for 30 min. After baking, films were submerged in a 1:2 solution of tetrahydrofuran:ethanol (THF/EtOH) for 30 min to remove the PS phase. Films were rinsed in pure ethanol prior to drying at room temperature. Finally films were baked at 70 °C for 30 min to remove any remaining solvents. For device fabrication these films were backfilled with an electron accepting material.

2.7.8 Preparation and Measurement of P3HT Nanowire Photovoltaic Devices

P3HT nanowire films were utilized in photovoltaic (PV) devices and the performance of these devices examined in Section 5.3. These devices were fabricated by spin-coating an acceptor material onto P3HT nanowire films located on patterned ITO substrates. The acceptor phase solution was made by dissolving 15 mg/mL of either PCBM (used as received from Luminescent Technologies) or pyridine-capped CdSe NCs[120] (~3.5 nm diameter, 10 mg/ml) in an orthogonal solvent consisting of 1:2 DCB:dibenzylether (DBE). These solutions were spun onto either planar P3HT films or P3HT nanowire mats at 800 rpm for 60 s and subsequently baked at 75 °C for 30 min. PV device performance was characterized under an AM 1.5 solar spectrum generated by a Newport Instruments 91160 light source (300 W Xe Arc lamp). The current-voltage (*I-V*) response was recored on a Keithley 2400 sourcemeter.

The patterned ITO substrates with P3HT nanowire/acceptor (PCBM or CdSe NC) films were then loaded into a thermal evaporator for deposition of the cathode. The deposition chamber was evacuated to a pressure of $< 2 \times 10^{-6}$ Torr and a 0.5 nm thick layer of lithium fluoride was deposited over the entire free surface of each substrate. After breaking vacuum the samples were briefly

removed from the deposition chamber and a mask was position over each substrate. The substrates were again loaded into the deposition chamber and the chamber was evacuated to a pressure of $< 2 \times 10^{-6}$ Torr. Finally, a 50 nm layer of patterned aluminum was applied to each substrate yielding six separate devices per substrate, each with an active area of 4 mm × 4 mm.

2.7.9 Morphology Charaterization of EPD P3HT Nanowire Films

The morphology of the P3HT nanowire films studied in Chapter 5 was characterized using a Hitachi 4700 scanning electron microscope (SEM) operated at 10 kV. For improved imaging resolution SEM samples were on samples coated with 1.8 nm Au-Pd. Surface contact measurements conducted using 8 μL drops of deionized water served as an indication of the effective surface area factor [cm2 of wetted P3HT per areal cm2]. AFM measurements were made using a ThermoMicroscopes model AP-0100 stage and a Si cantilever tip operated in tapping mode at approximately 15 kHz. Wide angle x-ray scattering (WAXS) measurements were performed at the Stanford Linear Accelerator Center (beam line 11-3) to investigate molecular packing within the P3HT nanowires as well as the PS matrix. WAXS data were collected for films of pure P3HT, blended films of PS and P3HT, and P3HT nanowire mats, with an incident angle of 0.10° and a detector distance of 400 mm.

3 Suppression of Fracture in EPD Films of CdSe NCs using Surfactant Molecules

3.1 Introduction

Electrophoretic deposition (EPD) of cadmium selenide (CdSe) nanocrystals (NCs) offers the ability to create dense, thick, and spatial selective NC coatings on conductive substrates.[121, 122] These films exhibit the unique properties of the constituent NCs, which may impart useful optical, electrical, or mechanical properties to the treated surface.[48, 123] These attributes could be utilized in applications such as photovoltaics (PVs), emissive displays, or mechanical surface treatments.[124] Posing the greatest obstacle to use of EPD NC films in such applications is the tendency of EPD NC films to fracture following deposition and subsequent removal from the deposition solvent. In this chapter we will examine a new process developed as part of this thesis whereby fracture of EPD CdSe NC films is suppressed by treatment of the as-deposited film with trioctylphosphine oxide (TOPO), an organic surfactant molecule utilized as both ligand and stabilizing agent (Figure 3.1). The as-deposited, wet, EPD NC films were soaked in TOPO solutions of hexane, and then allowed to dry. During TOPO treatment the TOPO molecules bind to vacant sites at the surface of NC cores. The added TOPO may also reduce "void volume" in the wet film (regions filled with deposition solvent) by displacing the deposition solvent. This treatment is found to reduce the strain (and stress) in the dry CdSe NC EPD film to a level at which fracture does not occur.

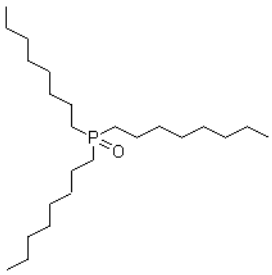

Figure 3.1: Molecular structure of trioctylphosphine oxide (TOPO).

The extent of strain that develops in a dried EPD NC film is strongly influenced by the fraction of film volume occupied by deposition solvent (hexane) in the as-deposited film. Solvent remains in the *in situ* EPD film, mixing with the ligands that cap the cores and within interstitial spaces between the NCs. In the several-step washing procedure needed to prepare the NCs to form the EPD films[47], a fraction of the capping ligands is removed[47, 125]. However, this washing procedure may increase the amount of this residual solvent, which will increase tensile strain in the dried film and the likelihood of fracture. Previous studies of fracture of EPD NC films have determined the in-plane tensile strain due to drying and observed the resulting fracture in real time.[126, 127]

In order to understand the mechanism of fracture suppression in EPD NC films it is necessary to understand the driving force for fracture: a decrease in equilibrium NC spacing that occurs upon drying of the as-deposited film. A balance between attractive inter-NC van der Waals forces and repulsive forces from ligand-ligand steric interference determine the equilibrium NC separation in the as-deposited (i.e. *wet*) film. As the film dries, and residual deposition solvent that remains between the TOPO-capped NC cores evaporates, the as-deposited equilibrium NC spacing is disturbed. NCs at the electrode surface are bound to the electrode and cannot reorganize to accommodate the change in van der Waals and steric forces. NCs away from the surface therefore experience an in-plane tensile strain as the equilibrium core spacing is reduced and NCs (bound) at the electrode surface act to resist an in-plane change of NC spacing. When the strain resulting from decreased NC spacing is large, the in-plane tensile stress applied to the film by the substrate is sufficient to cause channel-type fracture throughout the NC film (as seen in Figure 3.5 and later in Chapter 4). [45, 126, 127] Such fracture due to solvent evaporation also occurs in dry cast NC films.

In this chapter we will explore several phenomenon that influence the equilibrium NC spacing, and attempt to understand how treating EPD NC films with a TOPO solution leads to changes in this

equilibrium spacing. First we will examine the size (length) of the TOPO ligand when in the "wet" (i.e. in the deposition solvent) and when dry. By considering the ligand density at the NC core surface we arrive at an estimate of the NC ligand shell thickness before and after film drying. We will then address the possibility that the ligand shell of adjacent NCs intermix. By taking into account ligand shell thickness and interdigitation we can estimate the equilibrium NC core spacing, and from that knowledge estimate film strain.

3.2 Consideration of EPD Film Formation and Effects of Drying

During EPD, NCs are expected to form a dense but random three-dimensional structure. The term "dense" denotes that the NC core, along with the ligand shell, will come into direct contact with its nearest-neighbor NCs. Depending on the nature of the ligand shell, its thickness, and the extent to which adjacent ligand shells interpenetrate, the average separation between adjacent NC cores will differ. In our analysis we will assume the NC core diameter is fixed (i.e. a perfectly monodisperse NC core distribution), and that the ligand shells of all NCs are equivalent.

3.2.1 Consideration of Ligand Conformation Before and After Drying of EPD NC Films

When considering inter-NC spacing in a dense EPD film it is necessary to consider density of ligands bound to the average CdSe NC surface and the effective geometry of these bound ligands. Due to steric interference of adjacent TOPO molecules located on the same NC core, only a fraction of available binding sites on the NC core surface can be occupied. The fraction of occupied NC binding sites will be reduced for CdSe NCs that have undergone the rigorous washing process required to accomplish EPD (see Chapter 2).[45, 46]

The conformation of bound ligands will be a function of the environment to which the NC (film) is subjected. In a good solvent the ligand (TOPO) is expected to have an effective persistence

length that reflects a sterically hindered random-walk of the three alkyl chains. However, when a TOPO-capped NC is placed in a poor solvent (such as air), the TOPO molecules are expected to take on a compact conformation that minimizes the surface area of the high-energy TOPO-(poor)solvent interface in favor of the van der Waals interactions possible through inter- and intra-alkyl chain contact. Figure 3.2 depicts two possible conformations for ligands in the dry state corresponding to high and low ligand binding densities at the NC core surface. The thickness of the dry ligand shell is expected to be larger at high ligand densities as a result of increased ligand volume as well as steric interference of adjacent ligands leading to a more rod-like ligand conformation.

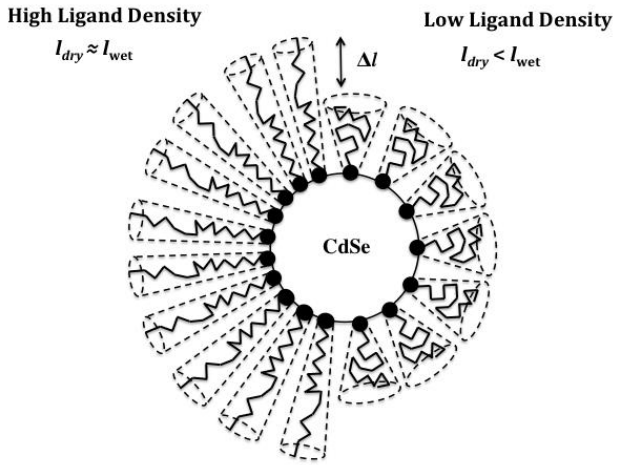

Figure 3.2: Depiction of increased dry ligand shell thickness resulting from high ligand density.

Utilizing previously determined values for the size of the TOPO molecule, we can set reasonable bounds on the physical characteristics of a TOPO ligand shell under different conditions (i.e. wet and dry). As depicted in Figure 3.4, we model the bound TOPO ligands on CdSe NCs in a good solvent (such as hexane) as in as truncated cones with 0.252 nm radius (0.2 nm^2 area, A_0) apex bases (or footprints) on the core, heights (ligand shell thickness, l_{wet}) of 0.99 nm (~ 1 nm), and base (swept-out) radii on the shell of 0.55 nm.[29, 128, 129] As a result of this assumed geometry and the steric hindrance between adjacent TOPO molecules that results, only a portion of available binding sites at

the CdSe NC surface can be occupied. Careful optical measurements have shown that, for CdSe NCs that are fully passivated by TOPO molecules, that approximately 30% of available binding sites are occupied[128, 130, 131] These results are consistent with the observation that ligand coverage increases for smaller cores with higher curvature and correspondingly reduced ligand-ligand steric interference.

With the above values in mind it is possible to estimate the total volume of ligand material that constitutes the ligand shell of a NC with radius *r* using Equation 3.1.

$$Total\ Ligand\ Volume\ (V_{Lig}) = 0.3\left(\frac{4\pi r^2}{0.2}\right)(0.53\ nm^3) \qquad \textbf{Equation 3.1}$$

More importantly, by assuming this ligand volume is a conserved quantity, it is possible using Equation 3.2 to estimate the thickness of the dry ligand shell, assuming the contracted ligands form a fully dense (0.831 g/cm^3) shell surrounding the core when dried.

$$l_{dry} = \left(\frac{3V_{Lig}}{4\pi} + r^3\right)^{1/3} - r \qquad \textbf{Equation 3.2}$$

As seen in Figure 3.3b, the dried ligand shell (l_{dry}) of a fully passivated (30 % TOPO coverage) CdSe NC is approximately 60% of the original ligand shell thickness when in a good solvent (l_{wet}). As the ligand coverage is decreased to 20% and 10%, the final thickness of the dry ligand shell (for a 4 nm NC) is reduced to approximately 43% and 24% of the original wet ligand shell thickness respectively. Another trend apparent in Figure 3.3a is that as the NC diameter is reduced, and the curvature of the NC core increases, the magnitude of ligand contraction (l_{wet} - l_{dry}) increases.

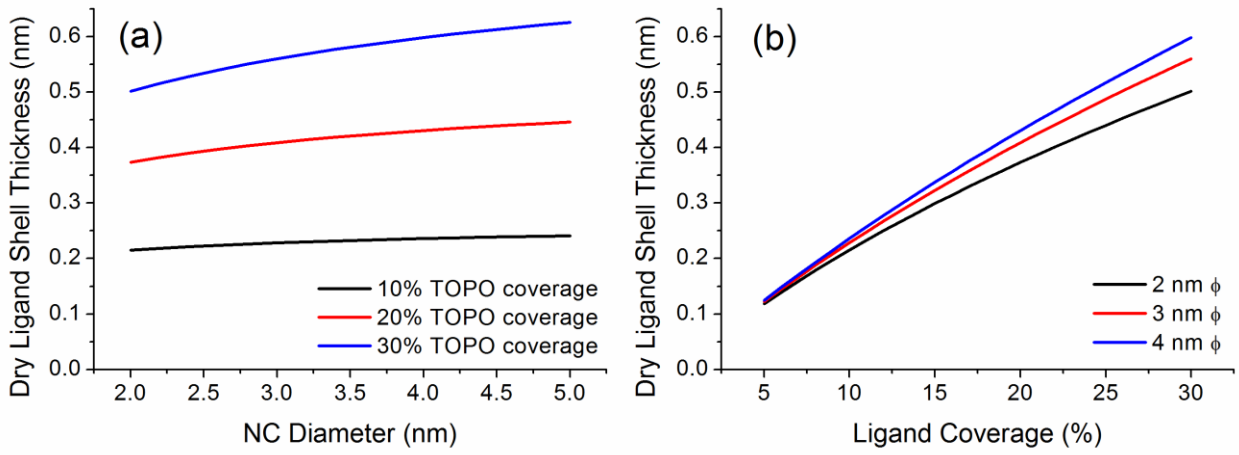

Figure 3.3: Estimated dry ligand shell thickness for TOPO-capped CdSe NCs.

For the washed NCs with fewer than the maximum number of ligands on the core, the ligand shell thickness is still ~1.0 nm in solution; however, the number of bound TOPO ligands will be reduced. Mulvaney et al. have shown that PL intensity from CdSe NCs is proportional to ligand coverage, providing a tool by which the ligand density on the CdSe NC core may be estimated.[128] As will be discussed below, PL measurements suggest that the as-deposited CdSe NCs have only 10-25% of the maximum (30%) ligand coverage. As seen in Figure 3.3b, the final thickness of the dry ligand shell is reduced when the initial ligand coverage is below saturation.

Before proceeding it is important to note that the above estimates of l_{dry} are low-end estimates. In reality the contraction of ligands in the dry state will be limited by steric effects resulting in a less than fully-dense dry ligand shell. Furthermore, the estimated molecular volume in this model (~0.52 nm^3) is smaller than the estimated molecular volume of TOPO (~0.71-0.80 nm^3, using a bulk density of ~0.8-0.9 g/cm^3 is typical of organic molecules). It is also important to note that recent work indicates the primary surface species of "TOPO-capped" CdSe NCs may be alkyl phosphonic acids,[31, 132] but the analysis here of TOPO ligands remains insightful and is applicable to the understanding of different organic ligand types.

3.2.2 Consideration of Interdigitation between Adjacent Ligand Shells

The above calculation of the dry ligand shell thickness assumes that each ligand shell dries independently, reaching full density in the dry state, and does not interpenetrate adjacent ligand shells. Under these conditions the cores of two NCs may approach to within $2l_{dry}$. A second possibility is that the ligand shells of adjacent NCs are not interpenetrating in the wet state, but become interdigitated upon drying. A third possibility is that there is some degree of ligand shell interdigitation in both the wet and dry state (but not necessarily the same degree of interdigitation). The amount of intermixing of adjacent ligand shell will have important consequences for NC core separation (a) and the strain that develops in dried EPD NC films. Figure 3.4 depicts the scenario in which there is partial interdigitation of adjacent ligand shells.

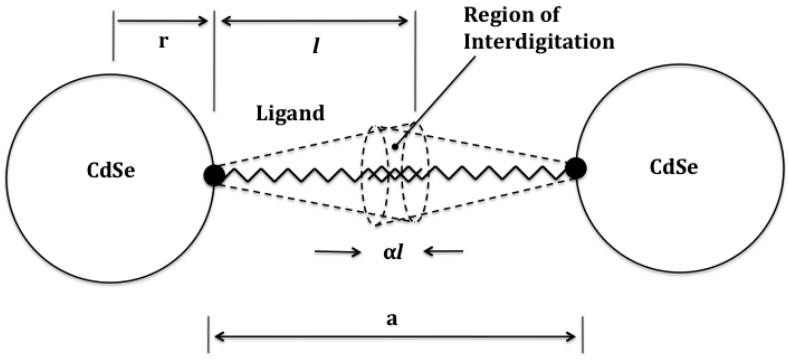

Figure 3.4: Interaction geometry of ligand-capped NCs with partial ligand interdigitation.

To facilitate our analysis we will introduce the variable α, which captures the potential for partial ligand interdigitation, where α can range from 0-1.0 for zero interdigitation and full interdigitation of adjacent ligand shells respectively. The separation between adjacent NC core surfaces can then be expressed using Equation 3.4 and Equation 3.5:

$$a_{wet} = 2l_{wet}\left(1 - {}^{\alpha_{wet}}/_{2}\right) \qquad \textbf{Equation 3.4}$$

$$a_{dry,eq} = 2l_{dry}\left(1 - {}^{\alpha_{dry}}/_{2}\right) \qquad \textbf{Equation 3.5}$$

Work in the field of grafted polymer brushes provides a means of estimating ligand shell thickness as well as shell interpenetration. Flory and Huggins[133, 134] showed that the effective volume and resulting persistence length (L) of a flexible organic molecule can be approximated by the expression $L \sim N^{\eta}$, where is the N is the number of repeat units in the flexible organic molecule and η is the Flory-Huggins Parameter that can range from 1/3 for a relatively dense self-interacting globular conformation, to 1/2 for a non-interacting Gaussian chain (in good solvent). Alexander and Manciu extended this work to grafted polymer brushes of various densities on rigid surfaces[135, 136] and showed that the average thickness of a grafted polymer brush could be approximated using Equation 3.6

$$\overline{D} \sim N(k\gamma)^{-\eta} \qquad \textbf{Equation 3.6}$$

where $\overline{D}$ is the average brush thickness (equivalent to l_{wet} or l_{dry} above), k reflects the preference of the brush for polymer-polymer interaction vs. solvent interaction, and γ is the areal density of grafted polymer brush. The value of η can fall between 0.25 and 0.33 at moderate graft densities for which there are strong steric interactions between adjacent organic molecules. The lower value of the η range (0.25) corresponds to a relatively sparse graft density while a η value of 0.33 reflects higher graft density. It is important to note the above equation is only applicable at graft densities below which the range in which brush thickness is dominated by N. Figure 3.2 illustrates how the value of γ, the ligand density at the NC core surface, may lead to an effective increase in the ligand shell thickness by imposing a rod-like ligand conformation in the dry state.

An important conclusion reached by Manciu is that as two grafted polymer brushes approach one another across a symmetry plane, there can be both attractive and repulsive forces corresponding to interdigitation or exclusion respectively. For good (and even moderately good)

solvents there is a strong repulsive force when two brushes interact at length scales shorter than the persistence length of the respective polymer chains. However, for very poor solvents (such as air) it is found that there is a strong attractive force between interacting brushes at short distances, corresponding to a high degree of interpenetration. This theory would therefore predict that during EPD (good solvent) NCs can approach to only within $\sim 2l_{wet}$ but that after drying the separation between NC cores ($a_{\mathrm{eq,dry}}$) may be as little as a single ligand shell thickness (l_{dry}), corresponding to full interdigitation of adjacent ligand shells.

Following the above arguments we predict that there is relatively little ligand shell interdigitation within the as-deposited EPD film, and that two NCs in good solvent may approach each other until their cores are separated by $2l_{wet}$ (~2 nm). However, for thoroughness, we will continue to consider the possibility that there is ligand shell interdigitation in the wet state (possibly due to electrophoretic forces or due to sparse ligand coverage).

In accordance with the work of Manciu[135, 136] we expect that the degree of interdigitation increases upon drying such that $\alpha_{wet} < \alpha_{dry}$. This assumption reflects the fact that as the deposition solvent evaporates intermixing of ligands becomes more energetically favorable as a result of the relatively high surface energy associated with the new ligand-solvent (air) interface and favorable van der Waals bonding available between ligands.

3.2.3 Analysis of Dry EPD Film Strain Based on NC Core Separation

Although we do not know the values α_{wet} or α_{dry}, we can consider several scenarios for α_{wet} and α_{dry} that are physically meaningful and span the maximum, minimum, and intermediate states of strain that are possible in the dried EPD NC film. The scenarios we will examine are:

(1) $\alpha_{wet} = 0$, $0 < \alpha_{dry} < 1$

(2) $\alpha_{wet} = \alpha_{dry}$, $0 < \alpha_{dry} < 1$

(3) $\alpha_{wet} = 1$, $0 < \alpha_{dry} < 1$

For a film composed of NCs with core radius r and equilibrium core separation $a_{dry,eq}$ in the dry state, the in-plane strain of the adhering dry film, where $a_{dry} = a_{wet} = 2l_{wet}(1 - 0.5\alpha_{wet})$, will be

$$\varepsilon = -\ln\left(\frac{2r+a_{dry,eq}}{2r+a_{wet}}\right) = -\ln\left(\frac{r+l_{dry}(1-0.5\alpha_{dry})}{r+l_{wet}(1-0.5\alpha_{wet})}\right) \qquad \textbf{Equation 3.7}$$

As a result of TOPO treatment the number of occupied ligand binding sites is increased and the volume of the ligand shell increases, leading to a corresponding increase in l_{dry} and $a_{dry,eq}$. We assume the presence of deposition solvent in the wet film maintains l_{wet} at ~ 1.0 nm. a_{wet} is therefore a function of α_{wet} only and is not influenced by ligand density at the core surface.

3.2.4 Analysis of EPD NC Film Thickness Based on In-plane Film Strain

In classical materials with a Poisson ratio ν, for plane stress conditions, the out of plane strain of a homogenous material can be expressed using Equation 3.8, where ε is the in-plane strain.

$$\varepsilon_{out} = \frac{-2\nu}{1-\nu}\varepsilon \qquad \textbf{Equation 3.8}$$

If NC solids were classical in this sense, then TOPO infusion would slightly increase the thickness of the dried EPD film by reducing the in-plane film strain (Equation 3.8 does not account for possible changes to ν that may occur with TOPO treatment). However, EPD NC films are not expected

to behave like classical homogeneous materials[137] and ν might be very small (and approach zero) as a result of the ligand phase and void volume between NC cores.

The measured thickness of a TOPO-treated EPD NC film will reflect the contribution of partial in-plane relaxation (Equation 3.8), as well as changes to the thickness of the NC ligand shells. The difference in film thickness (between films treated with different amounts of TOPO) can be quantified by applying Equation 3.7 and using the expression $\Delta h_{Lig} = h_0\varepsilon$, where h_0 designates the thickness of the fully relaxed (30 mM TOPO-treated) film. The total difference between measured EPD NC film thickness resulting from differences in ligand shell thickness and in-plane relaxation is described by Equation 3.9.

$$\Delta h_{tot} = h_0\varepsilon + h_0\left(\frac{-2\nu}{1-\nu}\right)\varepsilon = h_0\varepsilon\left(1 - \frac{2\nu}{1-\nu}\right) \qquad \textbf{Equation 3.9}$$

3.3 Analysis of the Elastic Modulus of EPD NC Films

3.3.1 Measurement of Elastic Modulus of EPD NC Films

The elastic modulus of CdSe NC films deposited using EPD can be directly measured using nanoindentation.[138, 139] Using Equation 3.10, where A is the contact area of the nanoindenter tip (standard Berkovich), E_r is the reduced modulus of the material $\left(\frac{1}{E_r} = \frac{1-\nu_i^2}{E_i} + \frac{1-\nu_s^2}{E_s}\right)$ and where subscripts *i* and *s* correspond to indenter and sample respectively, the elastic modulus of a 2-D film can be calculated from the slope of the unloading segment of the force-displacement curve.[140] Advanced analytical and empirical techniques have been developed to account for the instantaneous contact area (A) of the indenter tip as a function of indentation depth.[140]

$$\boldsymbol{E = \frac{2\sqrt{A}}{\sqrt{\pi}}E_r} \qquad \textbf{Equation 3.10}$$

It is evident from Equation 3.10 and the definition of reduced modulus (E_r) that it is necessary to assume a value of Poisson's ratio (ν) for the film as well as the indenter tip in order to calculate the film's elastic modulus. Although known, ν_i can be ignored because the elastic modulus of the diamond indenter tip is much larger than that of the film. For classical materials Poisson's ratio can range from 0-0.5. The value of Poisson's ratio for a fully-dense solid typically falls between 0.2 and 0.4 while the Poisson's ratio of a porous material can range between 0 and 0.3.[141] In this work we assume an intermediate value of 0.18 for Poisson's ratio for all EPD films. As will be shown below, the assumed value for Poisson's ratio of the EPD NC film does not substantially influence the estimates of film modulus.

3.3.2 Modeling the Elastic Modulus of EPD NC Films

We will use mean-field micromechanics models of multiphase materials to analyze the elastic modulus *E* for dried EPD films after TOPO treatment, composed of a filler (the NC core filler, CdSe), a matrix (TOPO ligands), and voids. In order to supply these models with the necessary inputs, we must make certain assumptions about the density of NC cores in the dry EPD NC film as well as the volume fraction of voids. Here we assume a packing fraction, *f*, of 0.58 for random loose-packed structures of hard spheres.[142, 143] The micromechanics models employed here also use the results of a recent study that showed how the elastic modulus of CdSe NC cores decreases with radius ($E_{\mathrm{CdSe}} \approx$ 21.5 GPa for the 2 nm radius cores here).[144]

To account for voids in the EPD NC films we apply a model developed by Christensen[145,146] in which the modulus of film (E_{film}) is a function of the void volume fraction (c_{void}) and modulus of the solid medium (E_m) according to:

$$E_{film} = E_m(1 - 2\beta c_{void}) \qquad \textbf{Equation 3.11}$$

for small c_{void}, where $\beta = 3(1-\nu_m)\,(9+5\nu_m)/4(7-5\nu_m)$ and ν_m is the medium Poisson ratio. For $0 \le \nu_m \le 0.5$, β is insensitive to ν_m and is ~1. For concentrated voids, $c_{void} \to 1$,

$$E_{film} = E_m\left[\frac{2(1-c_v)}{5+\nu_m}\right] \qquad \textbf{Equation 3.12}$$

After TOPO treatment and the possible local rearrangement of NCs, there are CdSe cores and TOPO ligands, and perhaps air voids. In the limit of dominating ligand steric repulsion, the NCs (core of radius r + ligand shell of thickness l) can be treated as hard spheres; for a free film the fractional volumes of the cores, ligands, and voids would be: $c_{CdSe} = f[r/(r + l)]^3$, $c_{TOPO} = f\{1-[r/(r + l)]^3\}$, and $c_{void} = (1 - f)$, where f is the packing fraction of NCs .

If the van der Waals attraction between CdSe NC cores dominates steric interference between ligand shells, adjacent ligand shells will intermix and the core separation will be less than 2*l* (Figure 3.14). If $l > (1/f^{1/3} - 1)r$, the ligands can fill all of the regions between the cores, with none of them in contact. This corresponds to $l \ge 0.40$ nm for 2 nm radius cores and f = 0.58, or ≥ 62% of the maximum ligand coverage of the core. In this regime: $c_{CdSe} = [r/(r + l)]^3$ and $c_{TOPO} = 1-[r/(r + l)]^3]$ For *l* = 0.6, 0.5, and 0.4 nm, c_{CdSe} = 0.45, 0.51, and 0.58, and c_{TOPO} = 0.55, 0.49, and 0.42, with $c_{void} = 0$. If $l < (1/f_{1/3} - 1)r$, the ligands cannot fill all of the voids even if the cores touch. Then, for minimum void fractions: $c_{CdSe} = f$, $c_{TOPO} = f\{[(r + l)/r]^3-1\}$, and $c_{void} = 1- f[(r + l)/r]^3$. For *l* = 0.3, 0.2, and 0.1 nm, c_{CdSe} = 0.58 (always), c_{TOPO} = 0.30, 0.19, and 0.09, and c_{void} = 0.12, 0.23, and 0.33, assuming minimum void volume.

Alternatively, we can use a different model developed by Halpin and Tsai to predict the modulus of a composite material.[147-149] According to the Halpin-Tsai model the bulk modulus of a two-phase composite film (K_{film}) will be:

$$K_{film} = K_{TOPO}\frac{1+\xi_K\eta_K\Phi_K}{1-\eta_K\Phi_K}, \qquad \textbf{Equation 3.13}$$

where $\xi_K = 4G_{TOPO}/3K_{TOPO}$ [= $2(1-2\nu_{TOPO})/(1+\nu_{TOPO})$ for particulate composites], $\eta_K = (m_K-1)/(m_K+\xi_K)$, and $m_K = K_{CdSe}/K_{TOPO}$, and the shear modulus G_{film}:

$$G_{film} = G_{TOPO}\frac{1+\xi_G\eta_G\Phi_G}{1-\eta_G\Phi_G}, \qquad \textbf{Equation 3.14}$$

where $\xi_G = (7-5\nu_{TOPO})/(8-10\nu_{TOPO})$, $\eta_G = (m_G-1)/(m_G+\xi_G)$, and $m_G = G_{CdSe}/G_{TOPO}$.

$$E_{film} = \frac{9K_{film}G_{film}}{3K_{film}+G_{film}} \qquad \textbf{Equation 3.15}$$

The modulus of the composite material, as predicted by Halpin-Tsai model (Equation 3.15), can be adapted to account for voids in the matrix phase (TOPO) using Equations 3.11 and 3.12, which we will then call the Halpin-Tsai-Christensen model.

3.4 Results

Unless otherwise noted, the results below were obtained for EPD NC films generated using CdSe NCs generated from Batch III described in Section 2.5. Untreated EPD CdSe NC films grown to a thickness of ~ 2.25 μm (> fracture thickness threshold)[127] exhibited a dense network of channel cracks across the film thickness Figure 3.5a and Figure 3.6a). Figure 3.5c-f and Figure 3.6c-f show that the TOPO treatment suppresses fracture in both positive and negative electrode films. When treated

with solutions of 5 mM and 10 mM TOPO, EPD CdSe NC films form fine cracks. Films treated with TOPO concentrations ≥15 mM do not crack.

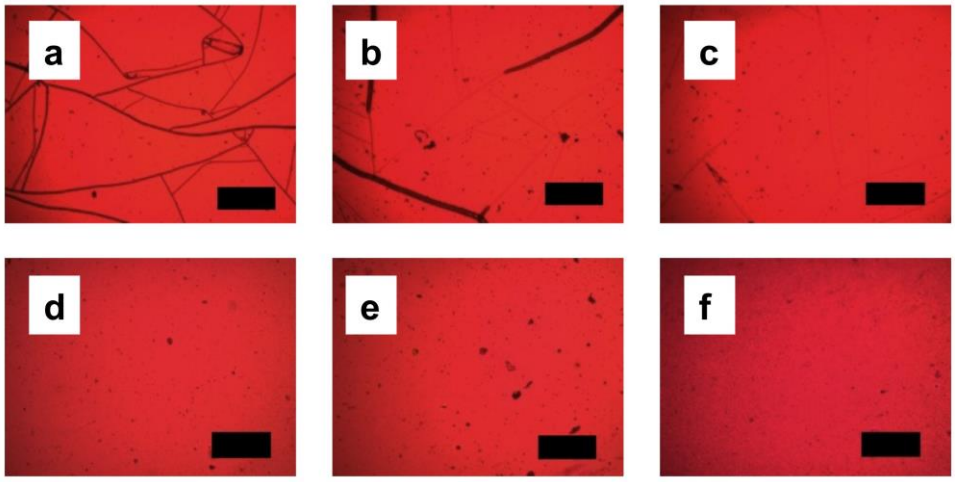

Figure 3.5: EPD CdSe NC (Batch III) film (negative electrode) treated with (a) 0 mM TOPO, (b) 5 mM TOPO, (c) 10 mM TOPO, (d) 15 mM TOPO, (e) 20 mM TOPO, and (f) 30 mM TOPO. The scale bar is 500 µm wide.

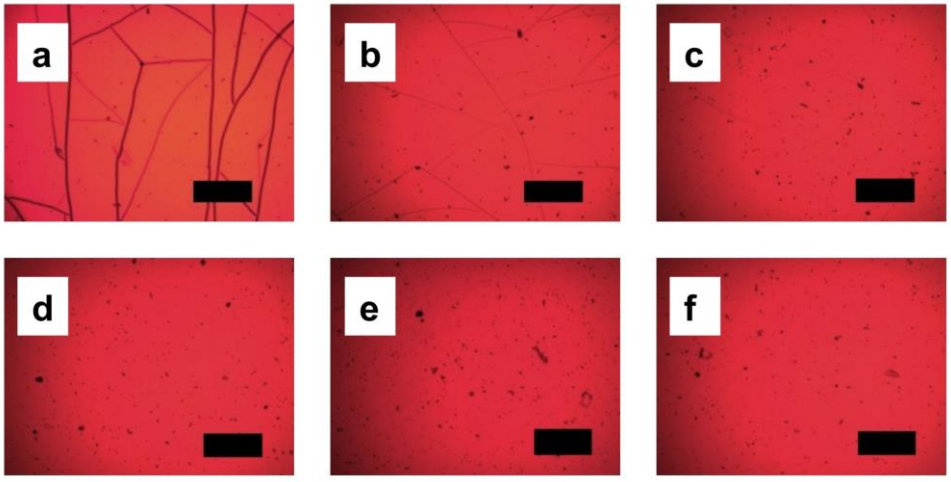

Figure 3.6: EPD CdSe NC (Batch III) film (positive electrode) treated with (a) 0 mM TOPO, (b) 5 mM TOPO, (c) 10 mM TOPO, (d) 15 mM TOPO, (e) 20 mM TOPO, and (f) 30 mM TOPO. The scale bar is 500 µm wide.

Figure 3.7 shows an increase in film thickness with TOPO concentration, of up to 38% (for 30 mM TOPO). Most of the change in film thickness occurs in treatments with ≤15 mM TOPO.

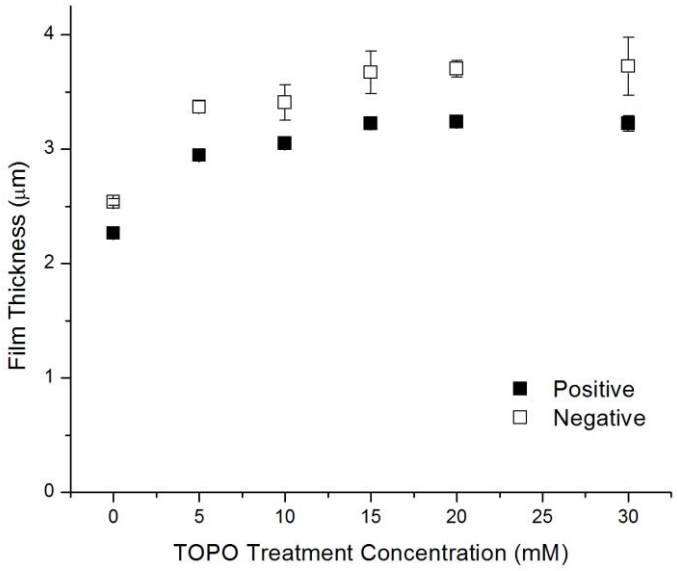

Figure 3.7: Thickness data for TOPO treatment of EPD CdSe NC (Batch III) films.

Figure 3.8 shows a typical nanoindentation trace for the negative electrode film using a standard diamond Berkovich indenter tip; those of the positive electrode are comparable. As can be seen, treatment of the wet EPD CdSe NC film results in softening of the dried film, without substantial effect on the viscoplastic response of the film (i.e. elastic recovery).

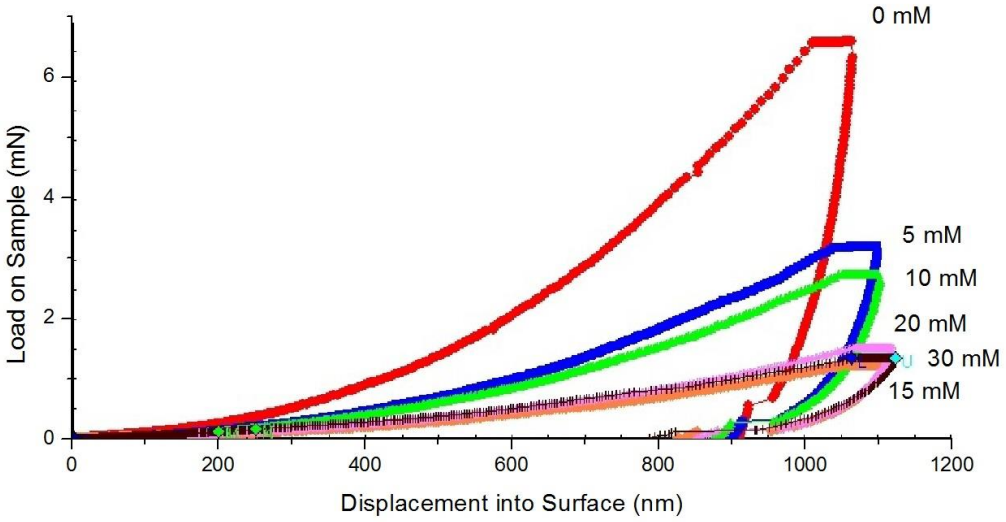

Figure 3.8: Load-displacement curves for TOPO treated EPD CdSe NC (Batch III) films.

The elastic modulus *E* of untreated EPD CdSe NC films ranges from 7.5 GPa to 9.5 GPa, as measured by nanoindentation; this is consistent with results from previous studies[150]. These dried films show a dramatic decrease in *E* upon treatment of films with TOPO (Figure 3.9a). Most of this softening occurs for treatment with < 15 mM. With this decrease in *E*, there is a concomitant increase in phase angle, and therefore viscoelasticity (Figure 3.9b).

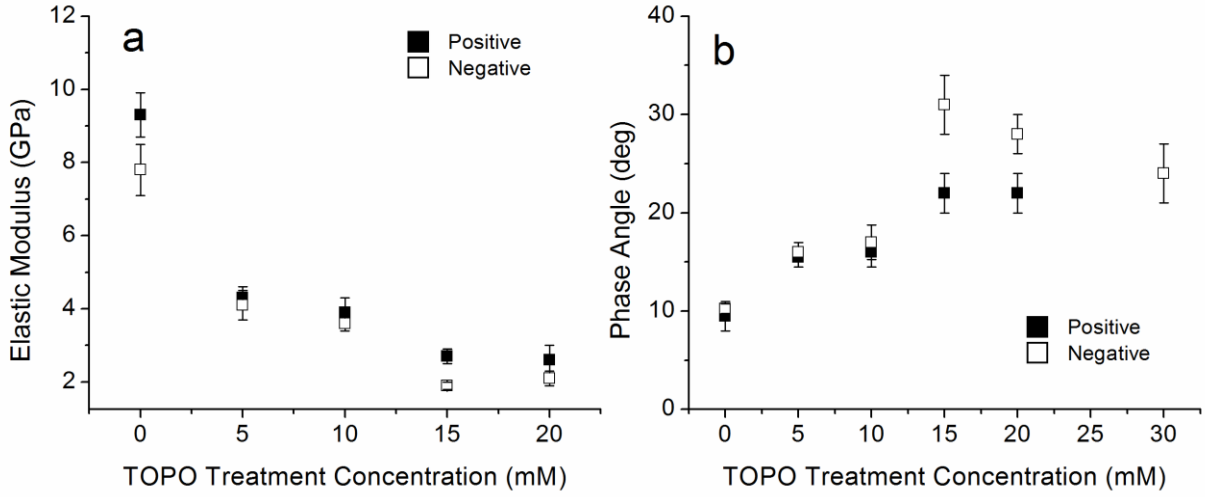

Figure 3.9: Influence of TOPO treatment on (a) elastic modulus and (b) phase-angle of EPD CdSe NC (Batch III) films.

TOPO solution treatment of EPD CdSe NC films greatly increases the NC photoluminescence efficiency. When treated with a solution of 5 mM TOPO, the PL signal increases by ~200% and ~1000% for the films grown on the positive and negative electrode films respectively. PL signals slowly increase with further increase in TOPO concentration and the increase saturates for TOPO concentrations of ≥15 mM. (The loss of PL intensity with 30 mM TOPO treatment, might be related to the pure TOPO deposits that accumulate on the film surface only for that condition.)

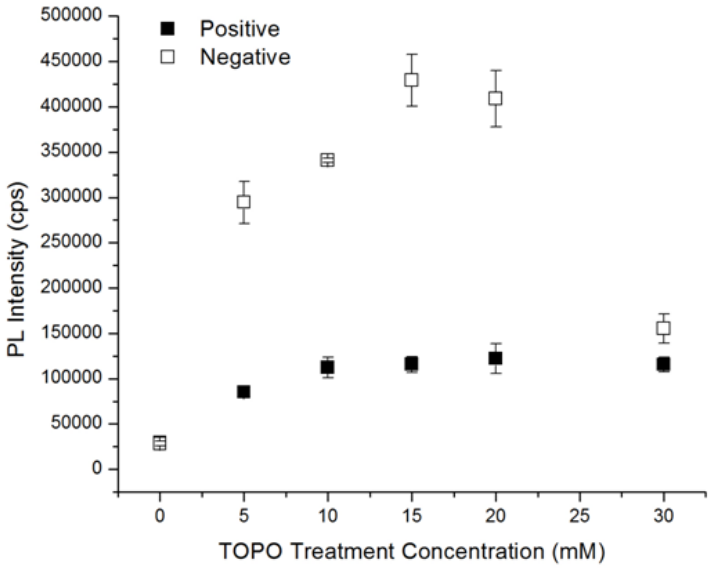

Figure 3.10: Influence of TOPO treatment on PL intensity of EPD CdSe NC (Batch III) films.

Figure 3.11 shows the nanoindentation trace of an EPD CdSe NC film (Batch I) that was allowed to fully dry (and crack) prior to treatment with a 30 mM TOPO solution. Optical micrographs reveal that the film remains cracked and is visually indistinguishable before and after TOPO treatment.

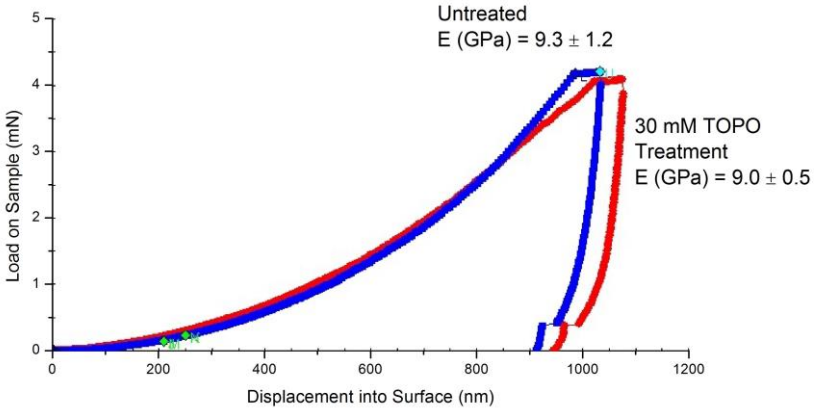

Figure 3.11: Investigation of TOPO treatment on modulus of dried EPD CdSe NC (Batch I) film.

PL intensity from the film is also essentially unchanged (Figure 3.12). We conclude that TOPO infusion into EPD CdSe NC films can occur in the wet, as-deposited film, but not in a film that has undergone drying and contraction.

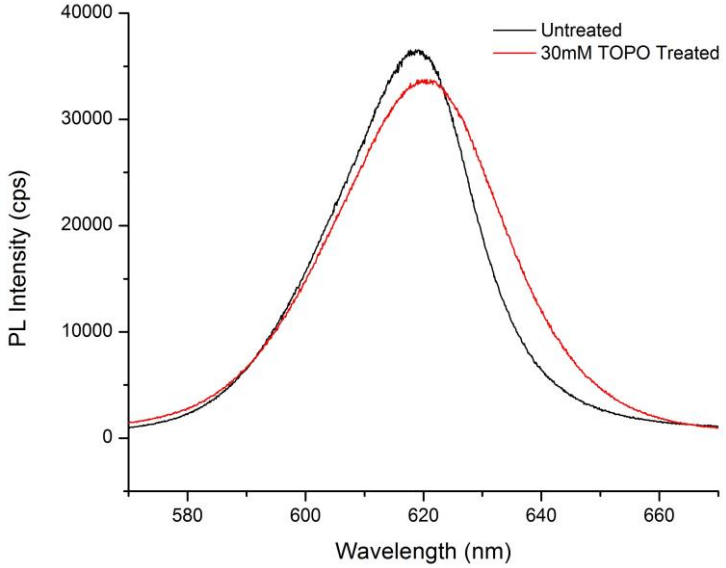

Figure 3.12: Comparison of PL intensity from TOPO-treated EPD CdSe NC (Batch I) film after it was allowed to dry and crack.

TOPO treatment of NC films formed by EPD of particles synthesized using slightly different procedures (Batch II, Section 2.6) yielded similar trends as those observed above. Figure 3.13 shows the optical and mechanical characteristics of a TOPO-treated EPD NC film deposited on the positive electrode. The CdSe NCs in this film were approximately 3.2 nm in diameter and synthesized without addition of phosphonic acid to the reaction mixture (as described in Chapter 2) thanks to impurities present in the 90 % pure TOPO used in that synthesis. The optical and mechanical measurements of this film show the same trends as other TOPO-treated EPD NC films: TOPO solution treatment reduces or, at high enough concentrations, suppresses film cracking, decreases film elastic modulus and increase viscoelasticity, and increases film photoluminescence. General increases in thickness with TOPO treatment concentration are seen (Figure 3.13a); however, there is more scatter in the

data in those runs, perhaps because of the differences in film preparation and/or the smaller sizes of the NC cores used. The films grown on the positive and negative electrodes have roughly the same thickness, and have similar properties that qualitatively change the same way with TOPO treatment. Of note, in each case they both do not fracture for ≥15 mM TOPO treatment.

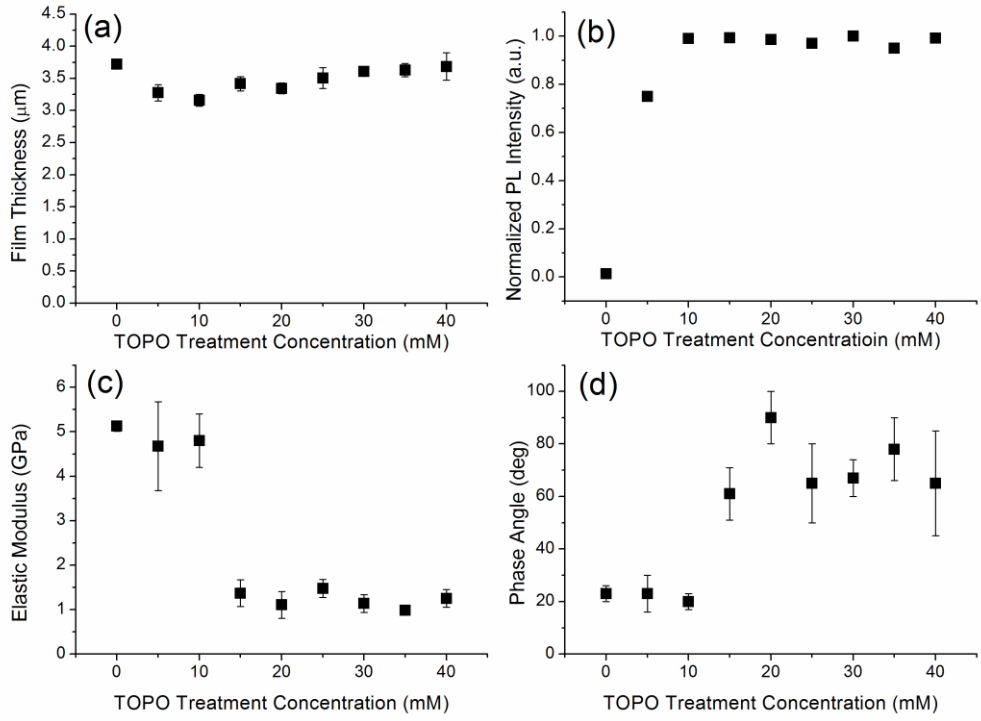

Figure 3.13: Effects of TOPO treatment on (a) thickness of EPD CdSe NC film, (b) PL intensity, (c) elastic modulus, and (d) phase angle during CSM mode nanoindentation. All data from EPD CdSe NC film deposited on positive electrode using NCs from Batch II.

Use of other ligands was briefly surveyed. Instead of treating the still wet TOPO-capped CdSe NC EPD film in TOPO solution, it was soaked in 30 mM hexadecylamine in hexane. The film quickly lifted off of the substrate and broke into very small pieces, and precipitated instead of redissolving fully into solution. In a separate experiment, the CdSe NCs were refluxed in hexadecylamine to change from TOPO to hexadecylamine ligands, but these NCs did not form EPD films.

3.5 Discussion

3.5.1 Overview of Film Properties

Treatment of EPD CdSe NC films was observed to have the following effects on all films investigated: lessened propensity to fracture, increased PL, decreased elastic modulus, increased viscoplasticity, and the general increase in thickness. These results indicate significant intake of TOPO into the film when it is treated while it is still wet, after formation. The changes are saturated when TOPO treatment concentrations are increased to ~10-15 mM. There does not seem to be significant TOPO intake into the film when it is treated after it has dried, likely because NC rearrangement after drying narrows the inter-NC regions.

Most of these changes could be due to increased density of TOPO bound to the cores and unbound in the voids. Only the increase in PL, due to surface passivation, is definitive proof that at least some of the infused TOPO increases ligand density bound to the cores. Moreover, since PL no longer increases for treatments > 15 mM TOPO, all available sites for capping ligands appear to be filled by treatment with 15 mM TOPO. It would not be surprising if most of the infused TOPO is bound to the cores.

There are clearly voids in the structure occupied by solvent while wet and air when dry. If not, there would not be large strains and fracture in the dried film and there would not be the apparently facile diffusion of TOPO into the wet film. However, if NC positions were the same before and after drying, with air voids merely replacing the solvent volume, with TOPO treatment a fraction of these voids merely being replaced by TOPO, TOPO treatment would then increase E according to micromechanics models (see below), rather than decrease it, as is observed, since E for TOPO exceeds that of air. This suggests that there could be (very local) rearrangement of NCs in the film during drying (particularly away from the substrate). This is considered below.

It is assumed that composition and properties do not change with depth into the film. It is possible that there is a gradient in TOPO diffusion and deposition and in film properties with depth into the film, and filling in the upper part of the film with TOPO could lessen diffusion to the film near the substrate. Although, this might play a role in a local rearrangement of NCs just mentioned, there is no reason to believe this dominates observations here, and it is not considered further.

3.5.2 Modeling EPD NC Film Strain Based on Ligand Effects

The observed changes in thickness of TOPO-treated EPD NC films suggest the films undergo a change of in-plane film strain upon TOPO-treatment (Equation 3.9). As previously discussed, strain in EPD NC films arises from changes to the equilibrium NC spacing (a), which in turn is a function of ligand density, ligand conformation (i.e. ligand shell thickness), and the degree to which adjacent ligand shells intermix.

In order to address the states of strain that can exist in a dried EPD NC film we will examine the equilibrium NC core spacing predicted for ligand densities (at the NC core surface) ranging from 10 – 30 % NC, and various degrees of ligand shell interdigitation corresponding to $0< \alpha_{wet} < 1$ and $0< \alpha_{dry} < \alpha_{wet}$. As previously noted, in the wet state, full interdigitation and zero interdigitation will correspond to a_{wet} = 1 nm and a_{wet} = 2 nm respectively. In reality we do not expect ligand shells in the wet state to fully interpenetrate, nor fully exclude adjacent ligand shells, but to reach an equilibrium state of partial interdigitation.

We will assume that in the as-deposited state $l_{wet} \sim 1.0$ nm. Provided an estimate of ligand shell interdigitation (α_{wet}), the NC core separation (a_{wet}) can be directly calculated using Equation 3.4. In the dry state the value of $a_{dry,eq}$ can be calculated using Equation 3.5, however, unlike in the wet state, we cannot a priori assume a value of l_{dry}. Instead we must apply the conservation of volume criteria to the partially intermixed ligand shell, and assume that each separate ligand shell is 50 % of

full density in the dry, intermixed, region; contributing to a fully dense ligand volume between adjacent NC cores. This requirement for full ligand density between NC cores in the dry state is expressed by Equation 3.14.

$$V_{Lig} = \frac{4\pi}{3}\left\{[(r + l(1 - 0.5\alpha))^3 - r^3] - \frac{1}{2}[(r + l)^3 - (r + l(1 - 0.5\alpha))^3]\right\}$$

Equation 3.16

For a given level of ligand coverage (0 - 30 %) and the corresponding value of V_{Lig}, α_{dry} and l_{dry} must satisfy Equation 3.16 while α_{dry} and a_{dry} must fall in the physically meaningful ranges of 0 - 1 and 0 - 1.0 nm respectively. By rearranging Equation 3.16 and using Equation 3.5 to substitute for l_{dry}, we find a third-order polynomial that describes the relationship between α_{dry} and $a_{dry,eq}$, resulting in the curves seen in Figure 3.14.

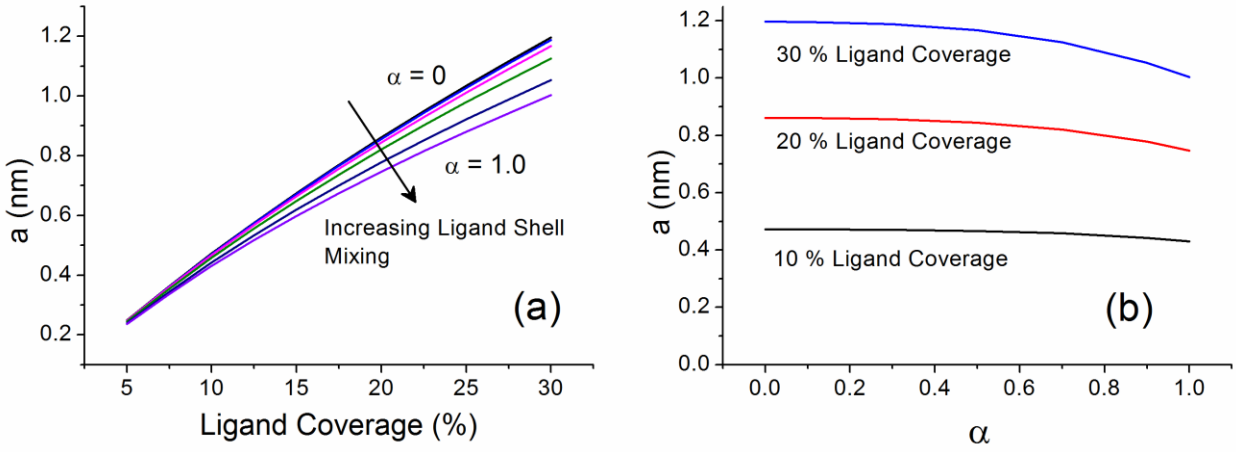

Figure 3.14: NC separation vs. ligand interdigitation.

It is apparent from Figure 3.14 that for low and moderate levels of ligand interdigitation ($\alpha < 0.6$), the equilibrium NC core separation in the dry film ($a_{dry,eq}$) is relatively insensitive to the degree of interdigitation and that values of $a_{dry,eq}$ are approximately equal to $2l_{dry}$ (Figure 3.3.) As the degree of ligand interdigitation in the dry film (α_{dry}) increases above 60 % there is a perceptible drop-off in $a_{dry,,eq}$. The magnitude of change in $a_{dry,eq}$ as a function of α_{dry} is less for smaller NCs and for NCs with

low ligand coverage. Figure 3.14b also shows us that the maximum and minimum core separation in the dry state corresponds to zero (α_{dry} = 0) and full ligand interdigitation (α_{dry} = 1) respectively.

In the absence of interdigitation in the wet and dry films, the values of a_{wet} and $a_{dry,eq}$ are $2l_{wet}$ and $2l_{dry}$ respectively, and Equation 3.7 reduces to $\varepsilon = -ln\left(\frac{r+l_{dry,eq}}{r+l_{wet}}\right)$. Figure 3.15a shows the magnitude of strain expected in the dry film for l_{wet} = 1.0 nm and α_{wet} = 0, where l_{dry} is calculated using from Equation 3.16. With interdigitation in the wet state the value of a_{wet} is reduced and the corresponding level of strain in the dry film is reduced. Figure 3.15b shows the influence of interdigitation in the wet state where it is assumed that $\alpha_{wet} = \alpha_{dry}$. Figure 3.15c depicts the extreme case in which α_{wet} = 1 (negative values of strain, corresponding to in-plane compression, are possible considered unlikely).

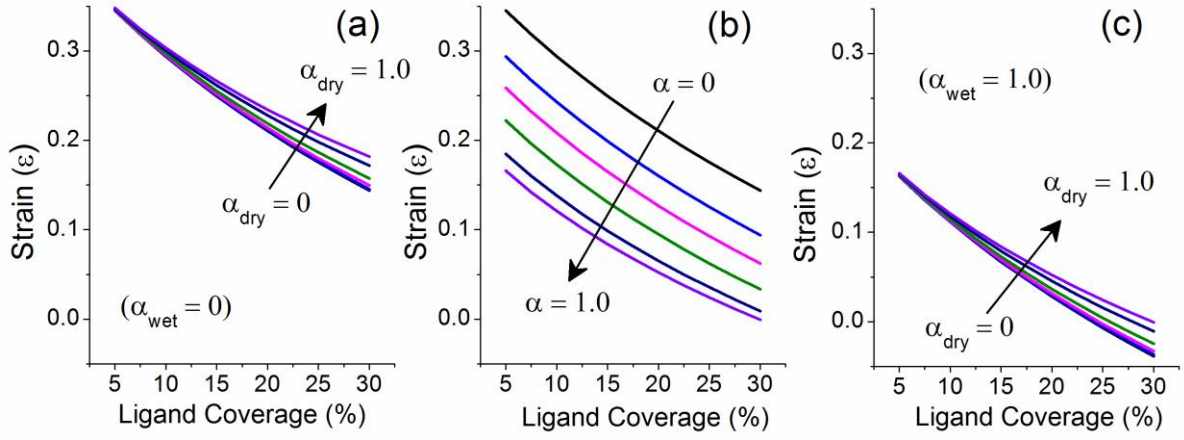

Figure 3.15: Strain in dried EPD film composed of 4 nm NCs where (a) there is no interdigitation of ligand shells in the wet state, (b) the degree of interdigitation in the wet and dry state are identical, and (c) there is complete interdigitation of ligands in the wet state. The arrows indicate curves of increasing α_{dry} including α_{dry} = 0, 0.3, 0.5, 0.7, 0.9, and 1.0 respectively.

It is apparent from Figure 3.15a and Figure 3.15b, that with or without ligand interdigitation in the wet state, that film strain in the dry state is expected to increase when ligand interdigitation in the dry state increases. From Figure 3.15b we see that when interdigitation in the wet and dry states are

identical ($\alpha_{wet} = \alpha_{dry}$) that strain in the dried film is expected to be reduced when the degree of interdigitation is increased.

3.5.3 Analysis of Film Strain Based on Thickness Measurements

In order to understand the affect TOPO treatment on EPD CdSe NC films we will compare predicted values of dry EPD NC film strain based (Figure 3.15b, $\alpha_{wet} = \alpha_{dry}$) with values of strain calculated from the thickness data shown in Figure 3.7 and Equation 3.9. In order to correlate TOPO treatment concentration with ligand coverage (as plotted in Figure 3.15), we utilize the PL data shown in Figure 3.10 (positive electrode) and assume that the PL intensity of the 30 mM TOPO-treated film correlates with full ligand coverage (30 %). The PL intensity of the untreated and TOPO-treated films is then assumed to be directly proportional to ligand coverage, leading to a predicted NC ligand coverage of 8 %, 22 %, 29 %, and 30 % for EPD CdSe NC films treated with 0 mM (untreated), 5 mM, 10 mM, and 15 mM TOPO solutions respectively. As can be seen from Equation 3.9, the assumed value of Poisson's ratio for the film (ν_{film}) will influence the magnitude of in-plane strain inferred from changes in film thickness. Figure 3.16 is consistent with the results of previous work[127] and suggests that as the magnitude of ν_{film} increases, the magnitude of dry film strain also increases, particularly when ligand coverage is low (based on consideration of PL measurements).

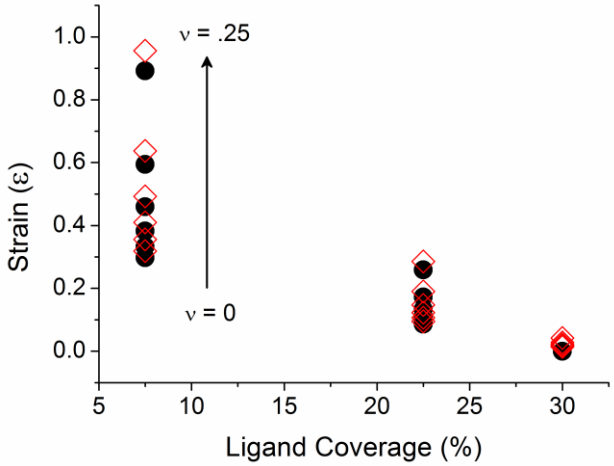

Figure 3.16: Influence of Poisson's ratio on (inferred) strain in dried TOPO-treated EPD NC (Batch III) films deposited on the positive (black circles) and negative (red diamonds) electrodes.

It is apparent from Figure 3.16 that a low assumed value of ν_{film} agrees most closely with the film strain inferred from thickness measurements. Figure 3.17 compares the same data shown in Figure 3.15b with values of dry film strain calculated using Equation 3.9 and an assumed value of ν_{film} = 0.05. We see that an assumed value of α_{dry} = 0 provides the best prediction of measured film strain (as inferred from thickness data) at low levels of ligand coverage (i.e. low concentration TOPO-treatment). At high levels of ligand coverage (i.e. high concentration TOPO-treatment) an assumed value of α_{dry} =1 provides the best prediction of measured film strain (as inferred from thickness data). These observations suggest that as ligand coverage increases, the degree of intermixing between adjacent ligand shell increases.

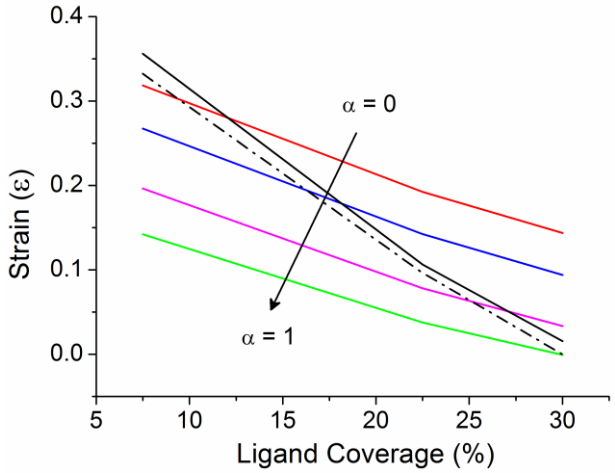

Figure 3.17: Comparison strain calculated for various levels of ligand interdigitation vs. strain inferred from measured thickness data of EPD of CdSe NC (Batch III) films formed on the positive (dashed black) and negative (solid black) electrodes.

3.5.4 Evaluating and Modeling EPD NC Film Modulus

For the discussion below we will assume a Poisson's ratio of 0.18 for all calculations. This assumption is supported by the results presented in Figure 3.18, where we show that our choice of ν_{film} does not affect our calculation of elastic modulus by more than ~ 10% in the range of ν = 0.15-0.35, suggesting that our choice of $\nu \sim 0.18$ is sufficient to draw meaningful conclusions regarding the elastic modulus of the films investigated.

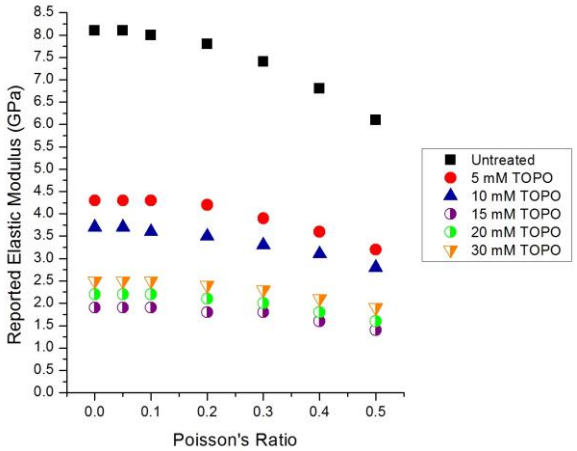

Figure 3.18: Influence of assumed Poisson's Ratio on calculated elastic modulus of EPD CdSe NC (Batch III).

Using the Christensen model, and assuming an elastic modulus (E_m) of 21.5 GPa (that of the CdSe core) for the dried EPD film we find that a void fraction of c_{void} = 0.42 for loose-packed CdSe cores, gives a film elastic modulus between 3.4 GPa and 4.5 GPa, as bounded by Equation 3.11 and Equation 3.12, which is lower than that measured. For packing fractions approaching close packing f = 0.74, Equation 3.11 is reasonably valid and gives an elastic constant ~10.3 GPa. This is more consistent with observations, but tight packing is not expected given that the NCs are not ordered and is not consistent with the large strains. Still, such films may be understood by an intermediate degree of core packing.

If the TOPO treatment merely replaced these air voids with TOPO in the still wet EPD films, then E would be larger in the dried treated films than in the dried untreated films because of this and because the fractional volume outside the voids would be expected to decrease. Since a decrease is seen, either the TOPO treatment leads to some rearrangement of NCs and the volume fraction of NC cores decreases or, less likely, the additional TOPO softens the existing TOPO matrix (decreases the elastic modulus).

The two-phase (CdSe core "filler" and TOPO medium) Halpsin-Tsai model[148] micromechanics model was used with E_{CdSe} = 21.5 GPa for r = 2 nm. For NC core separation in the dry film (a_{dry}) ranging from 1.2 nm (maximum ligand coverage) to 0.8 nm, E_{film} increases from 2.0 to 2.7 GPa when E_{TOPO} = 0.8 GPa; this range is consistent with the results of Figure 3.9b. These results are not very sensitive to CdSe core elastic modulus or the core and Poisson ratios. Similar estimates of E_{film} can be obtained assuming E_{TOPO} = 1.02 GPa 10% void volume when treated by using the Halpin-Tsai-Christensen three-phase model (Equation 3.15). For a_{dry} ranging from 0.6 nm to 0.2 nm and E_{TOPO} = 0.8 GPa, the Halpin-Tsai-Christensen model (with minimum voids) gives a film modulus (E_{film}) of ~2.4-2.5 GPa; again this range is consistent with the results of Figure 3.9a. Results are also consistent

with measurements when larger void fractions are assumed if larger values of E_{TOPO} are used. It is noted that the predictions of other micromechanics models (Cohen-Ishai[146], Mori-Tanaka[151], and Christensen-Lo[151]) can vary by ~20%; such model variations do not affect the main conclusions of this study

The somewhat smaller elastic modulus of the untreated EPD film presented in Figure 3.13 is explained in part by the smaller NC core radii (and their smaller elastic moduli[144], E_{CdSe} ~17 GPa and 14 GPa for the 1.75 nm and 1.6 nm radii). The somewhat smaller measured values of the elastic modulus after these films are treated with TOPO (~1.3 GPa) are modeled using their different core sizes and a slightly smaller value of E_{TOPO}, ~0.6 GPa.

Previous nanoindentation analysis of EPD films[126] of CdSe NCs found the elastic modulus was E = ~8-10 GPa, which is consistent with what is measured here. (E was found to be much smaller, ~2-2.5 GPa, after cross-linking the NCs in the EPD film, followed by treatment to remove the TOPO ligands, presumably because of much replacement of TOPO by voids, and possibly also larger voids due to larger inter NC core spacing.) In a related study[126], the elastic modulus of TOPO in EPD CdSe NC films was estimated to be 2.45-4.41 GPa, by using Raman spectroscopy and fracture patterns. [144]

For drop cast assemblies of NCs, the elastic modulus was found to be ~6 GPa for 2D array membranes of Au NCs (capped by dodecanethiol)[152] and ~0.2-6 GPa for a range of NC supercrystals[153], ~0.84 GPa and ~2.16 GPa for CdSe NC films and supercrystals. The effective elastic modulus of the matrix (outside the cores) was estimated to be ~0.1-0.7 GPa for a range of ligand matrices, with ~0.22 GPa for TOPO in CdSe NC films and ~0.71 GPa for TOPO in CdSe NC supercrystals.[153]

3.5.5 Consideration of Fracture in Strained EPD CdSe NC Films

According to classical fracture theory, cracking occurs in the film whenever the Griffith's criterion[154] is met during any stage of drying. This criterion for channel cracks is the critical film thickness

$$h_c = \frac{\Gamma E}{(1-\nu^2)Z\sigma^2} = \frac{\Gamma(1-\nu)}{(1+\nu)ZE\varepsilon^2} \qquad \textbf{Equation 3.17}$$

where σ and ε are the in-plane film stress and strain (with $\sigma = \varepsilon E/(1-\nu)$); E, ν, and G are the film elastic modulus, Poisson ratio and toughness; and Z is a parameter = 1.98 for channel cracks[155]; each of these parameters, except Z, changes during drying.

TOPO treatment of the EPD NC films may prevent fracture, effectively increasing h_c, because of one or more of the following mechanisms:

(1) Decrease of strain due to added capping ligands: The added bound ligands decrease in-plane film strain in the dried film, and likely in-plane stress also. This appears to be important in suppressing fracture. While it is difficult to assess the influence of TOPO treatment on ligand shell thickness and potential void filling, the increased PL with TOPO treatment proves that some (if not most or all) of the added TOPO binds to the NC cores.

(2) Decrease of strain due to added ligands in interstitial regions: Interstitial regions of the as-deposited film (occupied only by deposition solvent in the wet film without TOPO treatment) could be filled with unbound TOPO (void filling), reducing film contraction. This may be important (see above).

(3) Decreased film elastic modulus: The film E is seen to decrease, so σ would decrease even if ε did not (within and near the linear stress-strain regime). This may be important, but only if it is not accompanied by a decrease in fracture strength.

(4) Increased film toughness: The infusion and coordination of TOPO likely increases ligand interdigitation. This would increase van der Waals forces and likely increase film toughness (Γ), which would help suppress fracture.

(5) Film overcoating: If the EPD film were over-coated or encapsulated by a film of TOPO, this could reduce the density of nucleation sites in the EPD film and suppress fracture; however, there is no evidence of this. (However, after treatment with the highest TOPO concentration solutions, TOPO crystals do appear on the surface.)

Other mechanisms might be significant as well. Film viscoelasticity increases with TOPO treatment, but it is not clear if this is important in suppressing fracture. TOPO passivates surface defect sites, which appears to increase the local fracture toughness above the critical fracture threshold. In untreated films, cracks usually originate from small points that appear as black or dark red spots in the film, which may be dense aggregates of poorly passivated NCs. The density of these sites decreases with TOPO treatment, indicating that such passivation does occur; however, they still exist and fracture still occurs at the lowest TOPO concentrations.

3.6 Conclusions

When large strains and fracture arise after drying of EPD films formed from NCs with incomplete ligand shells on the core, the mechanical state of the film can be substantially improved by recapping the core with ligands before film drying. Specifically, it was seen here that treating EPD CdSe NC films with TOPO solutions reduces or suppresses cracking, and concomitantly increases film thickness a bit, reduces the elastic modulus of the film, and greatly increases film photoluminescence.

While this treatment reduces film strain greatly, there still may be some small residual strain. Film electrical conductivity might also be controllable by the choice of the coordinating ligand that is infused; increasing charge conductivity would be important for several applications of EPD NC films, such as for solar cells[156] and field-effect transistors. The work presented in Chapter 4 shows that fracture can also be suppressed by infusing molecules that do not cap the NC cores into the EPD NC film before it dries, specifically monomers that are later polymerized. [157]

The work discussed in this chapter has been published:

T. J. Kramer, S. K. Kumar, M. L. Steigerwald, and I. P. Herman, *J.Phys. Chem. B,* **2012,** 117, 1537

4 Polymer Stabilization of Electrophoretically Deposited CdSe NC Films

4.1 Introduction

Thick electrophoretically deposited (EPD) films of ligand-capped colloidal nanocrystals (NCs) are highly photoluminescent (PL) and deposit with high spatial selectivity on patterned conductive substrates.[45-47] Unfortunately the untreated EPD NC films that deposit on both electrodes typically crack when dried due to the evaporation of the deposition solvent, a decrease in film volume, and the corresponding strain that develops as a result of film adhesion to the rigid substrate. Previous work has shown that when an untreated EPD film of cadmium selenide (CdSe) NCs is thicker than ~ 600-800 nm, the dried film is likely to fracture,[45, 126, 127] making the resulting film unsuitable for nanoscale functionalization of most devices. In Chapter 3 we showed how fracture of thick EPD NC films could be avoided by infusing a solution of trioctylphosphine oxide (TOPO) capping ligands into the EPD film before solvent drying. The resulting films did not crack, and showed enhanced PL efficiency, but had a greatly reduced elastic modulus and decreased elasticity.[157]

In an effort to avoid EPD NC film fracture while preserving the mechanical EPD film properties, a technique discussed in this chapter has been developed in which fracture of thick (several um) EPD films of CdSe NCs is suppressed by treating the wet, as-deposited EPD films with various polymer precursor molecules (i.e. monomers). The liquid monomer displaces the deposition solvent and, upon polymerization, forms a non-volatile matrix surrounding the NC cores. Fracture is suppressed for one or both of two possible reasons: reduction of film strain (associated with preservation of the equilibrium NC spacing in the as-deposited state), or by an increase in film toughness. Both mechanisms for fracture suppression of EPD NC films will be discussed in this

chapter. The resulting EPD NC/polymer composite films show uniform NC dispersion, exhibit increased PL efficiency, enhanced elasticity, and, depending on the monomer (polymer), have an elastic modulus equal to or greater than an equivalent untreated film.

4.2 Monomer Selection

To completely infiltrate the EPD NC film and effectively displace the deposition solvent, the selected monomers should have good miscibility with the NC ligand shell (TOPO). The monomer should not evaporate prior to polymerization, and should be easily polymerized using free radical UV-polymerization to avoid the complications associated with high-temperature thermal free-radical polymerization. The resulting polymer should be non-volatile and have sufficiently high molecular weight (MW) to impart mechanical strength to the resulting composite film. To target these goals, the monomers methylmethacrylate (MMA), styrene (Figure 4.1a), divinylbenzene (DVB, (Figure 4.1b), butanedioldimethacrylate (BDMA), hexanedioldimethacrylate (HDMA), and dodecanedioldimethacrylate (DDMA, (Figure 4.1c)) were used to treat the still-wet EPD films. Methylmethacrylate and styrene are monofunctional monomers that polymerize to form long chain-like polymer molecules. DVB, BDMA, HDMA, and DDMA are difunctional monomers that form three-dimensional cross-linked elastomeric networks.

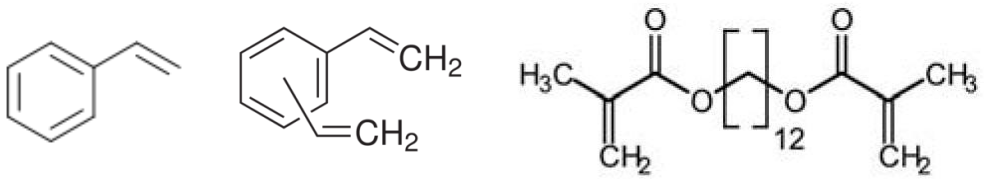

(a) (b) (c)

Figure 4.1: Chemical structure of (a) styrene, (b) divinylbenzene, and (c) dodecanedioldimethacrylate.

The monomers investigated in this chapter are not known to bind with the surface of CdSe NCs and presumably diffuse into the voids between the NC cores under the influence of steep concentration gradients. Depending on the size and composition of the monomer molecule the EPD CdSe NC film may swell to varying degrees, but in no cases was complete film dissolution observed. For monomers that cause relatively little film swelling, the packing density of NCs remains high. In several cases the film becomes much thicker as a result of this treatment.

4.3 Background on Polymerization of Monomers

The physical and chemical attributes of each monomer will lend the final polymerized product certain unique attributes. Each monomer molecule that participates in the polymerization process contributes a single repeat unit to the polymer chain (or network). By virtue of one or more "functional units" a monomer molecule is able to form a covalent bond with one or more other monomer units, forming a polymeric chain (in the case of a monofunctional monomer), or a polymeric network (in the case of a difunctional monomer).

The use of free-radical UV-polymerization was selected for this work (as opposed to thermal free-radical polymerization) for practical experimental reasons. Thermal free-radical polymerization often utilizes a peroxide additive and temperatures exceeding 90 °C to generate the free-radicals that drive the polymerization process (these polymerization additives are called *initiators*).[158] By contrast, UV-initiated polymerization utilizes UV-activated photoinitiators to generate free-radicals and can accomplish polymerization at ambient temperatures.[158] Provided the full volume of material to be polymerized can be effectively illuminated by UV light, UV-polymerization is a facile and robust method for generating polymer films.

As seen in Mechanism 4.1, when the initiator molecule (I) absorbs a photon of sufficient energy, one or more free radicals are generated (R^*). If one of these free radicals encounters a

monomer molecule (M) with an easily cleaved double bond (typically a C=C bond) the initiator breaks the double bond and creates an activated R-M* molecule in which the unbound electron now resides on the monomer portion of the molecule. When the R-M* molecule encounters an unreacted monomer the free-radical again cleaves the double bond of the monomer molecule and attaches the new monomer to the polymer chain, producing an R-M-M*. This process can continue until many (> 10^6) monomer units have been added to a single polymer chain.

$$I + h\upsilon \rightarrow 2R^*$$

$$R^* + M \rightarrow R{-}M^*$$

$$R{-}M^* + M \rightarrow R - M{-}M^*$$

$$R - (M)_n{-}M^* \rightarrow R - (M)_{n+1}{-}M^* \qquad \textbf{Mechanism 4.1}$$

The properties of a polymer resulting from free-radical polymerization are strongly influenced by the concentration of the free-radical initiator.[159] An important consideration during free-radical polymerization is the phenomenon of polymerization termination through reaction of two free-radical species with one another to yield an unreactive species (Mechanism 4.2). In some cases two initiator radicals can react with one another (to form an unexcited initiator molecule) before either radical participates in a polymerization reaction.

$$R - (M)_n{-}M^* + M^* - (M)_n - R \rightarrow R - (M)_{2n} - R \qquad \textbf{Mechanism 4.2}$$

The concentration of free-radical initiator is therefore an important factor in the polymerization process. By selecting a low initiator concentration the likelihood of free-radical annihilation can be reduced, but also lowers the population of actively growing polymer chains (and increases monomer availability). A low initiator concentration therefore leads to polymers

with high MW.[158, 160] Polymers with high MW often exhibit favorable properties such as improved solvent stability and increased mechanical strength.[161] The primary disadvantage to using a low initiator concentration is a slow polymerization rate and reduced reaction efficiency attributed to unreacted monomer that trapped in regions where there is no initiator. The presence of residual monomer is also known to degrade the mechanical properties of the resulting polymer if not removed.

By contrast, a high initiator concentration can facilitate rapid polymerization and reduce the probability of unreacted monomer in the final product; however, the large population of actively growing polymer chains results in reduced monomer availability, and increased frequency of polymerization-termination reactions, and produces a polymer with lower MW. The effect of initiator concentration on MW of a polymer can be understood by examining the influence of initiator on monomer concentration (Figure 4.2). The polymerization rate of actively growing chains will be directly proportional to the concentration of monomer. As seen in Figure 4.2 the concentration of monomer decreases more rapidly at higher initiator concentrations, leading to reduced rate of polymer growth, and a lower MW polymer for a given polymerization reaction time.[162]

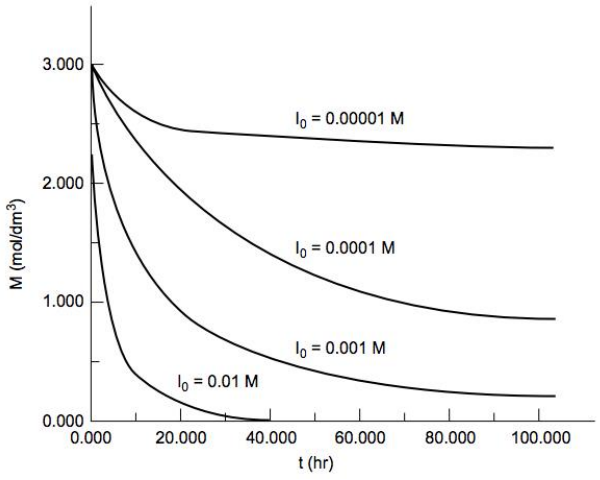

Figure 4.2: Monomer concentration vs. time for hypothetical polymerization reaction.[162]

Not all polymer molecules resulting from the same polymerization reaction will have the same size, making it important to define the average MW of a polymeric material. Several definitions for the average MW of a polymer exist, but the number-average molecular weight (M_N) and weight-average molecular weight (M_W) are two of the most common. In this thesis we will use M_N when discussing the molecular weight of a polymer.

$$M_N = \frac{\sum M_i N_i}{\sum M_i}$$

$$M_W = \frac{\sum M_i^2 N_i}{\sum M_i N_i} \qquad \textbf{Equation 4.1}$$

The concept of M_N can be misleading when discussing cross-linked polymer networks because it is possible, with difunctional monomers, to create a network polymer with an effective M_N that approaches infinity (i.e. the entire polymer is a single molecule). Polymers of this type are called *elastomers* and exhibit elastic recovery even at high (>> 100 %) levels of strain.[163, 164] This property can extremely valuable in mechanical applications requiring dissipation of mechanical energy without permanent deformation of the material (as in car tires, vibration dampeners, etc). While some elastomers are generated reaction of a single monomer precursor, it is also possible to simultaneously polymerize a monofunctional monomer with a difunctional monomer, creating covalent linkages between adjacent polymer chains that would otherwise have only van der Waals bonding. Figure 4.3 depicts the cross-linking of polystyrene with DVB, a common polymer used in ion-exchange resins.[165]

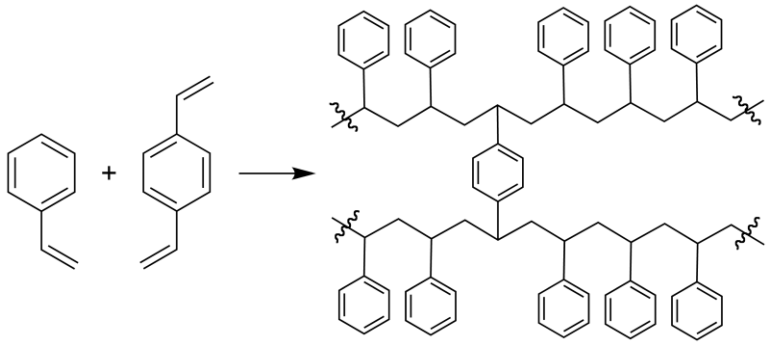

Figure 4.3: Cross-linking of polystyrene using divinylbenzene.

4.4 Behavior of Monomers and Polymers in a Composite Material

Several monomer and polymer characteristics will be important to the performance of the final composite NC material. During the initial stage of monomer infusion, the solubility of the NC phase in the monomer phase will influence the thickness of the final NC-polymer composite film. Following polymerization, the mechanical properties of the film will be strongly correlated with the mechanical properties of the polymer. In this chapter we will explore the effect of polymer stabilization on EPD NC films by consideration of the complex modulus of the visco-elastic polymer phase (E^*, Equation 4.4)[166], and by application of a mean-field micromechanics model to analyze the elastic modulus of the two-phase polymer composite.

4.4.1 NC Solubility in Monomers and Polymers

By assuming NCs in the as-deposited EPD film correspond to a polymer of infinite M_W, we can use the Flory-Huggins parameter (χ) to describe the solubility of as-deposited NCs in the monomer during treatment.[133, 160] We can then use Equation 4.2 to determine χ and from that infer the degree to which the as-deposited film swells upon monomer treatment. It is apparent

that a large value for the Flory-Huggins parameter corresponds to favorable mixing between the monomer and NC phase, leading to a low NC loading fraction (ϕ) in the final polymerized film.

$$\chi = -\ln\left(\frac{1-\phi}{\phi^2}\right) - \frac{1}{\phi} \qquad \textbf{Equation 4.2}$$

The Flory-Huggins parameter (χ) can also be related to the difference in solubility parameters of the two phases according to Equation 4.3, where δ_m and δ_{NC} are the solubility parameters of the monomer phase and NC phases respectively.

$$\chi \propto (\delta_m - \delta_{NC})^2 \qquad \textbf{Equation 4.3}$$

Equation 4.3 shows that the Flory-Huggins parameter (χ) will increase in magnitude as the difference in solubility parameter for the monomer (δ_m) and NCs (δ_{NC}) increases.

4.4.2 Mechanical Properties of EPD NC-polymer Composite Films

As previously mentioned, the mechanical properties (strength and rigidity) of a polymer typically increase with M_N. As the size of the average polymer molecule increases, mechanical failure of a polymer (i.e. tearing) becomes more difficult as a result of increased van der Waals bonding between polymer molecules as well as the entropic energy penalty associated with elongation of individual polymer chains.[163] Figure 4.4 depicts a common relationship observed between the strength of a polymer and the polymer molecular weight, where S_∞ is the strength of the polymer with infinite MW, and A is a scaling factor.[167]

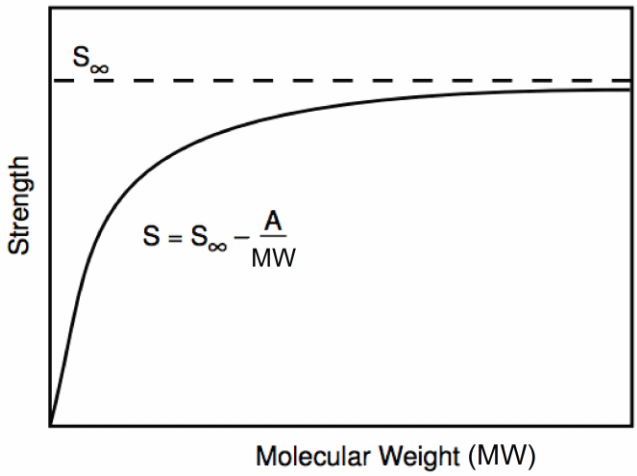

Figure 4.4: Strength vs. MW for a hypothetical polymer.[167]

The mechanical response of perfectly viscoelastic polymer (i.e. an elastomer) can be described by a spring and dashpot in parallel (the Kelvin-Voigt Model).[164] Alternatively, a spring and dashpot in series can be used to model the response of a perfectly viscoplastic polymer.[164] In both models the concept of complex elastic modulus (E^*) applies:

$$E^* = E' + iE'' \qquad \textbf{Equation 4.4}$$

where E' is the storage modulus, and corresponds to elastic deformation of the material in phase with the applied stress. E'' is the loss modulus, corresponds to deformation of the material out of phase with the applied stress, and reflects a materials ability to dissipate energy during loading. The relative magnitude of E'' and E' is described by Equation 4.5, where ψ is the phase-angle. A large phase-angle during cyclic loading of a polymer therefore corresponds to high damping.

$$\tan(\psi) = \frac{E''}{E'} \qquad \textbf{Equation 4.5}$$

Cross-linked polymers are characterized by a relatively small phase angle, attributed to reduced inter-chain sliding and a high degree of elastic recovery. The value of ψ is known to change inversely with cross-link density[161, 163, 164] while *E'* typically increases with cross-link density.[164] Alternatively, polymers without covalent cross-links are known to have a relatively high loss modulus associated irreversible chain movement and permanent plastic deformation. Typically the higher the molecular weight of a polymer the greater the energetic barrier to polymer chain reorganization, resulting in an increased value of E' and a reduced value of ψ.[164, 168]

Typically the higher a polymer's M_N the greater the degree of inter-chain entanglement and the greater the (instantaneous) stress required to accomplish a given level of strain in the material. The density of cross-link points in an elastomer will also influence the elasticity of the material, with higher cross-link density corresponding to higher modulus and greater elastic recovery. Various models exist to predict the strength and elasticity of a composite material based on the properties of the constituent matrix (polymer) and filler (NC) phases. As discussed in Section 3.3.2, we will use the Halpin-Tsai model to analyze the elastic modulus of polymer-stabilized EPD NC films comprised of a NC and organic binder phase.

4.5 Results

As described in Chapter 2 all EPD CdSe NC films were deposited simultaneously on pre-scored gold-coated Si substrates (positive and negative electrodes) at a bias of 800 V with electrodes positioned 2 cm apart. Unless otherwise noted, all films were deposited using NCs from Batch III. The average CdSe NC diameter was 4.0 nm as determined by UV-Vis absorption spectroscopy[8] and confirmed using transmission electron microscopy. For each monomer a non-polymerized sample (i.e. initiator-free monomer treated and not exposed to UV light) was made in

order to differentiate effects of the monomer treatment from effects of the subsequent polymerization step. All monomer-treated films were subjected to a vacuum drying step carried out at < 10^{-3} atm for 6 hours to remove residual solvent and unpolymerized monomer. Nanoindentation was used to study the mechanical properties of polymer-stabilized films. The relative stiffness of each film (untreated, monomer-treated, and polymerized) can provide qualitative information about the structure of the film. PL measurements were conducted to probe the impact of the polymer phase on the passivation of NC surface. By measuring film thickness using mechanical profilometry it was possible to estimate film swelling and the relative solubility of the NC phase in the monomer (and eventual polymer) phase. Microtoming was used to directly image the distribution of NCs through the thickness of polymer-treated EPD NC films.

Cracking was suppressed across the CdSe NC EPD film in all samples that had been treated with DVB, BDMA, HDMA, and DDMA and then polymerized, as seen in the optical micrographs in Figure 4.5. The resulting polymer-stabilized EPD films are stable and do not show evidence of cracking even after four years of storage in air under ambient conditions. After soaking in MMA or styrene, there was no fracture during the early stages of drying. However, once the excess monomer overcoating the film was removed by spinning, fracture resulted over all of the MMA-treated films and over much of the styrene-treated films, prior to UV polymerization, likely because of evaporation of these highly volatile monomers. Profilometry and nanoindentation measurements were made in the mm-dimension regions of styrene-treated films that did not crack. Films treated with styrene/DVB mixtures did not crack over the entire film.

Figure 4.5: Optical micrographs of (a) 3.8 mm-thick untreated, control EPD film and EPD films treated by (b) DVB, (c) BDMA, (d) HDMA, (e) DDMA, and then polymerization (negative electrode film). Scale bars are 100 μm wide.

Films were also briefly examined after monomer infusion, but without polymerization. Films treated with DVB and BDMA, but not polymerized, eventually fracture under vacuum, likely due to monomer evaporation. HDMA and DDMA films do not crack without polymerization even in vacuum for long times, likely because of very low monomer volatility – which is also coupled to good interactions between the monomers and NCs. Only the polymerized films are analyzed in detail below.

All of the treated and polymerized films are thicker than the untreated EPD films, which could be due to swelling or encapsulation by the polymeric material. DVB- and BDMA-treated films are only somewhat thicker than the untreated control, while the HDMA-treated and DDMA-treated films are much thicker than the control (Figure 4.6).

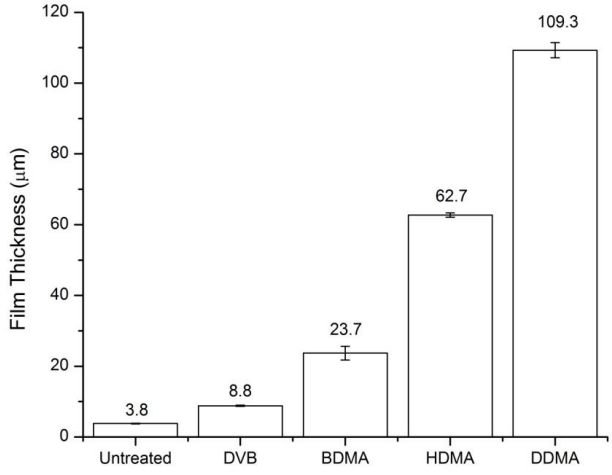

Figure 4.6: EPD film thickness after monomer treatment and polymerization (negative electrode film).

Figure 4.7 shows a TEM of the upper regions of the DDMA-treated film after ultramicrotoming, which suggests the NCs are dispersed in this (thickest) film. This suggests that NCs are homogeneously dispersed in each NC/polymer composite film, with no polymer overlay that is devoid of NCs.

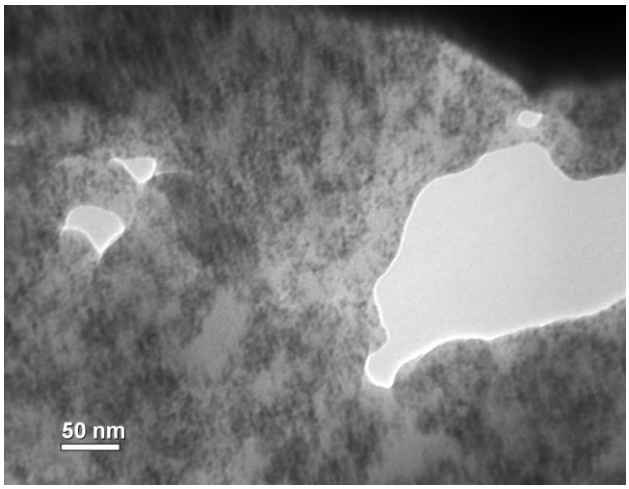

Figure 4.7: TEM of EPD film after DDMA-treatment, polymerization, and ultramicrotoming (negative electrode). Note that the sample chipped due to the ultramicrotoming.

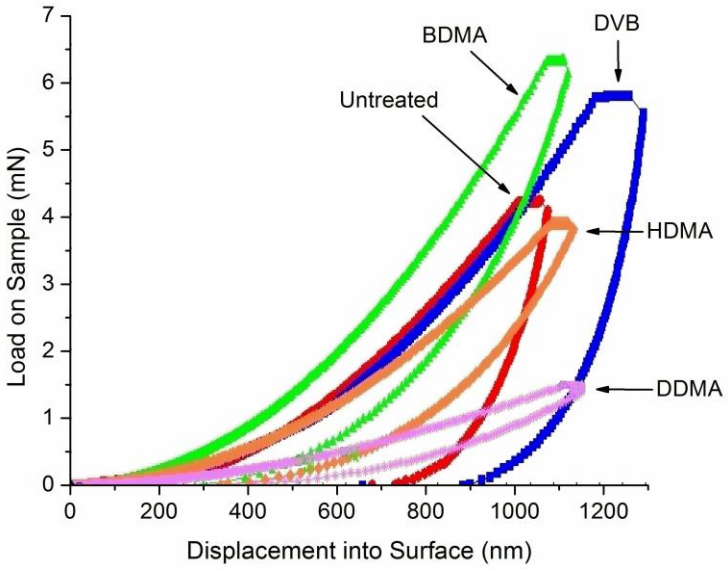

Figure 4.8: Force-displacement curves for monomer-treated and polymerized EPD films of CdSe NCs.

The elastic moduli of monomer-treated and polymerized films were estimated from force-displacement curves of the type seen in Figure 4.8 (see Chapter 3 for discussion of the elastic modulus calculation).[169, 170] Of note is the high degree of elastic recovery present in the BDMA-, HDMA-, and DDMA-treated films. It is apparent from Figure 4.9a that the elastic moduli of DVB- and BDMA-treated films are roughly equal to that of the untreated films, while the elastic moduli of HDMA- and DDMA-treated films are much smaller lead than that of the untreated films). Styrene-, BDMA-, HDMA-, and DDMA-treated films have a larger phase angle (are more viscoelastic) than the untreated films, while the DVB-treated films has a phase angle comparable to that of the untreated film (Figure 4.9b). The reduced phase angle of the DVB-treated film is consistent with the previous discussion of phase angle and demonstrates the importance of cross-link density on the complex modulus of a polymer. In each case, the elastic modulus and phase angle are nearly equal to that of films of the pure polymer, indicating that the mechanical properties of the composite films are dominated by the organic phase.

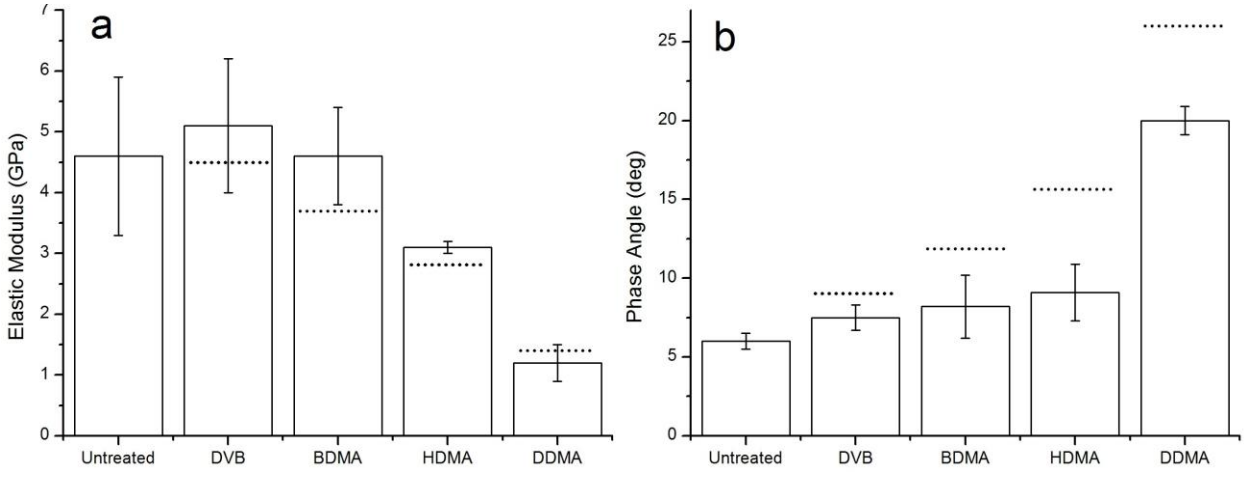

Figure 4.9: (a) Elastic modulus and (b) phase angle of EPD films after monomer treatment and polymerization along that for the untreated film for each sample (negative electrode). Data are also shown for the pure polymer films as dashed lines.

Films treated by varying fractions of DVB and styrene were thicker and softer (lower elastic modulus) than the untreated films, and were thicker, with larger elastic modulus with more DVB, for films formed on both electrodes (Figure 4.10, Figure 4.11a). This last result is unsurprising, given that DVB can crosslink the polymer matrix and thus increase the modulus.[164] Styrene, on the other hand will polymerize as linear chains that are dominated by van der Waals type inter-chain bonding and therefore exhibit a smaller elastic modulus and larger phase angle (ψ). The rapid decrease in phase angle with increasing DVB content seen in Figure 4.11b is consistent with DVB cross-linking of the linear polystyrene chains and a corresponding decrease in the loss-modulus of the resulting polymer.[168]

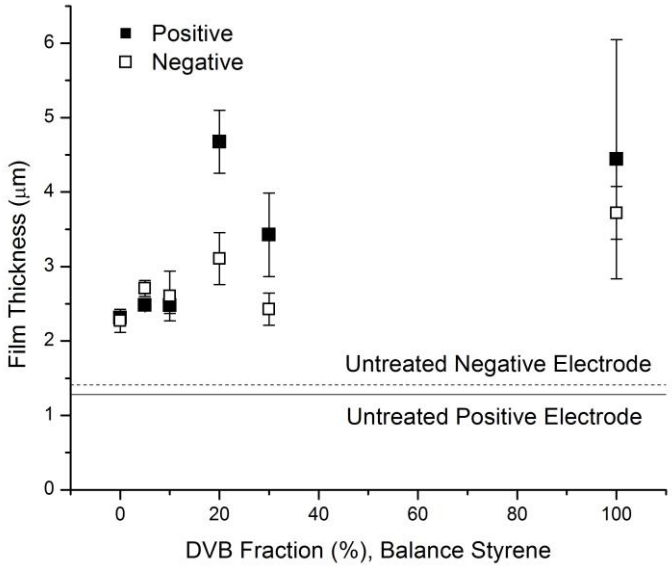

Figure 4.10: Thickness of the EPD film on the positive and negative electrodes after treatment solutions of varying fractions of DVB and styrene monomers, followed by polymerization.

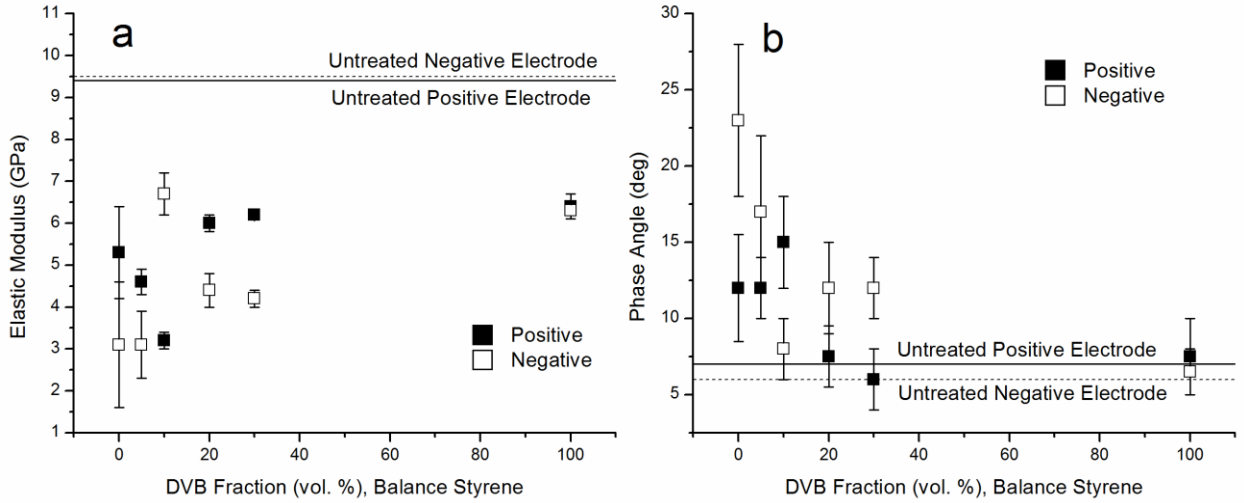

Figure 4.11: (a) Elastic modulus and (b) phase modulus of the EPD film on the positive and negative electrodes after treatment solutions of varying fractions of DVB and styrene monomers, followed by polymerization.

Figure 4.12 shows that the film modulus of EPD films treated with styrene decreases when the initiator concentration is increased for films formed on the positive and negative electrodes. This result again reiterates the fact that moduli are related to the molecular weight of the chains created by polymerization: the more initiator, the lower the molecular weight, the less chain entanglement, and the weaker the material.[171]

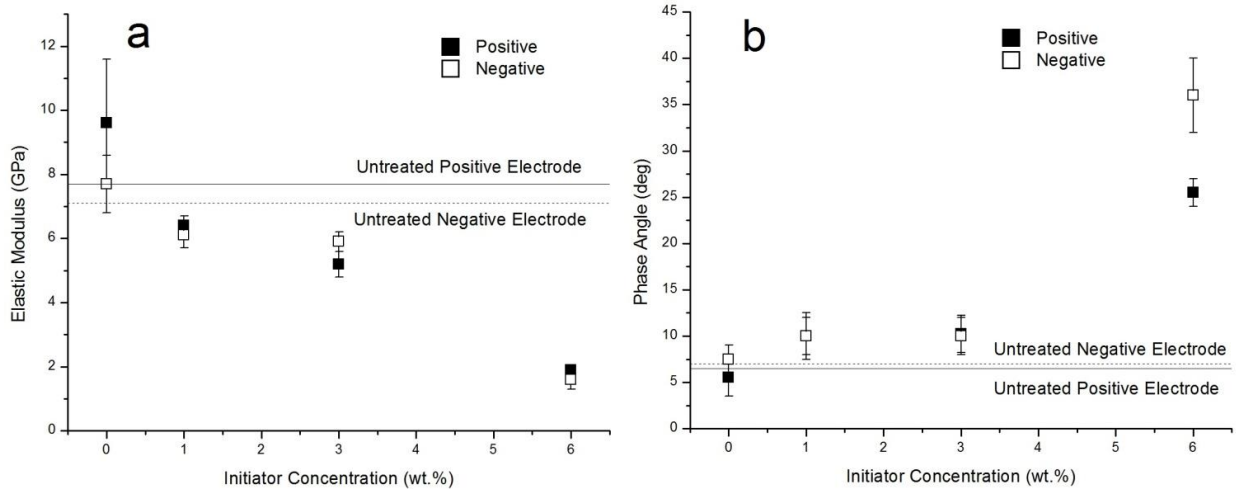

Figure 4.12: (a) Elastic modulus and (b) phase angle of the EPD films on the positive and negative electrodes after treatment by styrene monomer solution with different initiator concentrations, followed by polymerization.

All of the polymer-treated films have increased photoluminescence (PL) efficiency compared to the untreated films (Figure 4.13), with ~5× increases in PL in the DVB- and polystyrene-treated films and over 10× increases in PL the BDMA- and HDMA-treated films, and even more so in the DDMA-treated films. Each shows a small red shift relative to the untreated films.

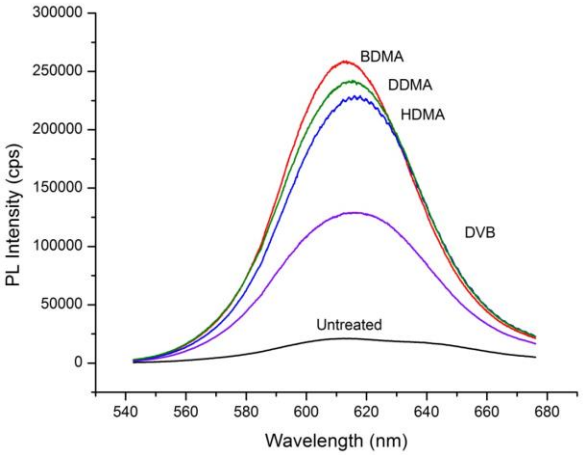

Figure 4.13: Photoluminescence of the EPD film after monomer treatment followed by polymerization (negative electrode).

4.6 Discussion

4.6.1 Overview of Film Properties

We assume that when the EPD NC film is contacted with the monomer, an equilibrium state is attained where the pure monomer is in equilibrium with a NC phase mixed with monomers. Under this assumption, the Flory-Huggins parameter (χ) of the NCs in the monomer is determined according to Equation 4.2 where we assume that a NC corresponds to a polymer with infinite molecular weight.[172] We further assume that $\phi = 1$ for the untreated EPD film and that the NC loading fraction for monomer-treated films (ϕ_m) is proportional to the treated film thickness (h_m) according to Equation 4.9, where h_0 is the untreated film thickness.

$$\phi_m = \frac{h_0}{h_m} \qquad \textbf{Equation 4.9}$$

The resulting χ parameters are reported in Table 4.1. The values of these parameters suggest that only partial miscibility is the norm when monomers are contacted with the NC film. This result arises from our underpinning assumption that there is an equilibrium between a pure monomer phase and one composed of a mixture of NC and monomer. Under these conditions $\chi > 0.5$, which is indeed what is found. The differences in χ cannot be rationalized on the basis of regular solution theory, $\chi \propto (\delta_{\mathrm{m}} - \delta_{\mathrm{NC}})^2$, since the solubility parameter, δ_{m}, is about the same for each monomer,[173, 174] and that of the NCs, δ_{NC}, is fixed. The results in Table 4.1 show that the NCs are barely miscible in DVB and are fairly miscible in the acrylates, and are more miscible the longer the alkane chain in the acrylate. Using single monomers, film swelling is relatively small when using DVB, and is even smaller with styrene-DVB mixtures (Figure 4.10). Some other factor, such as specific interaction between the acrylate group and the NC surface, or the interactions of the alkane spacers in the acrylate and the alkane part of the TOPO ligand, may play a role here, but these issues cannot be resolved with the experiments that have been performed to date. We defer these issues to future work.

Table 4.1: Flory-Huggins parameters (χ) for the EPD films after monomer diffusion and polymerization.

Treatment	Thickness (μm)	Estimated EPD Film Loading (vol. %), ϕ	χ
None	3.8	1	
DVB	8.8	0.43	0.72
BDMA	23.7	0.16	0.56
HDMA	62.7	0.06	0.52
DDMA	109.3	0.03	0.51

The inverse relationship of film elastic modulus and thickness occurs for several reasons: The elastic moduli of the polymers are smaller than those of the NCs and they are smallest for the polymers in which the NCs are most miscible—so these films are thicker and the NC loading factors are lower. The phase angle increases with film thickness because of the larger viscoelasticity of the polymers relative to the NCs, particularly for the monomers in which the NCs are most miscible.

A cross-linked polymer network, like that formed by DVB (a difunctional monomer) is expected to be more rigid than a similar polymer composed of individual chains (like that formed by styrene). Control films prepared of pure polymer confirm this, with the elastic moduli of poly-DVB and poly-acrylate films (Figure 4.9a) larger than that of polystyrene (~4.2 GPa), and with those of the corresponding EPD films being larger.

The cross-linking of polymers from one inter-NC interstitial region to the neighboring region may be small when there is little film swelling, but is clearly important when there is much swelling and the NCs are effectively dispersed in the polymer as in Figure 4.7.

In addition to suppressing fracture with relatively little film swelling, the chemical and mechanical properties of styrene-DVB copolymers can adjusted by controlling DVB content in the initial monomer blend, which leads to differences in cross-link density in the final polymer. Styrene-DVB copolymer are important in ion-exchange resins[165, 175] as well as proton exchange membranes (PEMs) where it has been shown that the incorporation of inorganic nanoparticles within the polystyrene-DVB PEM can impart enhanced mechanical, thermal, and mass-transport properties to the composite material.[176, 177]

The TEM of the ultramicrotomed sample and the observed increase in PL efficiency of polymer-treated films suggest that the NCs are homogenously distributed in an insulating film matrix. Such large increases in PL would not occur if a polymer-rich phase simply encapsulated an

underlying NC rich phase. The increase in PL efficiency suggests NC dispersion in the polymer and some passivation of the core NC cores; this could also explain the small PL red shifts seen in the polymer sample. The monomers are not conventionally used as ligands to cap and passivate the surfaces of CdSe NC cores. This increase in PL seems to be particularly strong for the acrylates (Figure 4.13), which suggests strong interactions with the states on the core surface. The PL red shift may suggest slight carrier delocalization at the core associated with this surface passivation.

4.6.2 Consideration of Polymerized EPD NC Film Modulus

The two-phase (CdSe NC core "filler" and polymer medium) Halpsin-Tsai model micromechanics model (Equations 3.13 - 3.15) was used with E_{CdSe} = 17 GPa (for r = 1.75 nm)[178], and ν_{CdSe} = 0.18. The elastic modulus of each polymer was assumed equal to those values measured in Figure 4.9. The bulk modulus (K) and shear modulus (G) of the polymer and CdSe NC phases were calculated using standard solid mechanics relationships (Equation 4.10 and Equation 4.11).[179]

$$K = \frac{E}{3(1-2\nu)} \qquad \textbf{Equation 4.10}$$

$$G = \frac{E}{2(1+\nu)} \qquad \textbf{Equation 4.11}$$

Using ligand shell thickness calculations introduced in Chapter 3 (Equation 3.2) we estimated the CdSe NC core volume fraction in the untreated film. Assuming a NC core diameter of 3.5 nm we predict the CdSe volume fraction in the as-deposited film (ϕ_{AD}) to be 0.69, 0.52, and 0.42 for 10 %, 20 %, and 30 % ligand coverage respectively. The lower end of this spectrum (10 – 20 % ligand coverage, ϕ_{AD} = 0.69 – 0.42) is most realistic in light of the extensive washing CdSe NCs are exposed to prior to EPD.

Under these assumptions it is found that different values of ν_{poly} lead to the best agreement between the measured values of polymer-treated EPD NC film modulus and the values predicted by the Halpsin-Tsai model (Table 4.2). It is apparent that for all polymer-treated EPD NC films there is a decrease in the best-fit value of ν_{poly} as the assumed value of initial ligand coverage increases. This is consistent with a film that loses some degree of elastomeric performance as a result of decreased cross-link density and increased fraction of van der Waals interaction (expected for alky-type TOPO ligands). Table 4.2 also shows that for DVB and DDMA the best-fit values of ν range from 0.22 – 0.36, while the best-fit values of ν_{poly} range from 0 – 0.8; suggesting that DVB- and DDMA-treated films have the lowest free-volume fraction and exhibit the highest degree of elastomeric performance.[161, 163] In the case of the DDMA-treated film, this is consistent with the high level of elastic recovery observed during nanoindentation (Figure 4.8).

Table 4.2: Poisson's Ratio (ν) that leads to best fit of by Halpsin-Tsai model to measured EPD NC/polymer film elastic modulus.

	10 % Ligand Coverage (ϕ_{AD} = 0.69)	20 % Ligand Coverage (ϕ_{AD} = 0.69)	30 % Ligand Coverage (ϕ_{AD} = 0.69)
DVB	0.36	0.28	0.22
BDMA	0.05	0.01	0
HDMA	0.08	0.06	0.05
DDMA	0.36	0.35	0.34

An intermediate value for the initial ligand coverage was assumed (20 %, ϕ_{AD} = 0.52) and a single value of $\nu_{Polymer}$ = 0.18 was found to provide the best over-all fit of the Halpsin-Tsai model to the measured elastic modulus data (Figure 4.9), where best fit is defined as the minimum value of $\sum_i \left| E_{Halpsin-Tsai} - E_{Measured} \right|$. Figure 4.14 shows that the Halpsin-Tsai model tends to over-

estimate the elastic modulus for DVB and DDMA while underestimating the elastic modulus of BDMA and HDMA.

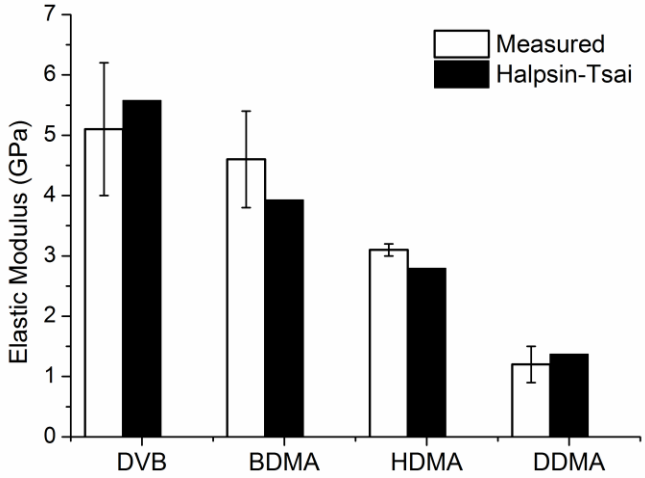

Figure 4.14: Comparison of measured film modulus with modulus predicted by Halpsin-Tsai model (ν_{poly} = 0.18).

4.6.3 Consideration of Stress and Strain

During monomer-treatment of the as-deposited EPD NC film, the monomers fill the voids between NCs and form a homogenous NC/monomer solution. We observe that for small monomers such as DVB and BDMA there is a relatively modest increase in the polymerized film thickness (< 5 x) compared to the untreated film, while the larger monomers such as HDMA and DDMA lead to a substantial increase in film thickness (> 10 x) relative to the untreated film. The work presented in Chapter 3 shows that relief of in-plane strain (i.e. $d_{dry,eq} \approx d_{wet}$ where d is the NC core separation) can lead to an ~38% increase in EPD film thickness. This suggests that the increased film thickness resulting from monomer treatment and polymerization is not simply preservation of the as-deposited NC spacing, but is the result of partial dissolution of the as-deposited film into the monomer phase. Because the final polymerized product is non-volatile, monomer treatment and polymerization avoids strain that would otherwise develop in the EPD NC films as a result of solvent evaporation and adherence of the film on the substrate.

There is however film strain arising from UV polymerization of the monomer-NC film, particularly in the case of cross-linked polymers.[180] The final in-plane tensile strain of these adhering films is determined by the difference in monomer and polymer densities. For pure DVB, the volume contraction is ~10% after polymerization, so the in-plane tensile strain after the isotropic contraction is ~0.03. For BDMA, the corresponding values are 3% and 0.01; even smaller values are expected for HDMA and DDMA because contraction scales inversely with density of cross-link points. In each case, the in-plane strain is much smaller than that for the untreated films and below the threshold for film fracture.

4.6.4 Consideration of Fracture

Using the Griffith's criterion for critical film thickness for fracture[181], polymer treatment of EPD NC films may prevent fracture by one or more potential mechanisms:

(1) Decrease of strain: The volume of the film originally occupied by deposition solvent is now occupied by polymer, so film contraction and corresponding tensile stresses are reduced. When the NCs are miscible in the monomers, strains and stresses should vanish, i.e. until polymerization. This mechanism is likely very significant in suppressing fracture.

(2) Increased film toughness: It has been well documented that the incorporation of nanoparticles in a polymer yields a composite material with toughness greater than that of the constituent polymeric phase.[182, 183] This could be part of the reason for the suppression of fracture in the treated EPD NC films.

(3) Increased plasticity: The infusion of monomers could be expected to increase film plasticity, so that NCs could reorganize and the film could relax prior to polymerization. Since the evaporation of monomers prior to polymerization noted in some cases led to film cracking, monomer infiltration apparently did not lessen strain film in these cases, and so this mechanism is

likely not important. There could be some local relaxation, but it does not occur on a large scale. For an adhering film, a decrease in film thickness would be expected after NC relaxation over large distances, but this is not seen.

(4) Film overcoating: The EPD film could be overcoated by a polymer film that bears a compressive stress to lessen film contraction. The TEM in Figure 4.7 showing NC dispersion and the polymer increase in PL (Figure 4.13) suggest there is no mechanically robust overcoat, and so this is not a primary source of crack suppression. Furthermore, such large increases in PL would not occur if a polymer-rich phase simply encapsulated an underlying NC rich phase.

4.7 Conclusions

When large strains and fracture arise after drying of EPD films formed from NC with incomplete ligands shells on the core, the mechanical state of the film can be substantially improved through the infusion of small monomers in the still wet film, followed by polymerization. Specifically, it was seen here that treating CdSe NC EPD films with several monomers followed by UV-initiated polymerization suppressed cracking. The packing density of NCs remains high for several of the polymers, in particular those formed using DVB and styrene-DVB mixtures, as it is for the untreated EPD NC films. However, NC packing density is reduced if the monomer treatment swells the as-deposited NC film, such as after treatment with HDMA and DDMA. In these films the NCs are believed to dissolve into the monomer, and upon subsequent UV polymerization form a more dilute NC-organic composite. Although polymerization of a monomer is known to decrease the material's volume and likely leads to some tensile strain in the polymerized EPD NC film, the level of strain is apparently below the fracture threshold of the composite NC-organic material. Monomer treatment and subsequent polymerization appears to passivate the CdSe NC core surfaces and increases the PL efficiency of the final film. This suggests intimate contact between

the polymer phase and the NC core surface and indicates there may be an opportunity to increase the conductivity of polymer-treated EPD NC films by choice of a conductive ligand. A mechanically robust, electrically conductive, NC film formed through EPD could be useful for applications such as solar cells[156] and field-effect transistors.[184]

This work discussed in this chapter has been published:

T. J. Kramer, S. K. Kumar, M. L. Steigerwald, and I. P. Herman, *J. Phys. Chem. B,* **2012**, 117, 1544

5 Poly(3-hexylthiophene) Nanowire Films for Photovoltaic Devices

5.1 Introduction to Hybrid organic/inorganic NC Composites for Photovoltaic Devices

In the previous chapters we have focused on NC composite materials created by back-filling an inorganic NC film with an organic material that lends both mechanical stability and chemical passivation; leading to nanocomposite films with improved mechanical properties and enhanced optical performance. The ability to precisely deposit NCs using electrophoretic deposition (EPD) and thus control the resulting nanocomposite material with a micron scale precision reflects the goal of this thesis: to explore techniques for the control of interfaces in hybrid NC-organic composites. In this chapter we will explore a complementary technique in which an organic material is back-filled with inorganic NCs, in this case reaching a nanometer level of precision in locating the organic-inorganic interface. Specifically, we will explore a technique developed as part of this thesis whereby a sacrificial polymer is used to template poly(3-hexylthiophene) [P3HT] into a film consisting of a dense array of crystalline nanowires. This structure, when backfilled with a complementary electron accepting phase (such as NCs), can be used to yield a hybrid nanocomposite with potential application as the active material in a photovoltaic (PV) device.

5.2 Photovoltaic Nanostructures

5.2.1 Organic Bulk Heterojunctions for Photovoltaic Applications

Organic bulk heterojunctions (BHJs) are a promising platform for solar energy conversion due to the low cost of the precursor materials, their high active volume fractions (i.e. film volumes within an exciton diffusion length of a donor-acceptor interface), and their potential for high-

throughput production (i.e. roll-to-roll processing). The highest reported external quantum efficiencies (EQE) for such devices are over 8%.[90, 185, 186] Attaining higher efficiencies will likely require new materials systems that absorb in the infrared (IR) portion of the solar spectrum. In particular, the use of inorganic IR sensitizing materials in conjunction with organic materials holds promise for enhancing the efficiency of low-cost photovoltaic (PV) devices.[94, 187, 188] The current paradigm of depositing both the donor and acceptor phases of a BHJ simultaneously from a common solvent limits the use of many such IR sensitizing materials. Such one-step methods of BHJ fabrication require each phase to meet a demanding set of electronic and miscibility criteria to attain good electrical characteristics as well as optimal nanoscale morphology.

5.2.2 Nanocrystal-sensitized Photovoltaics

Inorganic nanocrystals (NCs) have desirable optical and electronic properties and could serve as an optical sensitizing agent within a BHJ;[96, 189, 190] however, limited NC solubility in complementary organic materials can prevent the formation of an efficient BHJ morphology. Conventional techniques,[191] such as spin casting NCs simultaneously with organic semiconducting materials, typically lead to NC aggregation, which limits device performance.[192, 193]

One strategy to avoid the aggregation of NCs (or any other complementary phase) when utilized in a composite material is to structure one phase of the composite first and then backfill the second phase.[194] For PV devices it is particularly desirable for the donor phase (where the majority of optical absorption occurs) to have a nanowire morphology which results in a high volume fraction of material within an exciton diffusion length[195] of a donor-acceptor interface (i.e. active volume).

5.2.3 Low-dimensional Organic Nanostructures for Photovoltaics

Considerable research has been dedicated to the development of low-dimensional structures composed of organic semiconductors,[196-198] with organic PV performance being found to depend on both phase morphology and crystallinity.[199-202] Poly-(3)hexylthiophene (P3HT) in particular has been found to spontaneously form nanowires in a variety of donor/acceptor blends. Annealing blends of P3HT and [6,6]-phenyl-C_{61}-butyric acid methyl ester (PCBM) creates a network of highly crystalline P3HT nanowires within a PCBM rich phase,[199, 200, 203-205] resulting in enhanced PV device performance. Distinguishing the beneficial influences of P3HT crystallization and P3HT nanowire morphology on PV device performance is difficult. Increased P3HT crystallinity provides enhanced hole mobility, while the evolution of an interpenetrating donor/acceptor morphology facilitates exciton separation and charge carrier transport. Annealing of spin-cast P3HT/PCBM blends leads to P3HT nanowire crystallization, but PCBM diffusion within amorphous P3HT remains an active process even after crystallization of P3HT is complete. The continued improvement in PV device performance observed upon continued annealing, when P3HT crystallization has concluded, suggests that evolution of donor/acceptor morphology alone is important and can be utilized to improve the efficiency of PV devices.[203, 206, 207]

The ability to control P3HT crystallization and morphology independently of the acceptor phase is difficult using traditional one-step casting methods.[199, 200, 202, 208] When using non-fullerene acceptor materials (such as NCs or planar conjugated molecules)[96, 190, 209] the miscibility of donor and acceptor phases is expected to change dramatically compared to fullerene-based systems,[210] and may not lead to favorable blend morphologies. It will be advantageous to develop techniques in which the donor-acceptor morphology is decoupled from the choice of acceptor material. Also, although solution-phase methods for generating P3HT nanowires can yield efficient BHJ structures,

their reliance on relatively large volumes of dilute P3HT nanowire solutions is undesirable from a production standpoint. The need for careful filtration of unwanted byproducts further limits the utility of solution-phase nanowire production.

It would be advantageous to generate nanowire P3HT films directly on a substrate prior to application of the acceptor phase. Previous work has shown that it is possible to deposit a mat of P3HT nanowires on a variety of substrates utilizing rigid templates[107, 211-213] and electrospinning,[214, 215] as well as by growing P3HT nanowires in a marginal solvent and casting these fibers on a substrate.[216-218] Using such techniques it is possible to backfill a high active volume P3HT morphology with a complementary acceptor material, in some cases yielding photovoltaic devices with power conversion efficiencies (PCEs) of over 3%.[216, 217] More recently it has been shown that various organic nanowires (including P3HT) can be decorated with NCs while still in solution prior to casting on to a substrate.[114, 219-221]

Qiu and coworkers demonstrated that it is possible to generate P3HT nanowires on a substrate by annealing planar films of P3HT and poly(methylmethacrylate) (PMMA), followed by the removal of the PMMA using acetic acid.[222, 223] This technique employs a low initial P3HT concentration (< 5 wt.%) and also relies on an oxidizing selective solvent (acetic acid) that is expected to degrade the performance of most organic semiconducting polymers.

We report a versatile two-step method for generating P3HT nanowires directly on a substrate, producing an improved nanoscale BHJ morphology. By using a non-oxidizing selective solvent to remove PS from a P3HT/PS blend we generate a dense mat of highly crystalline P3HT nanowires that are 20-40 nm in diameter and hundreds of nm long. Others have used blends of P3HT and polystyrene (PS) to create similar structures,[208] but to our knowledge it has not been demonstrated that the PS phase can be removed from a P3HT blend with a selective orthogonal

solvent to expose nanowires of P3HT. Our nanowire mat can subsequently be backfilled with various complementary materials, such as PCBM or cadmium selenide (CdSe) NCs using an orthogonal solvent. This process enables scalable, on-chip fabrication of P3HT nanowire networks suitable for fabrication of BHJ devices composed of complementary materials that would not otherwise form a BHJ morphology using traditional one-step casting methods when the acceptors do not have suitable solubility/miscibility characteristics to promote nanowire growth while avoiding acceptor phase aggregation (as with NCs).

5.3 Results

After removing PS (10.4 kg/mol) from the initial P3HT/PS blend, the films contain an abundance of P3HT nanowires that are 20-40 nm in diameter and hundreds of nm long. The SEM image in Figure 5.1 reveals the morphology that results from a typical blend of P3HT and PS initially containing 50 wt. % P3HT after removal of the PS phase. The influence of the P3HT:PS ratio on the P3HT nanowire network morphology was explored by fixing the P3HT concentration at 15 mg/mL and varying the concentration of PS (MW of 10.4 kg/mol) from 15 to 60 mg/mL.

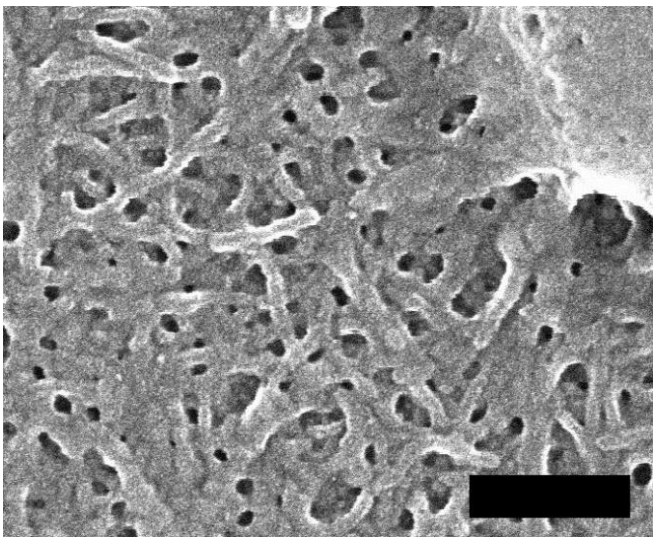

Figure 5.1: SEM image of P3HT nanowires generated from a blended film initially containing 33 wt. % P3HT and 77 wt. % 6.4k MW polystyrene (PS). The scale bar is 200 nm wide.

As seen in Figure 5.2a and Figure 5.2b (and also in lower magnification in Figure 5.4a and Figure 5.4b), an initial P3HT content of 40 wt. % or less (10.4 kg/mol PS) results in a mat of P3HT nanowires covering the majority of the substrate with raised micron-scale circular mesas of planar P3HT. This structure is inverted for blends of P3HT and PS initially containing 50 wt. % or more P3HT; when P3HT is the majority constituent (Figure 5.2c and Figure 5.2d, and also in Figure 5.4c and Figure 5.4d) there are small pockets of P3HT nanowires surrounded by a planar P3HT film that covers large portions of the substrate.

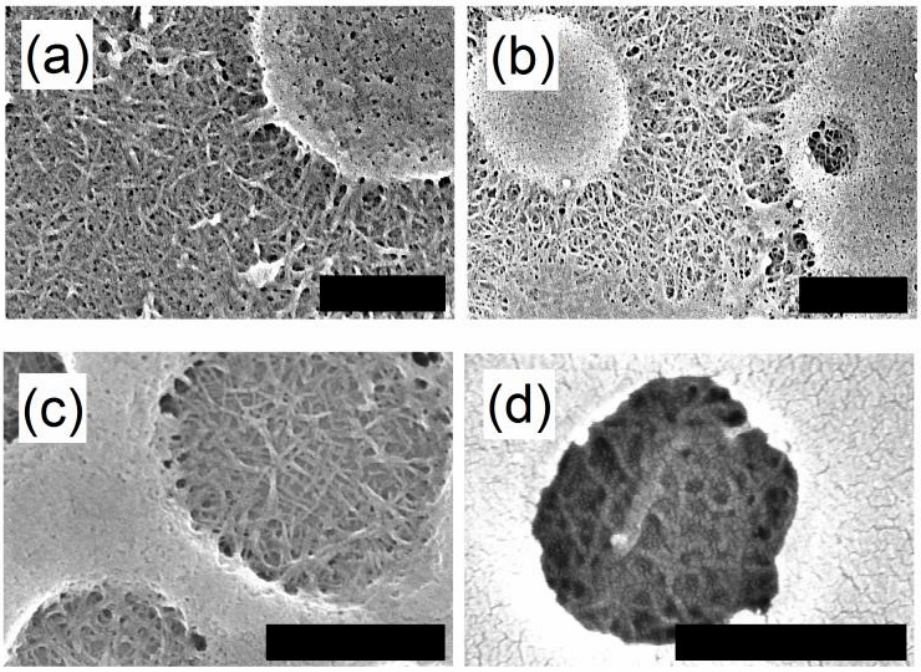

Figure 5.2: SEM images of P3HT nanowires generated from blended films initially containing (a) 30 wt. % P3HT, (b) 40 wt. % P3HT, (c) 50 wt. % P3HT, and (d) 75 wt. % P3HT (scale bar 500 nm). The remaining balance of all films is 10.4k MW polystyrene (PS). The scale bars are 1 μm wide.

AFM traces of blended P3HT-PS films before and after PS removal show that the thickness of the planar film regions approximately equals the thickness of the original blended film (Figure 5.3), suggesting the planar regions in these films are the original blended film surface. It is also apparent from Figure 5.3 that P3HT nanowire mats generated from blended films initially containing <40 wt. % P3HT are extremely thin (<40 nm) and may contain only one or two

monolayers of P3HT nanowires, while those containing ≥50 wt. % P3HT are relatively thick (~60 nm). As seen in Figure 5.3a, the thickness of the nanowire mat as well as the height of the planar mesa regions generated from low P3HT fraction blends are reduced compared to film cast from blends containing 50 wt. % P3HT and greater. We attribute the decrease in film thickness to loss of P3HT that had become fully surrounded by PS in the initial spin-casting step, and was then dislodged upon PS removal.

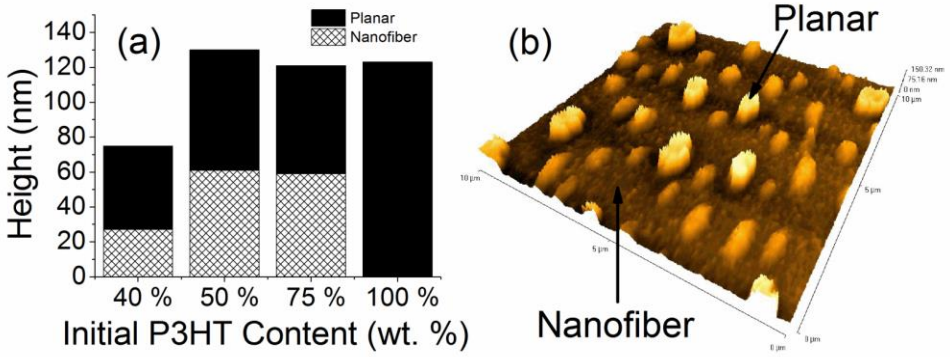

Figure 5.3: (a) AFM thickness data from P3HT nanowire films generated by removal of PS from P3HT/PS blended films (all films cast from solutions containing 30 mg/ml total solids). Thickness data are averaged over 100 μm². (b) AFM image from P3HT nanowire films generated by removal of PS from a P3HT/PS blend with 40 wt. % P3HT.

As the P3HT weight fraction is reduced the areal fraction of the chip covered by the nanowire mat steadily increases, as seen in Figure 5.4e. The SEM images of these films were analyzed by image processing (pixel counting), with nanowire pockets and planar P3HT mesas approximated as ellipsoids to determine the areal fraction of the film covered with P3HT nanowires. Figure 5.4e shows an approximately linear decrease in exposed P3HT nanowire coverage as the P3HT weight fraction in the initial polymer blend is increased. This suggests that films cast from solutions initially containing relatively low P3HT content (< 30 wt. %) exhibit the greatest areal fraction of P3HT nanowires upon PS removal.

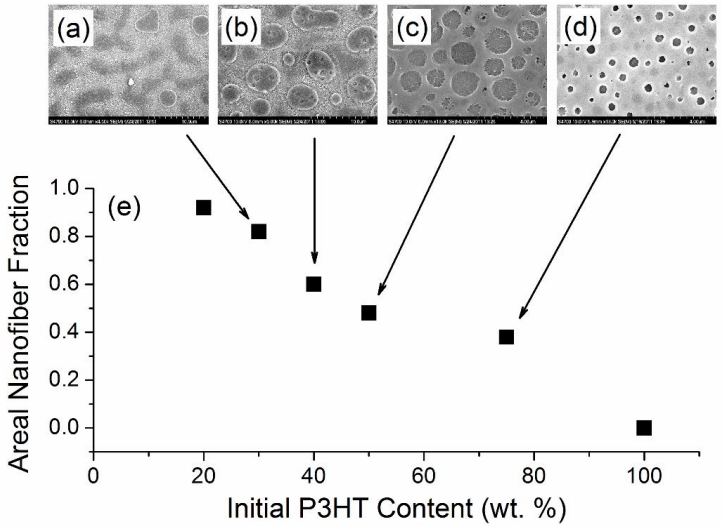

Figure 5.4: Areal fraction of P3HT films with nanowire morphology in (e), along with SEM images of P3HT nanowires generated from blended films initially containing (a) 30, (b) 40, (c) 50, and (d) 75 wt. % P3HT. The scale bars are 5 µm wide.

Surface contact angle measurements were performed to test this apparent monotonic correlation between initial P3HT fraction and nanowire coverage. The data seen in Table 5.1 reflects the average of ten separate measurements conducted using water droplets with a volume of 8 ml.

Table 5.1: Average surface contact angles made by water droplets in contact with P3HT films after removal of PS from blends containing different initial P3HT content.

Initial P3HT Content (wt. %)	Average Contact Angle (°)
20	101.2 ± 4.8
30	106.4 ± 1.8
40	109.4 ± 4.6
50	119.7 ± 2.2
60	117.5 ± 4.2
70	114.6 ± 3.0
80	111.8 ± 1.5
100	102.0 ± 2.7

We assume that the intrinsic interfacial energy of P3HT does not depend on P3HT morphology. On the macroscopic scale (such as the area contacted by a water droplet) we assume there is a surface roughness factor S that describes the larger interfacial surface area of a non-planar morphology and the correspondingly larger effective interfacial energy, as given by

$$\gamma^{NW} = S\gamma^{P} \qquad \textbf{Equation 5.1}$$

where γ is the effective interfacial energy and the superscripts P and NW denote the planar and nanowire morphologies respectively. Using Young's equation [$\gamma_{gl}\cos(\theta) = \gamma_{sg} - \gamma_{sl}$] to describe the contact angle θ at the circumference of a liquid droplet in contact with a solid substrate, Equation 5.1 becomes

$$S\left[\gamma_{sg}^{P} - \gamma_{sl}^{P}\right] - \gamma_{gl}\cos(\theta^{NW}) = \gamma_{sg}^{P} - \gamma_{sl}^{P} - \gamma_{gl}\cos(\theta^{P}) \qquad \textbf{Equation 5.2}$$

where γ_{sg}, γ_{sl}, and γ_{gl} denote the solid-gas, solid-liquid, and gas-liquid interfacial energy respectively. Substituting Young's relationship into Equation 5.2 leads to

$$S = 1 + \frac{\gamma_{gl}[\cos(\theta^{NW}) - \cos(\theta^{P})]}{\gamma_{sg}^{P}\cos(\theta^{P})} \qquad \textbf{Equation 5.3}$$

which upon making the assumption $\gamma_{gl} \approx \gamma_{sg}$ reduces to the Wenzel relationship[224] for liquid droplets in contact with a rough surface

$$\cos(\theta^{NW}) = S\cos(\theta^{P}) \qquad \textbf{Equation 5.4}$$

Using Equation 5.4 and the measured values of θ^{NW} (Table 5.1) we arrive at the estimates of the surface roughness S shown in Figure 5.5. These data suggest that the nanowire morphology produces a maximum effective surface area that is approximately twice that of the planar (100 wt. % P3HT) film.

Cassie and others have explored the influence of incomplete wetting by a liquid droplet in contact with a hydrophobic porous substrate due to trapped air.[225, 226] Assuming an idealized substrate described by a repeating array of parallel cylinders, it can be shown that

$$\cos(\theta^{NW}) = f[\cos(\theta^{P}) + 1] - 1 \qquad \textbf{Equation 5.5}$$

where f is the fraction of the liquid-substrate interface in contact with the solid material and 1-f (the areal porosity) is the fraction of the droplet in contact with trapped air. Applying Equation 5.5 to the surface contact data reveals that P3HT nanowire films (Figure 5.5) have up to 40% areal porosity (i.e., $f \sim 0.6$). The observed differences between results in Figure 5.4e and Figure 5.5 (for S) are attributed to the presence of exposed SiO_2 substrate for films cast from low initial P3HT weight fraction blends(< 40 wt. %). As seen in Figure 5.3 nanowire films generated from blends with low initial P3HT content may be only ~ 20 nm thick and are susceptible to pinholes which would expose the hydrophilic SiO_2 substrate and decrease the average surface energy of the water-substrate interface; leading to reduced contact angle and an apparent decrease in film surface area.

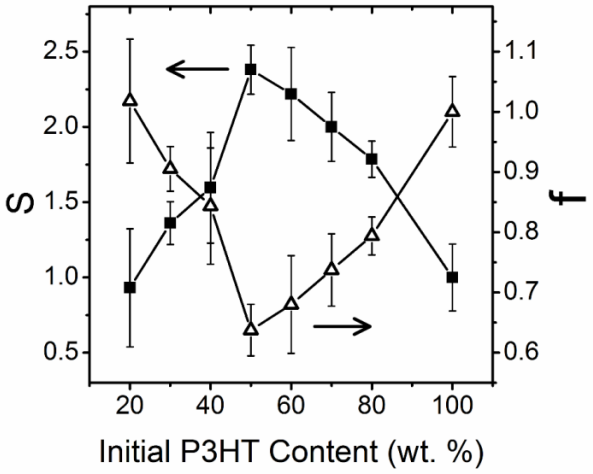

Figure 5.5: Effective surface roughness (*S*) and wetting fraction (*f*) as calculated from surface-contact angle measurements presented in Table 5.1.

UV-vis absorption spectra taken before and after PS removal of blended films (cast on ITO-coated glass substrates) show that for blended films initially containing 40 wt. % P3HT or less, there is a decrease in P3HT absorption at 560 nm of over 10%, indicating a loss of P3HT when the PS is removed. This is consistent with Figure 5.3 and the hypothesis that the low effective surface area reported in Figure 5.5 is the result of exposed substrate.

In contrast, the UV-vis absorption spectra shown in Figure 5.6 reveal that very little P3HT is lost in the PS removal process when the initial P3HT blend contains 50 wt. % P3HT or greater (< 3% decrease in film absorption at 560 nm upon PS removal). In Figure 5.6 it is also apparent that the incorporation of PS into the film has very little effect on the absorption profile of the blended film. However, upon removal of the PS phase from the blended film the P3HT nanowire mat exhibits a reduced absorption shoulder at ~525 nm while the absorption peak at ~610 nm is enhanced. The increased relative absorption at 610 nm may be the result of an increase in the number of delocalized inter-chain excitonic states[65].

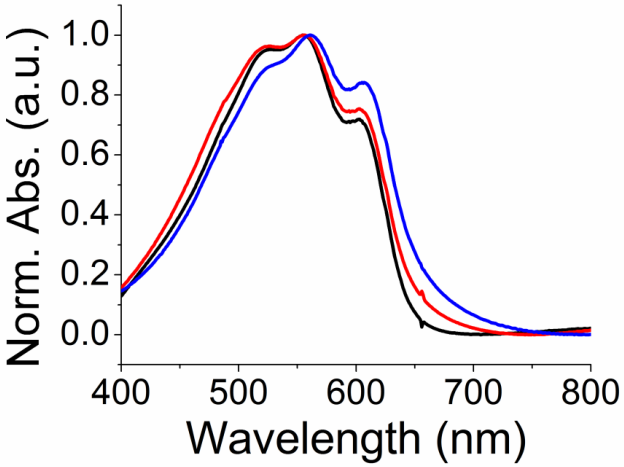

Figure 5.6: UV-visible absorption spectrum of films prepared from as-received P3HT (black), 50 wt. % P3HT- 50 wt. % PS blend (red), and P3HT nanowire mat resulting from removing PS from 50 wt. % P3HT-50 wt. % PS blend.

The influence of the PS molecular weight on P3HT nanowire morphology was investigated by varying the PS MW from 6.4 kg/mol to 96k kg/mol, while keeping the P3HT:PS ratio constant (33 wt. % P3HT). As seen in Figure 5.7 the final P3HT morphology is relatively insensitive to PS MW and is characterized by nanowires covering approximately ~80-90% of the substrate surface. However, for PS MW of 19k g/mol or higher, two 30 min immersions in fresh PS selective solvent (1:2 THF/EtOH) were needed to fully remove the PS phase, resulting in a P3HT nanowire morphology equivalent to those discussed above.

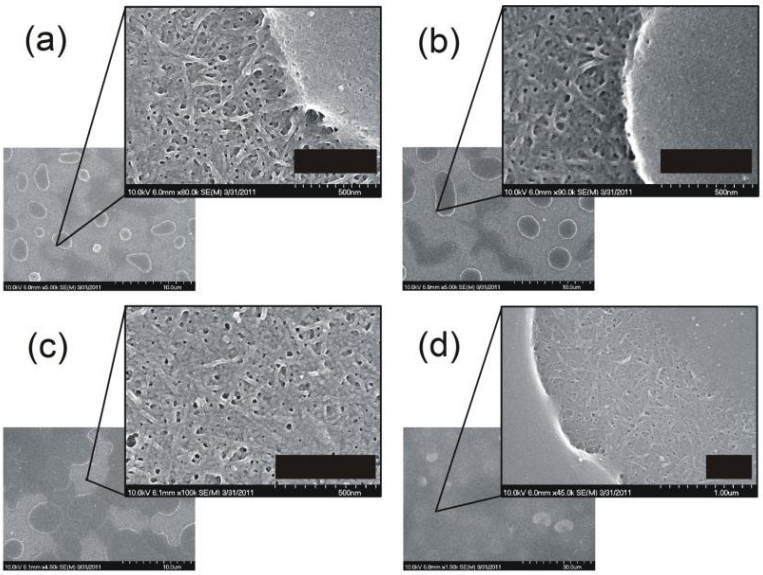

Figure 5.7: P3HT nanowire films produced by selective removal of PS from initial P3HT/PS blends containing PS with a MW of (a) 6.4k g/mol, (b) 10k g/mol, (c) 17.3k g/mol, and (d) 96k g/mol. The initial P3HT/PS blend contained 33 wt. % P3HT. Scale bars are 500 nm wide.

The WAXS data presented in Figure 5.8c demonstrate that P3HT nanowire films produced by selective removal of PS from a P3HT/PS blend exhibit a degree of crystallinity similar to that of the pristine P3HT film (Figure 5.8a). Diffraction peaks from the first, second, and third order (h00) reflections appear along the q_z axis at values of 0.38 Å^{-1}, 0.8 Å^{-1}, and 1.2 Å^{-1}, respectively, in all samples. This indicates that the lamellar side-chain stacking between adjacent thiophene molecules is normal to the substrate[59, 227, 228] and that the π-conjugated plane of the thiophene repeat unit has an edge-on orientation to the substrate. A weak signal from the (010) reflection at a q_{xy} ~1.6 Å^{-1} suggests the π- stacking of thiophene molecules is partially crystalline. The diffuse reflection signal at q~1.8 Å^{-1} is attributed to scattering from the underlying PEDOT and is seen in control samples of pure PS as well as bare PEDOT on ITO (Figure 5.9). Overall, the crystallinity of the pristine P3HT film and the P3HT/PS film after PS removal are very good, and that of the P3HT/PS blend film is slightly better.

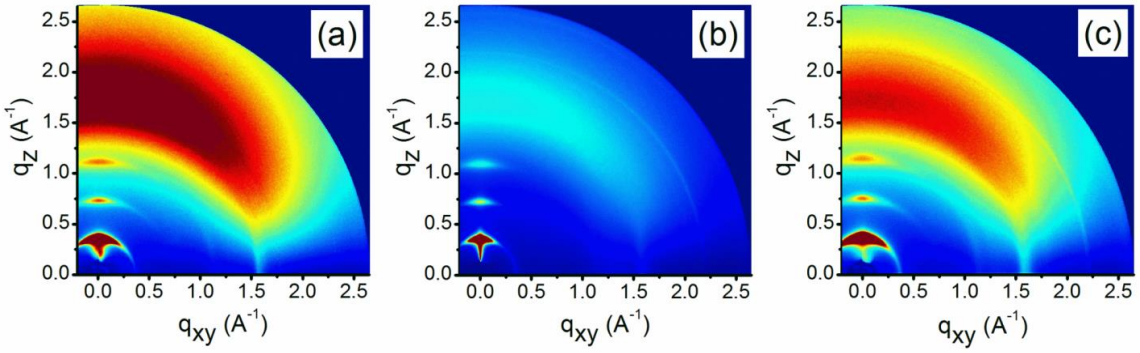

Figure 5.8: WAXS data from (a) pristine planar P3HT, (b) a blended P3HT/PS film containing 50 wt. % P3HT, and (c) a P3HT nanowire film generated by removal of PS from an initial P3HT/PS film containing 50 wt. % P3HT. Data collected at the Stanford Synchrotron Radiation Light Source.

A line trace of q_z (Figure 5.9a) reveals a slight shift of the (100) peak to lower q_z values for the P3HT/PS blend film relative to pristine P3HT and suggests a very slight (~1%) expansion of the *d*-spacing along the a-axis of the P3HT crystal (h00 direction) when the PS phase is present. When the PS phase is removed, the position of the (100) reflection shifts to higher q_z values, consistent with a ~3% decrease in lamellar stacking distance relative to pristine P3HT. The fact that this expansion/contraction is small and not accompanied by significant broadening of the (100) peak suggests that the P3HT crystal structure is only slightly perturbed by the presence of the PS phase or by its subsequent removal. It is therefore likely that only a very small fraction of the PS is intercalated into the P3HT crystallites that compose the resulting nanowires. A similar shift is not found in the (010) reflection found at a q_{xy} value of ~1.6 Å (Figure 5.9b) indicating that PS has less effect on the π-π stacking of adjacent molecules compared to the out-of-plane lamellar side-chain stacking.

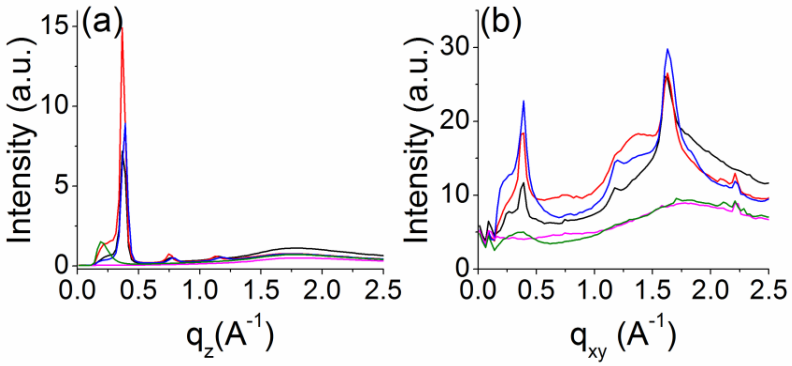

Figure 5.9: Intensity traces of the 2D WAXS pattern from a bare PEDOT-coated ITO substrate (green), a PS control film (magenta), a P3HT control film (black), a P3HT-PS blend (50 wt. % P3HT) (red), and a P3HT nanowire film (blue) integrated within (a) a 20° arc starting from the q_z direction toward the q_{xy} direction and (b) a 10° arc starting from the q_{xy} direction toward the q_z direction.

SEM images of P3HT nanowire films treated with solutions of 1:2 DCB/DPE (Figure 5.10) show that the nanowire morphology is not damaged by application of the acceptor phase during PV device fabrication. As seen in Figure 5.10, the persistence of the P3HT nanowires suggests that the DCB/DPE mixture used to apply both PCBM and CdSe NCs to P3HT nanowire films for PV device fabrication does not damage the nanowire morphology.

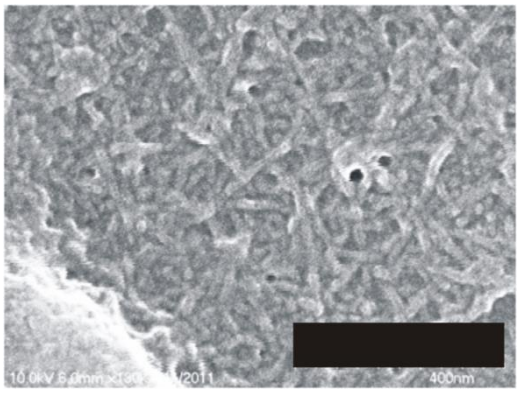

Figure 5.10: P3HT nanowire film generated by removal of PS from an initial P3HT/PS blend containing 30 wt. % P3HT after spin casting a solution of 1:2 DCB/DPE at 800 rpm for 60 s followed by 2000 rpm for 5 sec. The scale bar is 400 nm wide.

The WAXS data presented in Figure 5.11 are consistent with Figure 5.10 and demonstrate that the crystallinity of P3HT is not substantially affected by treatment with PCBM in DCB/DPE. Of particular significance is the fact that the intensity of the (100) reflection at $q_z = 0.38$ Å^{-1} does not

change substantially after treatment with DCB/DPE, indicating the carrier solvent for PCBM and CdSe is orthogonal to the P3HT nanowire film.

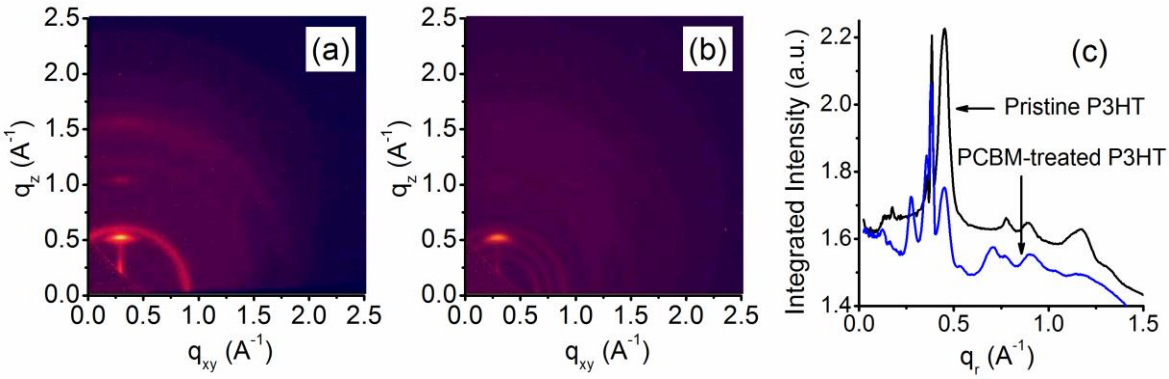

Figure 5.11: WAXS data from (a) pristine planar P3HT films and (b) planar-bilayer-prepared P3HT/PCBM films, along with (c) line traces of intensity for these data. Data collected at the National Synchrotron Light Source at Brookhaven National Laboratory.

The *J-V* curves of four photovoltaic devices fabricated by backfilling P3HT nanowire network films with organic and inorganic acceptor materials are shown in Figure 5.12. As seen in Figure 5.12a, a planar-prepared P3HT/PCBM device (50 wt. % P3HT) has a short circuit current density (J_{sc}) of 0.8 mA/cm^2, an open circuit voltage (V_{oc}) of ~0.43 V, and a fill factor (FF) of 0.37, yielding a power conversion efficiency (PCE) of 0.13%. For a nanowire P3HT/PCBM device fabricated from an initial P3HT/PS blend containing 50 wt. % P3HT, the J_{sc} increases to 7.75 mA/cm^2, with V_{oc} = 0.62 V and FF = 0.25, yielding a PCE of 1.22%. This represents an increase in efficiency of 840% compared to similarly processed planar-prepared devices.

As a demonstration of the versatility of this fabrication method we also constructed PV devices consisting of P3HT nanowires backfilled with CdSe NCs (Figure 5.12b). This type of device is unique in its ability to combine both organic and inorganic materials in a PV device with well-defined BHJ morphology. The planar-prepared P3HT/CdSe NC device has J_{sc} = 0.32 mA/cm^2, V_{oc} = 0.80 V, and FF = 0.42, yielding a PCE of 0.11%. When a nanowire device (33 wt. % P3HT) is

similarly backfilled with CdSe NCs, J_{sc} = 3.0 mA/cm^2, V_{oc} = 0.53 V, and FF = 0.26, yielding a PCE of 0.41%, which is a 270% increase over the equivalent planar-prepared device.

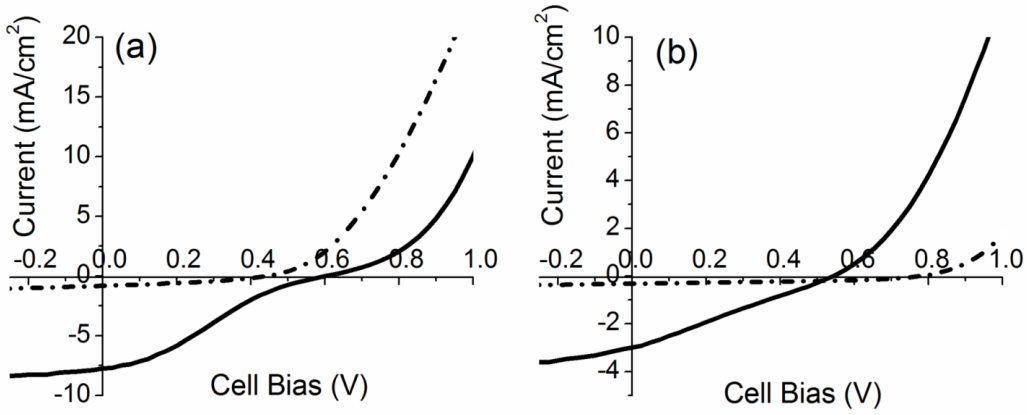

Figure 5.12: (a) J-V curves of all-organic PV devices fabricated by backfilling with PCBM a planar P3HT film (dashed line) (cast from a solution of 15 mg/mL P3HT), and a nanowire P3HT film (solid line) (P3HT/PS solution containing 15 mg/mL (50 wt. %) P3HT). (b) J-V curves of hybrid PV devices fabricated by backfilling with CdSe NCs a planar P3HT film (dashed line) (15 mg/mL P3HT), and a nanowire P3HT film (solid line) (P3HT/PS solution containing 15 mg/mL (33 wt. %) P3HT). The films represented by dashed lines are called planar-bilayer-prepared in the text.

The influence of P3HT content in the initial P3HT/PS blend on eventual PV device performance was studied and the results presented in Figure 5.13. Following procedures described above, a series of all-organic P3HT/PCBM devices were fabricated by backfilling of P3HT nanowire films with PCBM dissolved in a solution of 1:2 DCB/DPE. P3HT nanowire films were prepared from P3HT/PS blends containing 10 wt. %, 20 wt. %, 30 wt. %, 40 wt. %, 50 wt. %, and 100 wt. % P3HT (all films cast from solutions containing 15 mg/ml P3HT). Results for the 50 wt. % and 100 wt. % (planar) devices are Figure 5.12. We find that devices fabricated from P3HT/PS blends containing less than 20 wt. % P3HT do not exhibit PV performance, likely as a result of cathode-anode short circuits. PV performance for devices fabricated using 20, 30, 40, and 50 wt. % P3HT is presented in Figure 5.13.

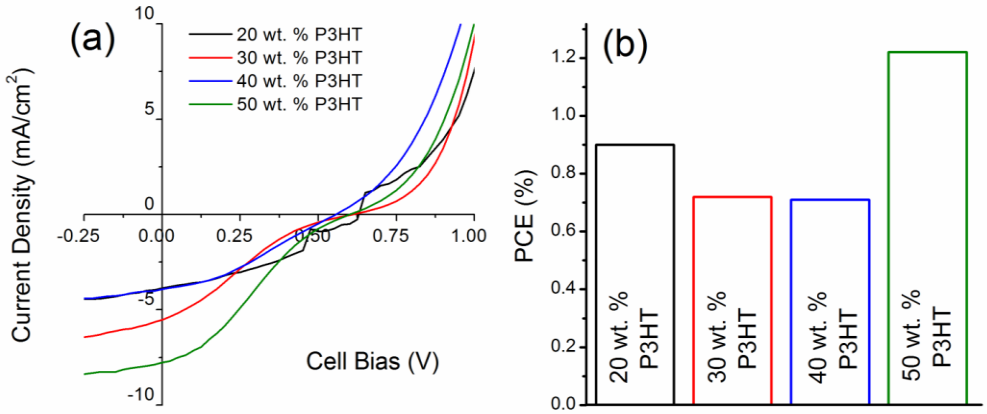

Figure 5.13: (a) J-V curves of four PV devices fabricated by backfilling of P3HT nanowire mats (20-50 wt. % initial P3HT content) with PCBM. (b) PCE of same PV devices depicted in (a).

In all cases the PV performance of nanowire P3HT devices greatly exceeds the PV performance of an equivalent planar device (PCE_{planar} = 0.13 %). Although PV performance does not correlate precisely with the apparent nanowire coverage (Figure 5.4), it is significant that the device exhibiting the greatest PCE corresponds to a P3HT nanowire film with the greatest apparent surface roughness (Figure 5.5). The relatively similar values of PCE for devices fabricated from P3HT/PS blends containing 20, 30, and 40 wt. % P3HT may mean these films have similar sub-surface morphology that cannot be effectively characterized using SEM and surface contact-angle measurement techniques.

5.4 Discussion

Spontaneous demixing of P3HT and PS generates a dense array of crystalline P3HT nanowires embedded in a PS matrix. The PS matrix is subsequently removed using a selective solvent, exposing a network of P3HT nanowires that has substantially greater surface area and active volume than a planar P3HT film. The WAXS measurements reveal that these P3HT nanowires are highly crystalline and that PS is absent from the interior of the P3HT nanowires.

Our results suggest that the formation of P3HT nanowires is driven by the crystallization of the P3HT phase and the corresponding exclusion of the PS phase from the P3HT crystallites. The P3HT phase appears to preferentially adhere to the substrate and upon crystallization forces the PS phase to migrate toward the exposed film surface. This phenomenon is fortuitous given that many PV devices are fabricated utilizing ITO as both the substrate and anode (hole acceptor).

At low P3HT fractions this method produces many small P3HT crystals that are surrounded by a continuous matrix of PS. Upon PS removal from these films some of the P3HT is left unsupported, leading to a loss of P3HT to the selective solvent. There must be sufficient P3HT in the initial blend so that during film drying the P3HT domains form a continuous and interconnected network of nanowires. This type of network appears to occur only for P3HT fractions >40 wt.%. The molecular weight of the PS sacrificial phase appears to have relatively little effect on the final film morphology.

The observed transition from "pockets" of nanowires in a "sea" of planar material to a sea of nanowires with mesas of planar material is clearly influenced by P3HT content. When the P3HT loading is high (> 40%) we see that PS is excluded into approximately cylindrical regions resulting in pockets of P3HT nanowire. When P3HT loading is 40 wt. % or less we observe the formation of cylindrical regions of high P3HT concentration, which upon PS removal results in circular mesas of planar P3HT surrounded by a mat of P3HT nanowires.

The surface contact angle analysis in Figure 5.5 suggests the maximum film roughness of P3HT nanowire mats occurs with an initial P3HT content of ~50 wt. %, whereas the image processing technique (Figure 5.4e) suggests maximum nanowire coverage at lower P3HT loading. The UV-vis absorption and AFM measurements suggest that the apparent decrease in S at lower P3HT content results from contact of the water droplet with exposed regions of the silicon

substrate. This is reasonable given the likelihood of pinholes in the thin P3HT nanowire mats that result from low initial P3HT loading fractions. Because the native oxide present on the silicon wafer substrate is hydrophilic, the existence of pinholes will reduce the effective solid-liquid interfacial energy, decreasing the droplet contact angle, leading to an apparently low roughness factor. Photovoltaic device measurements show that these low weight fraction P3HT content P3HT/PS blends do not yield efficient device performance (Figure 5.13). In some cases (initial P3HT < 20 wt. %) PV performance is entirely absent as a result of pinholes in the P3HT leading to shunt pathways between the cathode and anode.

The SEM image of nanowires persisting after treatment with that solvent system used for backfilling (Figure 5.10) suggests that backfilling does not dissolve the P3HT nanowire network and does not lead to any significant plasticizing effects (which could allow the diffusion of, say the PCBM). Still, we note that it is known that there can be bilayer mixing in P3HT and PCBM layers formed by solution processing even without thermal annealing and even when supposedly orthogonal solvents are used;[229] consequently, it is possible that there is intermixing in our planar-prepared and backfilled P3HT nanowire films. The WAXS data presented in Figure 5.11 suggests that any such mixing does not significantly affect P3HT crystallinity.

It is known that annealing causes some intermixing between sequentially deposited P3HT and PCBM layers,[207, 210, 230-233] and the extent of this mixing can be very significant for > 100 °C.[207, 232] Therefore in this study it could be expected that the sequentially deposited layers of P3HT and acceptor material (PCBM or CdSe NCs) do not form a discrete interface, but more likely form a mixed region near to the nominal donor-acceptor interface. The intermixing of P3HT and PCBM has been found to occur predominantly through intercalation of PCBM into regions of amorphous P3HT, but does not impact the structure or morphology of existing P3HT crystallites. However, in light of

the high P3HT crystallinity and lower annealing temperature (75 °C) employed in this study, relatively little PCBM is expected to diffuse into the P3HT phase due to annealing,[207, 232] thus preserving the morphological distinction between planar-prepared and nanowire blends.

In PV devices fabricated from P3HT nanowire films backfilled with PCBM J_{sc} increases by 870% relative to that of planar-prepared film devices (for which there may be some intermixing between the P3HT and PCBM layers), yielding a 840% relative increase in PCE. Similar to PCBM backfilled devices, we observe an 840% increase in J_{sc} for hybrid P3HT/CdSe NC nanowire devices compared to a similar planar-prepared device. However, the FF (0.26) associated with an "S"-shaped J-V curve is relatively low, so the hybrid nanowire device exhibits a comparatively modest 270% increase in PCE compared to a similar planar-prepared device. The low FF observed for the nanowire hybrid NC device may be the result of an increase in the number of interfacial trap sites[234-238] arising from both increased surface area as well as the presence of unbound pyridine in the NC solution.[239]

Photovoltaic devices fabricated by backfilling the P3HT nanowires with an acceptor material are more efficient than the corresponding planar-prepared devices, likely as a result of higher active volume fraction of P3HT with the nanowire morphology (even with some interphase mixing in the planar-prepared devices); the P3HT crystallinity is expected to be high in both structures. Moreover, PV devices with the highest PCE correspond to films possessing the largest *S* and smallest *f*, suggesting a direct correlation between surface area, film porosity, and active volume of the P3HT phase of a BHJ PV device, and that the reduced dimensionality of the nanowire morphology enables a larger fraction of photo-excited excitons to be extracted from the P3HT phase.

5.5 Conclusions

A method is described to fabricate large surface-area networks of crystalline P3HT nanowires in which the PS phase is removed from blended P3HT/PS films. Photovoltaic devices fabricated by backfilling these P3HT nanowire structures with an acceptor materials results in PV devices with enhanced PCE. Increases in PCE of 840% and 270% are observed in devices backfilled with PCBM and CdSe NCs respectively compared to planar-bilayer-prepared devices. The observed increase in PCE results from an increase in J_{sc} attributed to greater active volume within BHJ devices containing a P3HT nanowire morphology. PV devices fabricated from P3HT nanowire films backfilled with CdSe NCs demonstrate the unique capability of combining both organic and inorganic materials in a device with well-defined BHJ morphology. This two-step process enables scalable, on-chip fabrication of P3HT nanowire networks for large BHJ interfacial areas and holds promise for bringing together complementary materials in a BHJ geometry that cannot be cast simultaneously with the traditional one-step casting methods.

This work discussed in this chapter has been published:

T. J. Kramer, A. R. Chew, T. Schiros, I. Kymissis, and I. P. Herman, *J. Vac. Sci. Tech. B*: , **2013**, 31, 031209.

6 Small Molecule Terminated Nanocrystals for Electronic Device Applications

6.1 Introduction

The previous chapters of this thesis have explored several examples of how nanocrystal (NC) composite materials can exhibit novel and useful properties. In each case a critical aspect of the composite material performance was the NC-organic interface. In Chapter 3 we showed that, following electrophoretic deposition (EPD), the surface of sparsely-passivated NCs can be replenished with new ligands [trioctylphosphine oxide (TOPO)], leading to an EPD NC film with reduced elastic modulus but greatly enhanced PL. Chapter 4 explored the addition of various monomers to as-deposited EPD NC films that, following polymerization, preserved film modulus while increasing the elasticity and PL efficiency of the composite material. We showed in Chapter 5 that by exposing nanoscale free surfaces in a semiconducting polymer it is possible to create a novel NC composite material that is suitable for photovoltaic (PV) applications. In each case the chemical or morphological properties of the NC-organic interface were controlled to achieve enhanced composite material performance.

In this chapter we will examine the results of several short exploratory studies that demonstrate the use of EPD in conjunction with novel organic ligands to create EPD NC films with enhanced functionality. In particular we will explore the use of very small or conjugated ligands that facilitate EPD and are expected enhance charge transfer between inorganic NCs and a surrounding medium. We will then show that by using spatially selective EPD of NCs on patterned substrates it is possible to control the location and fracture characteristics of EPD NC films. Patterned EPD NC films of this type are used to create a novel photo-active device with lateral (in-

plane) donor-acceptor interfaces. These studies, in aggregate, demonstrate the importance of controlling NC interfaces within EPD films to yield functional NC composite materials.

6.2 Novel Ligands for EPD NC Films

NCs capped with small organic ligands are capable of exchanging carriers or energy with a surrounding material. In some cases, the use of a ligand that can be removed through subsequent processing may lead to a material that exhibits bulk-like properties but that can be easily solution processed using methods such as spin-casting, ink-jet printing, and EPD.

Chapter 3 and Chapter 4 of this thesis explored the use of EPD to deposit dense films of cadmium selenide (CdSe) NCs capped with phosphonate molecules (TOPO, tetradecylphosphonic acid, and trioctylphosphine) In this chapter we will discuss three separate techniques to produce CdSe NCs, PbS NCs, and ZnO NCs whose surfaces are capped with phenylphosphonic acid (Section 6.1.1), naphthoic acid (Section 6.1.2), and ammonium chloride (6.1.3) ligands respectively (Figure 6.1). We will also discuss preliminary results in which chloride-terminated CdSe NCs have been deposited using EPD. These NCs were selected, in part, based on the optical and electronic properties of the NC core. Specifically, each type of NC has the ability to absorb in a unique region of the optical spectrum (ZnO absorbs in the UV and visible, CdSe absorbs in the visible, and PbS absorbs in the near-IR) and therefore has potential application in a variety of PV and sensing applications. These NCs can be used separately to absorb/emit light in a particular portion of the optical spectrum, or used together to achieve broad-band absorption/emission. The ligands in each case were selected based on the criteria that they provide strong electronic coupling between the NC core and the surrounding environment by virtue of their size (< 1 nm), and in the case of phenylphosphonic acid (PPA) and naphthoic acid (NA), their conjugated electronic structure. We

go on to deposit the above NCs using EPD to demonstrate the potential of solution processing to create useful nanoscale materials for device applications.

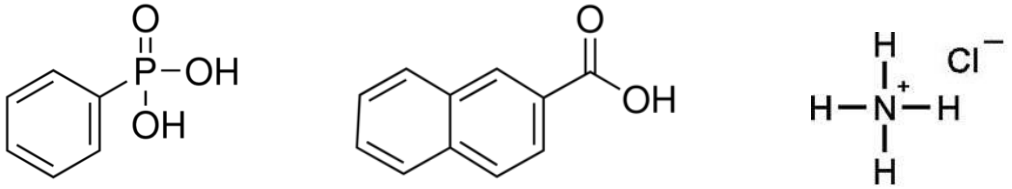

(a) (b) (c)

Figure 6.1: Molecular structure of (a) phenylphosphonic acid, (b) 2-naphthoic acid, and (c) ammonium chloride.

6.2.1 Phenylphosphonic Acid Terminated CdSe NCs

New synthetic techniques were developed in order to synthesize CdSe NCs with small conjugated ligands. Specifically, in Section 2.2.3 it was shown that by addition of phenylphosphonic acid (PPA, Figure 6.1a) to a solution of high-purity TOPO (lacking phosphonate impurities) the synthesis of CdSe NCs could be modified such that the resulting NCs were passivized with PPA (as demonstrated by solubility characteristics). The PPA molecule is approximately 0.6 nm in size and contains a conjugated phenyl group with delocalized sp^2-hybridized electrons. By virtue of its size and electronic structure the PPA molecule is expected to offer enhanced electronic coupling between the CdSe NC core and the surrounding environment compared to a larger, insulating, TOPO molecule.

The solubility characteristics of PPA-capped CdSe NCs provide evidence that the NC surface is dominated by PPA molecules and does not contain a substantial quantity of TOPO molecules. The presence of the phenyl group on the PPA molecule leads to good NC solubility in aromatic solvents such as benzene, chlorobenzene, and toluene. This is the result of favorable π-π electronic interactions between the solvent and ligand molecules. Unlike TOPO-capped CdSe NCs, PPA-capped NCs are not soluble in alkyl chain type solvents such as hexane and octane. A TEM image of 4.6 nm

diameter CdSe-PPA particles and a corresponding absorption spectrum (in chlorobenzene) is seen in Figure 6.2a and Figure 6.2b respectively.

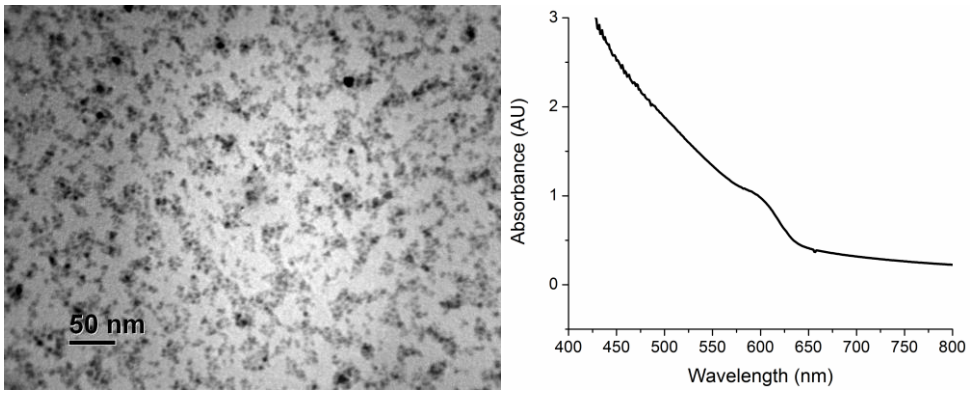

(a) (b)

Figure 6.2: (a) TEM image of drop-cast film of CdSe-PPA NCs, and (b) absorption spectrum of same particles in a solution of chlorobenzene.

The as-synthesized particles can be deposited from a toluene solution using EPD (500 V bias at 2 cm electrode separation) and form a thick, dense NC film only on the positive electrode. Figure 6.3 shows a typical EPD film composed of CdSe-PPA NCs. Unlike TOPO-capped CdSe NCs it is apparent that the cracks in the CdSe-PPA EPD film are relatively straight. This result indicates that the film has lower toughness than a similar film comprised of CdSe-TOPO and is consistent with greater van der Waals bonding between TOPO ligands compared to PPA ligands. When chloroform is added to the toluene (~10 vol. %), it is found that an EPD film forms on the negative electrode and is of low quality.

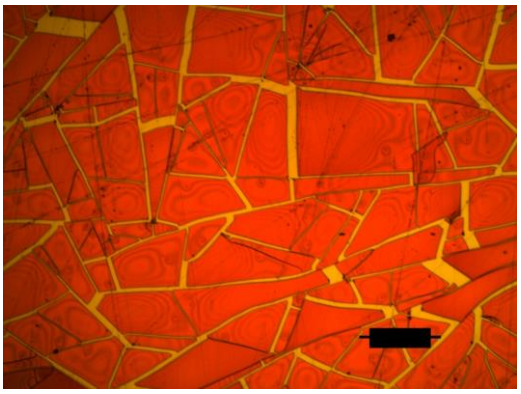

Figure 6.3: EPD film (positive electrode) of phenylphosphonic acid terminated CdSe NCs deposited from toluene. Scale bar is 100 µm wide.

6.2.2 Naphthoic Acid Terminated PbS NCs

Using techniques described in Section 2.3.2, naphthoic acid (NA, Figure 6.1b) terminated PbS NCs were synthesized. Unlike traditional synthetic routes utilizing oleic acid, we showed that NA can be used to complex the lead (II) cation in a high boiling-point aromatic solvent (dibenzylether) and subsequently reacted with a sulfur precursor (trimethyl siloxane-sulfide) to yield PbS-NA NCs. As confirmed by TEM (Figure 6.4a) and NIR absorption measurements carried out in toluene (Figure 6.4b), these PbS-NA NCs are estimated to have a diameter of approximately 2 nm. PbS-NA NCs are highly soluble in aromatic solvents but are not soluble in alkyl chain-type solvents; indicating a NC surface dominated by conjugated NA ligands. Professor Owen's group in the Department of Chemistry at Columbia University has shown that CdSe-NA NCs can be synthesized and exhibit interesting electronic and optical characteristics attributed to the small conjugated structure of the naphthoic acid ligand. [28]

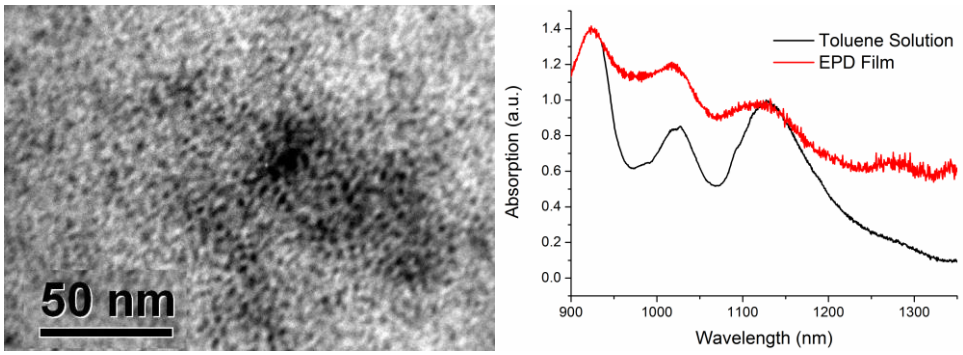

(a) (b)

Figure 6.4: (a) TEM image of naphthoic acid terminated PbS NCs, and (b) absorption spectrum of the same particles in a toluene solution (black), and of an EPD film (positive electrode) deposited on an ITO substrate (red).

PbS-NA NCs, shown in Figure 6.4, can be deposited from hexane using EPD to form thick films on only the negative electrode. EPD was carried out at 200 V with an electrode separation of 2 cm. The resulting EPD film can be deposited in excess of 1 μm thick and fractures upon drying (Figure 6.5). Similar to the results obtained for CdSe-PPA, the fracture pattern seen in Figure 6.5 is dominated by relatively straight cracks, suggesting the PbS-NA film is relatively brittle. The absorption profile of an EPD PbS-NA film deposited on an ITO substrate (Figure 6.4b) shows that the first excitonic absorption peak of the film is at the same wavelength as the same particles in solution, indicating that EPD does not lead to sintering of PbS-NA particles and that quantum confinement is maintained.

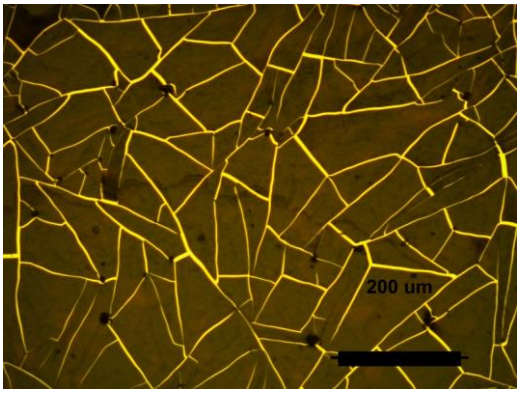

Figure 6.5: EPD film (positive electrode) of naphthoic acid-terminated PbS NCs. Scale bar is 200 μm wide.

The ability of PbS NCs to absorb in the NIR portion of the solar spectrum would make them an attractive sensitizing agent for PV devices; increasing the NIR absorption increasing PV efficiency. Additionally, the conjugated structure of the NA molecule is expected to offer superior charge transport[25] between the PbS core and the surrounding environment compared to alkyl chain-type ligands such as TOPO. Together CdSe-PPA and PbS-NA NCs of various sizes could be used to absorb over virtually the full range of the visible (CdSe) and near-IR (PbS) solar spectrum and could therefore be combined in a PV device to yield efficient broad-band performance. The ability to deposit both CdSe-PPA and PbS-NA NCs using EPD is also important and could enable selective deposition of NCs on PV device substrates (this concept is explored later in this chapter).

6.2.3 Chloride-terminated CdSe NCs

Recently the Owen group developed a technique for the synthesis of CdSe NCs with chloride ligands (CdSe-Cl).[240] As shown in Figure 6.6 the surface of these NCs is primarily chloride terminated, but may have small quantities of phosphine or amine ligands as well. In this study only phosphine-type CdSe-Cl NCs were investigated. The resulting CdSe-Cl NCs are highly monodisperse (Figure 6.6c) and show clear signs of quantum confinement.[240] In addition to the small size of the chloride ligand, which is expected to facilitate efficient charge transfer, the chloride ligands greatly increase the solubility of CdSe-Cl in polar solvents such as dimethylsulfoxide (DMSO) and acetonitrile (ACN).

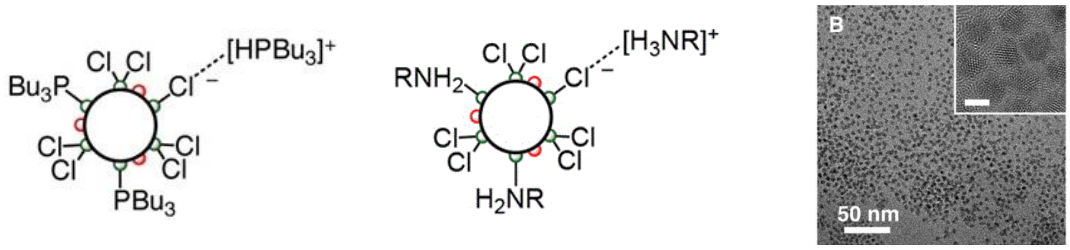

(a) (b) (c)

Figure 6.6: Depiction of surface species present on chloride-terminated CdSe NCs synthesized using (a) phosphine precursor, (b) amine precursor, and (c) TEM image of chloride/phosphine-terminated CdSe NCs. Figures reproduced from Ref. 240.

CdSe-Cl NCs with a diameter of approximately 3.4 nm were prepared by the Owen group using a phosphine precursor ligand and were deposited using EPD. Several deposition solvents were tested as well a variety of deposition conditions. Solvents investigated included toluene, chloroform, dimethylsulfoxide (DMSO), and acetonitrile (ACN). Deposition voltages of between 2 – 200 V were applied between ITO electrodes positioned 1 cm apart. Of the solvents investigated, EPD of CdSe-Cl NCs occurred only in ACN and DMSO. EPD in ACN was possible only at 2 V and occurred only on the negative electrode, indicating that deposition may occur via electrochemical reduction of the chloride counter-ion. At deposition voltages above 2 V in ACN the deposition current increased rapidly which may indicate electrochemical degradation of the deposition solvent. In contrast, in DMSO a higher deposition voltage of 100 - 200 V was necessary to accomplish EPD, also leading to deposition only on the negative ITO electrode. Figure 6.7 shows an EPD CdSe-Cl NC film deposited on the negative electrode from an ACN solution.

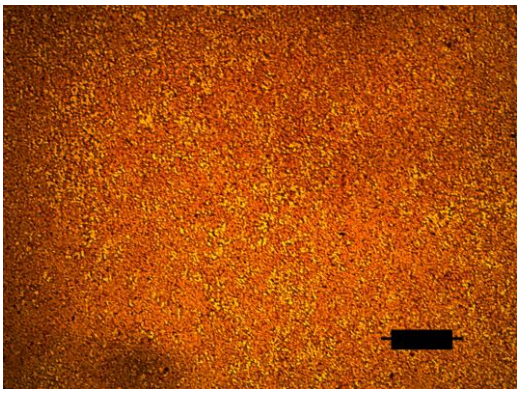

Figure 6.7: EPD film of phosphine-type chloride-terminated CdSe NCs deposited on ITO substrate (negative electrode). Scale bar is 100 μm wide.

6.3 Using Patterned Electrodes for Spatially-selective EPD

In the preceding sections we explored the use of EPD to deposit NCs with a variety of novel ligands that are expected to offer enhanced charge transfer with the NC core. If NCs of this type are to be used in devices it will likely be necessary to control the physical location of the EPD film with a high degree of precision. Previous work has shown that utilizing patterned electrodes it is possible to achieve spatially selective deposition of CdSe NCs using EPD.[45] In this section we will present results of selective EPD of CdSe NCs on patterned electrodes of various geometries with micron-scale dimensions.

In addition to offering spatial selectivity, a hypothesis explored in this section is that fracture may be avoidable if the lateral (in-plane) dimension of the EPD NC film is sufficiently small that the EPD film can relax without stress levels exceeding the fracture strength of the dry NC film (this approach is in contrast to the results of Chapter 3 and Chapter 4 in which fracture of EPD NC films was suppressed by infusion of ligands and monomers to relieve strain). This hypothesis is supported by the observation that when an untreated, planar, EPD CdSe NC film undergoes fracture, the resulting islands of uncracked material are frequently of approximately the same size (area). This observation suggests that at a certain lateral scale, the traction forces exerted by the substrate

do not have sufficient distance to develop stresses exceeding the fracture strength (σ_f) of the dry NC film (see Chapter 3 for discussion of σ_f).

In order to investigate EPD NC film fracture on substrates of limited in-plane dimension, standard electron-beam lithography techniques were used (see Section 2.6.2) to generate micron-scale patterned gold electrodes on a Si wafer with a 500 nm thick thermal oxide layer. The patterned electrodes consisted of interconnected regions of Au on the insulating oxide substrate. Wire-bonding techniques were used to make electrical contact to the interconnected (patterned) electrodes. Using an unpatterned, planar Au counter-electrode (3 mm electrode separation), EPD of 3.5 nm diameter TOPO-capped CdSe NCs in hexane was carried out at 500 V until a film in excess of the critical fracture thickness (~ 600 nm) was deposited on the both the patterned electrode (negative) and planar counter electrode (positive). Of interest in each experiment was the dimension of the patterned electrode (in the confined dimension) at which cracks perpendicular to the confined dimension are not observed; corresponding to relaxation of the film in the confined dimension. Figure 6.8 and Figure 6.9 show optical micrographs of EPD of CdSe NCs on patterned Au electrodes. In these micrographs the red/orange regions are comprised on CdSe NCs overlying the Au electrode, while the lighter (purple/blue) regions are the underlying oxide layer of the wafer.

In order to determine at what length scale fracture of the EPD NC film was suppressed, one set of experiments was carried out in which EPD of CdSe NCs was carried out on patterned micron-scale electrodes consisting of interdigitating triangles (technically trapezoids). Figure 6.8a and Figure 6.8b show optical micrographs of EPD CdSe NC films deposited on approximately triangular Au electrodes that are 700 μm tall and have bases 100 μm wide and 50 μm wide respectively. The light regions between the red CdSe NC films are the exposed SiO_2 substrate. The arrows in Figure 6.8a indicate the position along the triangle length at which cracking perpendicular to the triangle

base is suppressed, corresponding to relaxation of the EPD NC film in the narrow dimension of the triangular electrode. It is apparent that at approximately half the triangle height, corresponding to a width of approximately 50 μm, cracking in Figure 6.8a is suppressed normal to the narrow dimension. Figure 6.8b provides slightly higher resolution and shows that cracking in the narrow dimension of the EPD NC film is suppressed when the dimension of the film is approximately 30 μm or less.

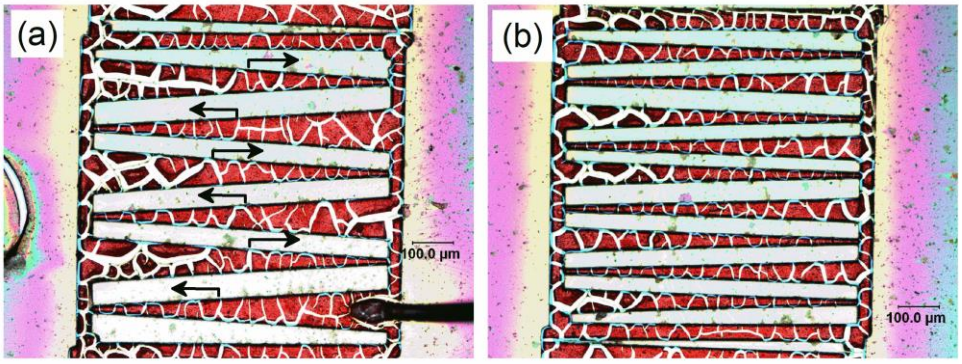

Figure 6.8: EPD CdSe NC (3.8 nm diameter) films deposited on patterned Au (negative electrode) located on SiO_2 substrate: (a) triangles 100 μm wide at the base and 700 μm tall (b) triangles 50 μm wide at the base and 700 μm tall. Light-colored regions between Au electrodes (over coated with CdSe NCs) are exposed SiO_2 50 μm wide and 25 μm wide in (a) and (b) respectively. The lower right corner of (a) shows contact point of wire-bond pad used to make electrical contact with the patterned electrode.

Figure 6.9a-b shows the result of confining the lateral dimension of an EPD NC film in two dimensions simultaneously by depositing on interconnected circular and square Au (negative) electrodes. From Figure 6.9a it is apparent that cracking is fully suppressed for circular electrodes 30 μm or less in diameter. Figure 6.9b shows that, for square electrodes, fracture of the EPD NC film can occur when the square film is 30 μm on a side, but is fully suppressed for square films 20 μm or less in dimension. This agrees with Figure 6.9c that shows cracking of a EPD CdSe NC film

on interconnected, concentric, ring-shaped Au electrodes is suppressed in the confined dimension (radial direction) when the width of the ring-shaped electrode is 20 μm or less.

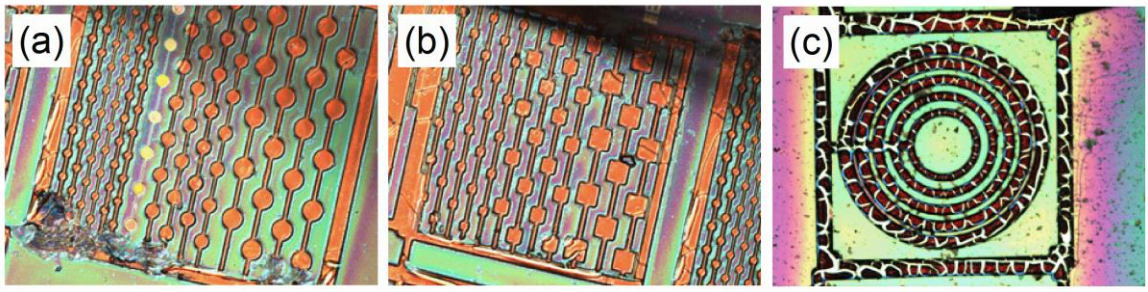

Figure 6.9: EPD films of CdSe NCs on negative electrode comprised of (a) interconnected circular Au pads with diameters of 10 μm, 20 μm, and 30 μm, (b) square pads with widths of 10 μm, 20 μm, and 30 μm, and (c) interconnected rings with widths of 10 μm (inner), 15 μm, 20 μm, 25 μm, and 30 μm (outer).

The observation that cracking is completely suppressed in EPD NC films that are confined in two dimensions (of sufficiently small size) is not surprising given that the in-plane stress (and strain) of the film is a function of two orthogonal in-plane stresses (σ_x and σ_y). By reducing stress and strain in both dimensions simultaneously we have shown that it is possible to avoid fracture in EPD NC films, even when the films are above the critical thickness for fracture of a macroscopic film (see Section 3.4).

6.4 Application of EPD on Patterned Electrodes for the Fabrication of NC-sensitized Photovoltaic Devices

Unlike bottom-up solution-phase particle synthesis, lithography can be used as a top-down technique to generate interesting nanoscale interfaces with precise spatial location. In this section we explore the use of lithographically-defined interdigitating electrodes (IDEs) used in conjunction with EPD to create heterojunctions between dissimilar NCs, with potential application for photovoltaic (PV) applications.

The IDE device architecture is unique in that locates both cathode and anode electrodes on the same substrate, and produces current as a result of lateral (in-plane) charge separation at the donor-acceptor interface. PV devices based on the IDE architecture can be fabricated from a variety of low-cost and potentially flexible substrates, reducing the cost of the final device.[241] In contrast, traditional PV devices utilize planar donor-acceptor interfaces and rely on out-of-plane charge separation. To achieve illumination of the full active area (and to attain high efficiency) these traditional planar PV devices require one electrode (typically the anode) to be a transparent conductor such as indium-tin oxide (ITO. Traditionally the transparent conducting electrode is a major cost in PV device fabrication.[241]

Previous work has shown that lithographically defined, interdigitated electrode (IDE) architectures, can be used to achieve spatially selective electroplating of II-VI semiconductors and generate useful PV devices.[242] Alternatively it is also possible to yield PV devices by application of planar organic films over micron-scale patterned electrodes.[243, 244] In this section we show that EPD offers the unique capability to selectively functionalize a single set of IDE electrodes with inorganic NCs. The functionalized electrode array can then be over coated with a complementary material to yield a planar film comprised of lateral donor-acceptor interfaces.

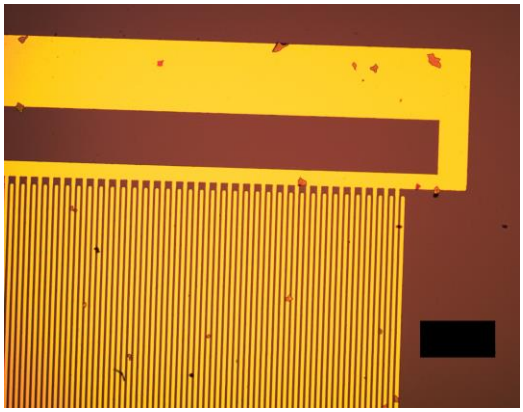

Figure 6.10: Interdigitated gold electrodes with common bus-bar connecting alternating electrodes. The common bus-bar connecting the other set of alternating electrodes is not shown. Scale bar is 100 μm wide.

As seen in Figure 6.10, an array of interdigitating gold electrodes was fabricated using standard PMMA/e-beam lithography techniques (see Section 2.6.2 for details). Adjacent electrodes are electrically isolated, while every other electrode is electrically connected to a common bus bar. An electrode of this type can be configured in several ways that allow selective EPD of NCs onto a single set of alternating electrodes. In one type of configuration, called "opposing electrode configuration", a potential is applied between a single set of electrodes and a separate, planar electrode held parallel at a fixed distance 1 cm away. In accordance with the mechanism of EPD, NCs with a non-zero zeta potential will move to a single set of (alternating) electrodes under the influence of the electric field. When utilized in this manner, deposition is expected to occur predominantly on the electrode surface facing away from the substrate (and toward the opposing planar electrode). Figure 6.11 shows a film of ZnO NCs (prepared according to techniques describe in Section 2.4) deposited on a single set of (negative) IDE electrodes utilizing EPD in the opposing-electrode configuration. Deposition was carried out at 20 V in DMSO for 3 minutes with the planar (positive) electrode held parallel and 1 cm apart from the IDE substrate. No deposition was observed on the planar, positive electrode.

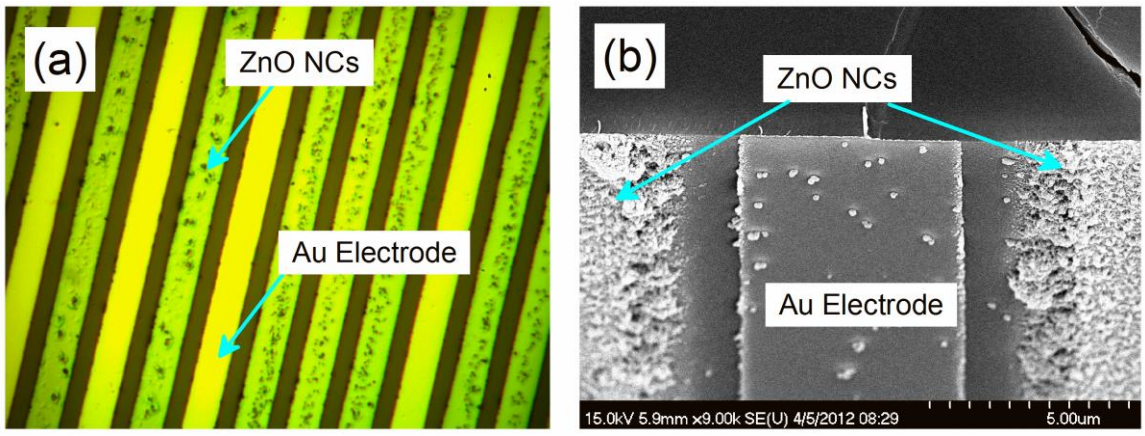

Figure 6.11: (a) An optical micrograph and (b) SEM image of ZnO NCs deposited using EPD on alternating Au electrodes using an opposing-electrode configuration. "Au Electrode" denotes floating set of electrodes. Electrode widths are 5 μm.

As described in Section 2.4, these ZnO NCs were passivated with ammonium ions (Figure 6.1), which are small and can be removed using chemical or thermal techniques. The ease with which ammonium ligands can be removed from the NC surface is important and, in contrast to traditional ligands such as tetramethylammonium, will facilitate sintering of the ZnO NC film into a "bulk" film which could offer superior electron transport.

Alternatively, as shown in Figure 6.12, it is possible to apply a voltage between the two sets of electrically isolated sets of electrodes on the same substrate. While this technique has been used before to deposit carbon nanotubes using dielectrophoresis,[245] to our knowledge this is the first time it has been used to selectively functionalize an IDE PV device with inorganic NCs. This configuration, called "on-chip" deposition, leads to electric field lines that lie primarily in the plane of the electrode substrate and extend between adjacent electrodes. When used in this manner EPD is expected to result in NC films that deposit primarily on the electrode faces that are perpendicular to the substrate and face the neighboring electrode. This result is confirmed by the SEM image shown in Figure 6.12.

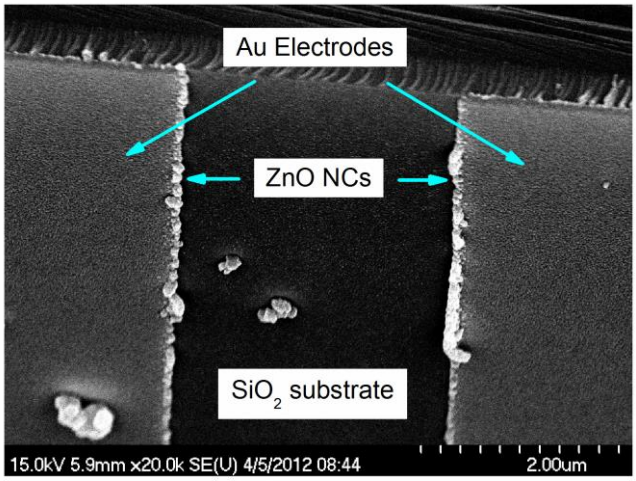

Figure 6.12: On-chip EPD of ZnO NCs on interdigitated Au electrodes. Right electrode was held at – 75 mV while left electrode was held at + 75 mV. EPD was carried out for 3 minutes in a solution of DMSO.

Using the opposing-electrode configuration a simple PV device was fabricated by spin-casting a solution of pyridine-capped CdSe NCs over an array of interdigitated electrodes that had been selectively deposited with ZnO NCs using EPD. A cross-section SEM image of this structure is seen in Figure 6.13. It is apparent from Figure 6.13 that there is partial separation of the relatively thin ZnO NC EPD film and the thicker over-lying CdSe NC film.

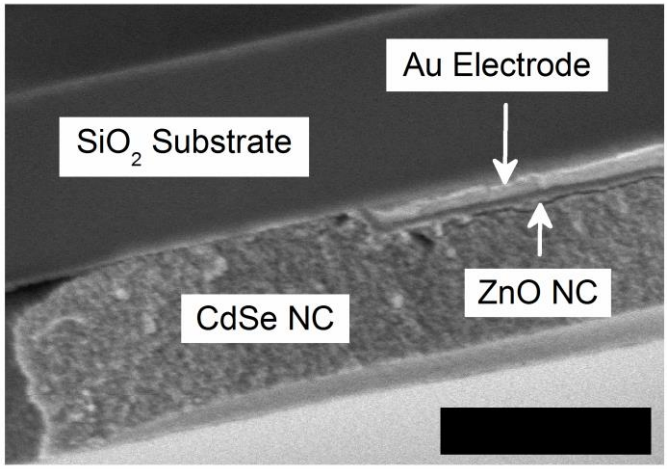

Figure 6.13: Cross-sectional SEM image of ZnO NC/CdSe NC interface generated on an interdigitated electrode substrate. Scale bar is 500 nm wide.

In this exploratory study this device did not exhibit true photovoltaic performance (i.e. did not generate a voltage)[71] when exposed to simulated solar illumination. However, it did exhibit an asymmetric I-V curve, suggesting the existence of a hetero-interface between adjacent electrodes. Furthermore, under a forward-bias condition (ZnO NC-decorated surfaces held at negative potential), there was an appreciable increase in photocurrent suggesting that photo-generated excitons are converted to electrical current.

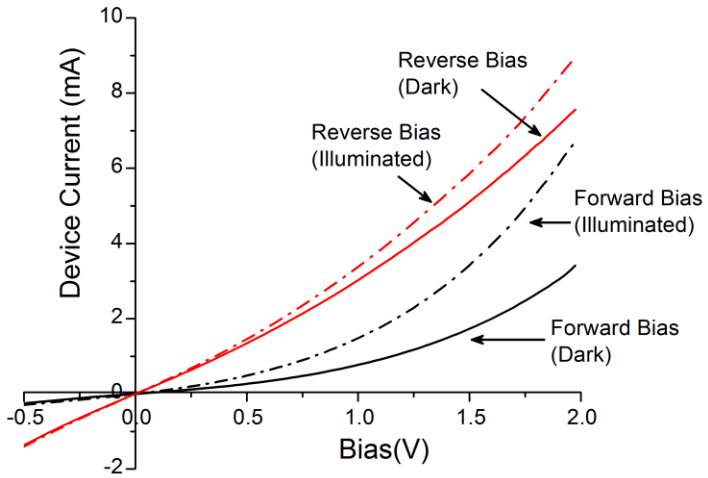

Figure 6.14: I-V curve of ZnO NC/CdSe NC PV device fabricated from an interdigitated electrode array.

6.5 Conclusions

It is apparent from the above work that the surface modification of various NCs through choice of ligand can be coupled with EPD from organic solvents to generate novel materials. These materials, composed primarily of NCs, exhibit the optical properties consistent with quantum confinement of carriers within the NCs, and can be located precisely on a patterned conductive substrate using EPD. Furthermore, patterning of EPD NC films using micron-scale electrodes has been shown to prevent NC film fracture and may be a useful tool in the fabrication of devices and structures requiring spatially-complex and consistent NC functionalization. By careful selection of the NC ligand, it is possible to increase the electronic coupling of the NCs with a surrounding material, making these materials promising for use in a variety of applications such as chemical sensing and PV devices requiring exchange of energy with the NC phase.

7 Summary and Future Directions

7.1 Summary of Results

In this thesis we have explored techniques for generating functional nanocrystal composites using two-step back-filling methods and have studied the properties of the resulting nanomaterials. By decoupling the placement of organic and inorganic (NC) phases we are able to utilize phase-specific (i.e. NC or organic) processing techniques such as electrophoretic deposition (EPD) and templated organic nanowire growth to generate novel nanostructures with potential application in the fields of advanced optical coatings, chemical sensing, and photovoltaics (PVs).

EPD of inorganic nanoparticles has been extensively studied and has merit as a scalable technique for spatially selective deposition of inorganic NC films. Hindering its implementation (to date) has been the tendency of EPD NC films to fracture due to loss of deposition solvent when dried and the resulting strain in the adhering NC film. The suppression of fracture in EPD NC films through back-filling with a complementary organic material is an important advancement to the technique of NC EPD. We have shown two promising strategies for suppression of fracture in EPD NC films, including addition of organic ligand molecules and the addition of polymeric precursor materials to as-deposited films. In addition to proving highly effective at suppressing fracture, these back-fill methods offer the ability to create NC composites with useful mechanical, optical, and electronic properties.

Back-fill methods have also proven useful in creating photovoltaic nanocomposite materials from organic nanowires. A novel synthetic route for the fabrication of dense, organic semiconducting, P3HT nanowire mats was demonstrated. These films of organic nanowires have high surface area and a nanoscale morphology that makes them well suited for decoration with NCs to yield hybrid NC/organic bulk-heterojunction structures. We have shown that a nanocomposite

material with bulk-heterojunction architecture can be created by back-filling the exposed nanowire mat with CdSe NCs to yield a photovoltaic material. The versatility of this method makes it amenable to the use of many different types of NC and could provide a low-cost and scalable method for the fabrication of hybrid PV devices.

7.2 Future Work

Despite the successful implementation of back-fill methods presented in this thesis, there remains substantial opportunity to improve upon these results through exploration of various other combinations of organic and inorganic NC materials. One opportunity lies in the prospect of back-filling EPD NC films with conductive/semiconducting/photoconductive organic material to create NC films with precise spatial resolution and novel optoelectronic properties. Building on the work presented in Chapter 5, we also see value in applying the method of back-filling organic nanowire films with a variety of inorganic NCs. In each case, the general methods developed in this thesis are expected to be applicable to the realization of new nanocomposite materials with novel properties.

7.2.1 Conductive Ligands for EPD NC Film Stabilization

Conductive (or more likely photo-conductive) ligands will be an important category of organic materials to investigate for their potential to suppress fracture in EPD NC films and lend the film improved electronic properties. Naphthoic acid, the ligand used in Chapter 6 to passivate PbS NCs represents one embodiment of this concept. There are likely other ligands that combine a binding head group such as a carboxylate group, cyano group, or phosphonate group with a photoconductive, conjugated moiety. Figure 7.1 shows the structure on one such molecule: a bis(styryl)benzene chain functionalized with cyano groups on the central benzene unit. A molecule of

this type has the desirable characteristics of possessing both electron withdrawing groups (cyano) and electron donating groups (nitrogen), leading to a donor-acceptor-donor structure that will reduce exciton binding and provide both electron and hole conduction pathways through the pure organic phase. The particular molecule picture in Figure 7.1 also has HOMO and LUMO levels appropriate to act as the donor phase when blended with CdSe NCs.[246] Other ligands, such as oligo-(phenylene vinylene),[247] 5-(pyridin-3-ylethynyl)picolinic acid,[248] and pentathiophene phosphonate [249] are just a few other ligands that are expected to bind to the surface of inorganic NCs and may provide both mechanical stabilization and improved EPD NC film conductivity.

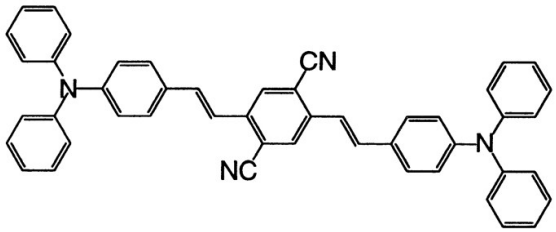

Figure 7.1: Molecular structure of cyano-functionalized bis(styryl)benzene molecule.[246]

7.2.2 Organic Semiconducting Polymers for EPD NC Film Stabilization

Building on the work discussed in Chapter 4, we believe there is an opportunity to stabilize EPD NC films with monomers that can be polymerized to form semiconducting polymer chains. A variety of techniques have been reported for the grafting of conjugated organic molecules to inorganic NCs in solution. Zhang et al. demonstrated the ability to graft polymers bearing conjugated Frechet-type polyether dendrons to the surface of CdS NCs in an aqueous solution (Figure 7.2).[250], while Skaff et al. used a Heck-type coupling reaction to coat CdSe NCs with poly(*para*-phenylene vinylene).[251] Many other techniques for polymerization of conjugated

polymers in the presence of NCs exist and could potentially be utilized to enhance the properties of EPD NC films through back-filling and subsequent polymerization.[249]

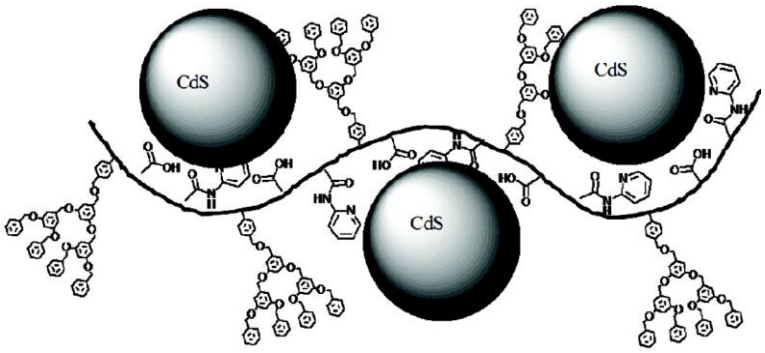

Figure 7.2: CdS NCs capped with Frechet-type polyether dendrons.[249, 250]

In order for one of these techniques to be compatible with the back-filling methodology explored in this thesis, several criteria must be met: The polymeric precursor material (i.e. monomer) must easily diffuse through the as-deposited EPD NC film, and must therefore have good miscibility with the NC ligand used during the EPD process. Additionally, the conditions of the polymerization reaction (solvent, catalyst, and temperature) must not damage individual NCs or dislodge the as deposited film. This will require a polymerization solvent that falls in specific range of NC/ligand solubility such that it is wetting to the as-deposited EPD NC film but does not solubilize the NCs sufficiently to dislodge or dissolve the film. The use of reactive polymerization catalysts must also be used conscientiously so as to avoid introduction of impurities that would reduce the performance (optical, electronic, etc.) of the final nanocomposite material.

7.3 Alternative NCs for Back-filling of P3HT Nanowire Films

As discussed in Chapter 1 and again in Chapter 6, inorganic NCs offer the ability to sensitize a composite material to a broad portion of the electromagnetic spectrum.[95, 116, 252] By selection of an appropriate NC type and size, the sensitivity of a nanocomposite PV material can be tuned to absorb

light in virtually all portions of the solar spectrum. ZnO, TiO_2, and SnO_2 NCs (just to name a few) absorb strongly in the UV portion of the solar spectrum. These materials are, in general, electron conductors[95] and well-suited to the role of acceptor-phase in a composite PV material. Other types of NCs such as PbS, CdTe, and Si[253] may be used to sensitize in the NIR region of the solar spectrum where conventional organic semiconductors cannot. Dictating the choice of NC will be its bandgap (i.e. absorption characteristics), and the relative position of the valence and conduction bands. As depicted in Figure 7.3, the position of the valence and conduction bands in an IR absorbing NC can cause it to behave as either an electron donor or acceptor. Since P3HT is known to preferentially conduct holes,[56] an acceptor-type NC with good electron mobility is a good choice for a P3HT/NC composite PV material. PbS NCs, with a valence band at approximately – 4.9 eV and an effective bandgap ranging from 0.6 – 1.7 eV (10 – 2.5 nm respectively)[32] meets these criteria and is a logical choice for back filling of P3HT nanowires to yield an IR-sensitized nanocomposite PV material.

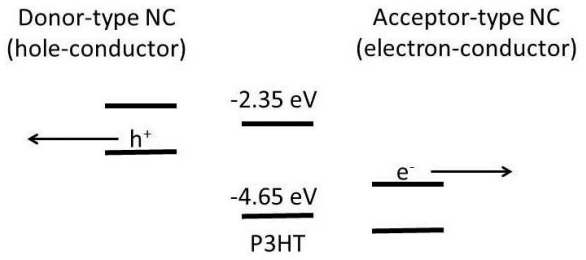

Figure 7.3: Depiction of relative valence and conduction band levels in IR-sensitizing NCs paired with P3HT.

7.4 Concluding Remarks

The work in this thesis builds on the industrious efforts of the scientists who laid the ground work for the field nanotechnology through the development of pioneering synthetic techniques, innovative experimentation, and careful theoretical analysis. Once considered a specialized field, nanotechnology has grown into an expansive subject that attracts many of the

world's greatest scientific minds and is a continuing source for new technologies that will undoubtedly shape the future of technology. If this thesis contributes in even the slightest way to the field of nanotechnology it will have been a success.

Bibliography

[1] J. Park, K. An, Y. Hwang, J.-G. Park, H.-J. Noh, J.-Y. Kim, J.-H. Park, N.-M. Hwang, and T. Hyeon, Nature Materials 3 (2004) 891.

[2] L. E. Brus, J. Chem. Phys. 79 (1983) 5566.

[3] N. C. Greenham, X. Peng, and A. P. Alivisatos, Physical Review B 54 (1996) 17628.

[4] B. Wetzel, F. Haupert, and M. Qiu Zhang, Composites Science and Technology 63 (2003) 2055.

[5] N. A. Hill and K. B. Whaley, Chemical Physics 210 (1996) 117.

[6] B. O. Dabbousi, J. Rodriguez-Viejo, F. V. Mikulec, J. R. Heine, H. Mattoussi, R. Ober, K. F. Jensen, and M. G. Bawendi, The Journal of Physical Chemistry B 101 (1997) 9463.

[7] S. Kim, B. Fisher, H.-J. Eisler, and M. Bawendi, Journal of the American Chemical Society 125 (2003) 11466.

[8] W. W. Yu, L. Qu, W. Guo, and X. Peng, Chemistry of Materials 15 (2003) 2854.

[9] C. R. Bealing, W. J. Baumgardner, J. J. Choi, T. Hanrath, and R. G. Hennig, ACS Nano 6 (2012) 2118.

[10] H. Liu, J. S. Owen, and A. P. Alivisatos, Journal of the American Chemical Society 129 (2006) 305.

[11] J. A. Christiansen, ACTA Chemica Scandinavica (1954) 909.

[12] J. S. Owen, E. M. Chan, H. Liu, and A. P. Alivisatos, Journal of the American Chemical Society 132 (2010) 18206.

[13] M. M. Rahman, Nucleation and Growth of TiO2 Nanoparticles, Nanomaterials, Sharif University of Technology, Tehran, 2011.

[14] Y. Yin and A. P. Alivisatos, Nature 437 (2005) 664.

[15] N. Pradhan, D. Reifsnyder, R. Xie, J. Aldana, and X. Peng, Journal of the American Chemical Society 129 (2007) 9500.

[16] Q. Lu, F. Gao, and D. Zhao, Nano Letters 2 (2002) 725.

[17] J. Y. Rempel, B. L. Trout, M. G. Bawendi, and K. F. Jensen, The Journal of Physical Chemistry B 110 (2006) 18007.

[18] P. O. Anikeeva, J. E. Halpert, M. G. Bawendi, and V. Bulović, Nano Letters 9 (2009) 2532.

[19] X. Peng, M. C. Schlamp, A. V. Kadavanich, and A. P. Alivisatos, Journal of the American Chemical Society 119 (1997) 7019.

[20] S. A. Ivanov, A. Piryatinski, J. Nanda, S. Tretiak, K. R. Zavadil, W. O. Wallace, D. Werder, and V. I. Klimov, Journal of the American Chemical Society 129 (2007) 11708.

[21] B. Fiedler, F. H. Gojny, M. H. G. Wichmann, M. C. M. Nolte, and K. Schulte, Composites Science and Technology 66 (2006) 3115.

[22] P. V. Kamat, The Journal of Physical Chemistry C 112 (2008) 18737.

[23] S. N. Sharma, Z. S. Pillai, and P. V. Kamat, The Journal of Physical Chemistry B 107 (2003) 10088.

[24] J. H. Bang and P. V. Kamat, ACS Nano 5 (2011) 9421.

[25] W. Warta, R. Stehle, and N. Karl, Applied Physics A 36 (1985) 163.

[26] M. V. Kovalenko, M. Scheele, and D. V. Talapin, Science 324 (2009) 1417.

[27] K. A. Mazzio, K. Okamoto, Z. Li, S. Gutmann, E. Strein, D. S. Ginger, R. Schlaf, and C. K. Luscombe, Chemical Communications 49 (2013) 1321.

[28] B. M. Cossairt, P. Juhas, S. J. L. Billinge, and J. S. Owen, The Journal of Physical Chemistry Letters 2 (2011) 3075.

[29] C. B. Murray, D. J. Norris, and M. G. Bawendi, Journal of the American Chemical Society 115 (1993) 8706.

[30] W. W. Yu and X. Peng, Angewandte Chemie International Edition 41 (2002) 2368.

[31] J. S. Owen, J. Park, P.-E. Trudeau, and A. P. Alivisatos, Journal of the American Chemical Society 130 (2008) 12279.

[32] J. Jasieniak, M. Califano, and S. E. Watkins, ACS Nano 5 (2011) 5888.

[33] Y. Zhou, H. Itoh, T. Uemura, K. Naka, and Y. Chujo, Langmuir 18 (2002) 5287.

[34] T. Trindade, P. O'Brien, and N. L. Pickett, Chemistry of Materials 13 (2001) 3843.

[35] N. Pradhan and S. Efrima, Journal of the American Chemical Society 125 (2003) 2050.

[36] M. A. Hines and G. D. Scholes, Advanced Materials 15 (2003) 1844.

[37] D. B. Hall, P. Underhill, and J. M. Torkelson, Polymer Engineering & Science 38 (1998) 2039.

[38] W. W. Flack, D. S. Soong, A. T. Bell, and D. W. Hess, Journal of Applied Physics 56 (1984) 1199.

[39] A. G. Emslie, F. T. Bonner, and L. G. Peck, Journal of Applied Physics 29 (1958) 858.

[40] D. R. Brown and F. W. Salt, Journal of Applied Chemistry 15 (1965) 40.

[41] C. P. Gutierrez, J. R. Mosley, and T. C. Wallace, Journal of The Electrochemical Society 109 (1962) 923.

[42] J. C. Dunbar and T. J. Mitchell, Journal of the Science of Food and Agriculture 4 (1953) 190.

[43] H. Koelmans and J. T. G. Overbeek, Discussions of the Faraday Society 18 (1954) 52.

[44] J. Dickerson, in Electrophoretic Deposition of Nanomaterials (J. H. Dickerson and A. R. Boccaccini, eds.), Springer New York, 2012, p. 131.

[45] M. A. Islam and I. P. Herman, Appl. Phys. Lett. 80 (2002) 3823.

[46] S. Jia, S. Banerjee, and I. P. Herman, The Journal of Physical Chemistry C 112 (2007) 162.

[47] M. A. Islam, Y. Xia, J. D. A. Telesca, M. L. Steigerwald, and I. P. Herman, Chem. Mater. 16 (2004) 49.

[48] M. A. Islam, Y. Xia, M. L. Steigerwald, M. Yin, Z. Liu, S. O'Brien, R. Levicky, and I. P. Herman, Nano Lett. 3 (2003) 1603.

[49] A. Singh, N. J. English, and K. M. Ryan, The Journal of Physical Chemistry B 117 (2012) 1608.

[50] I. D. Morrison, Colloids and Surfaces A: Physicochemical and Engineering Aspects 71 (1993) 1.

[51] M. A. Islam, Y. Xia, D. A. Telesca, M. L. Steigerwald, and I. P. Herman, Chemistry of Materials 16 (2003) 49.

[52] S. Shoaee, T. M. Clarke, M. P. Eng, C. Huang, S. Barlow, E. Espíldora, J. Luis Delgado, B. Campo, S. R. Marder, M. Heeney, I. McCulloch, N. Martín, D. Vanderzande, and J. R. Durrant, Journal of Photonics for Energy 2 (2012) 021001.

[53] http://www.uea.ac.uk/~c286/aromaticnotes.htm.

[54] P. E. Shaw, A. Ruseckas, and I. D. W. Samuel, Advanced Materials 20 (2008) 3516.

[55] W. Barford, University of Cambridge, 2013.

[56] S. Shoaee, T. M. Clarke, C. Huang, S. Barlow, S. R. Marder, M. Heeney, I. McCulloch, and J. R. Durrant, Journal of the American Chemical Society 132 (2010) 12919.

[57] H. Sirringhaus, Advanced Materials 17 (2005) 2411.

[58] J. R. Tumbleston, D.-H. Ko, E. T. Samulski, and R. Lopez, Physical Review B 82 (2010) 205325.

[59] Z. Wu, A. Petzold, T. Henze, T. Thurn-Albrecht, R. H. Lohwasser, M. Sommer, and M. Thelakkat, Macromolecules 43 (2010) 4646.

[60] J. Guo, H. Ohkita, H. Benten, and S. Ito, Journal of the American Chemical Society 132 (2010) 6154.

[61] O. K. Varghese and C. A. Grimes, Solar Energy Materials and Solar Cells 92 (2008) 374.

[62] A. V. Sachenko and I. O. Sokolovskiĭ, Semiconductors 42 (2008) 1219.

[63] J. M. Lobez, T. L. Andrew, V. Bulović, and T. M. Swager, ACS Nano 6 (2012) 3044.

[64] J. Roncali, Macromolecular Rapid Communications 28 (2007) 1761.

[65] P. J. Brown, D. S. Thomas, A. Köhler, J. S. Wilson, J.-S. Kim, C. M. Ramsdale, H. Sirringhaus, and R. H. Friend, Physical Review B 67 (2003) 064203.

[66] Z.-L. Guan, J. B. Kim, H. Wang, C. Jaye, D. A. Fischer, Y.-L. Loo, and A. Kahn, Organic Electronics 11 (2010) 1779.

[67] G. Garcia-Belmonte, A. Munar, E. M. Barea, J. Bisquert, I. Ugarte, and R. Pacios, Organic Electronics 9 (2008) 847.

[68] M. Nirmal and L. Brus, Accounts of Chemical Research 32 (1999) 407.

[69] http://www.volker-quaschning.de/articles/fundamentals3/index.php.

[70] M. T. Winkler, C. R. Cox, D. G. Nocera, and T. Buonassisi, Proceedings of the National Academy of Sciences 110 (2013) E1076.

[71] N.I., National Instruments, 2012.

[72] M. C. Scharber, D. Mühlbacher, M. Koppe, P. Denk, C. Waldauf, A. J. Heeger, and C. J. Brabec, Advanced Materials 18 (2006) 789.

[73] J. J. Loferski, Journal of Applied Physics 27 (1956) 777.

[74] M. Grätzel, Inorganic Chemistry 44 (2005) 6841.

[75] G. Allen, G. Gee, and J. P. Nicholson, Polymer 1 (1960) 56.

[76] H. Vink, European Polymer Journal 12 (1976) 77.

[77] S. H. Yoo, J. M. Kum, and S. O. Cho, Nanoscale Research Letters 6 (2011) 545.

[78] S. E. Shaheen, C. J. Brabec, N. S. Sariciftci, F. Padinger, T. Fromherz, and J. C. Hummelen, Applied Physics Letters 78 (2001) 841.

[79] J. Peet, A. J. Heeger, and G. C. Bazan, Accounts of Chemical Research 42 (2009) 1700.

[80] M. Campoy-Quiles, T. Ferenczi, T. Agostinelli, P. G. Etchegoin, Y. Kim, T. D. Anthopoulos, P. N. Stavrinou, D. D. C. Bradley, and J. Nelson, Nature Materials 7 (2008) 158.

[81] B. A. Collins, E. Gann, L. Guignard, X. He, C. R. McNeill, and H. Ade, The Journal of Physical Chemistry Letters 1 (2010) 3160.

[82] B. A. Collins, J. R. Tumbleston, and H. Ade, The Journal of Physical Chemistry Letters 2 (2011) 3135.

[83] N. D. Treat, M. A. Brady, G. Smith, M. F. Toney, E. J. Kramer, C. J. Hawker, and M. L. Chabinyc, Advanced Energy Materials 1 (2011) 82.

[84] B. Ray, P. R. Nair, and M. A. Alam, Solar Energy Materials and Solar Cells 95 (2011) 3287.

[85] S. S. v. Bavel, M. Bärenklau, G. de With, H. Hoppe, and J. Loos, Advanced Functional Materials 20 (2010) 1458.

[86] S. S. v. Bavel, E. Sourty, G. d. With, and J. Loos, Nano Letters 9 (2008) 507.

[87] J.-H. Huang, K.-C. Li, F.-C. Chien, Y.-S. Hsiao, D. Kekuda, P. Chen, H.-C. Lin, K.-C. Ho, and C.-W. Chu, The Journal of Physical Chemistry C 114 (2010) 9062.

[88] G. Li, Y. Yao, H. Yang, V. Shrotriya, G. Yang, and Y. Yang, Advanced Functional Materials 17 (2007) 1636.

[89] Y. Liang, Z. Xu, J. Xia, S.-T. Tsai, Y. Wu, G. Li, C. Ray, and L. Yu, Advanced Materials 22 (2010) E135.

[90] K. T. Inc., http://www.konarka.com/index.php/site/pressreleasedetail/konarkas_power_plastic_achieves_world_record_83_efficiency_certification_fr, 2010.

[91] X. Gong, M. Tong, F. G. Brunetti, J. Seo, Y. Sun, D. Moses, F. Wudl, and A. J. Heeger, Advanced Materials 23 (2011) 2272.

[92] E. H. Sargent, Nat Photon 3 (2009) 325.

[93] N. Obata, Y. Sato, E. Nakamura, and Y. and Matsuo, Japanese Journal of Applied Physics 50 (2011) 121603.

[94] Y. Hao, X. Yang, M. Zhou, J. Cong, X. Wang, A. Hagfeldt, and L. Sun, ChemSusChem 4 (2011) 1601.

[95] A. Kongkanand, K. Tvrdy, K. Takechi, M. Kuno, and P. V. Kamat, Journal of the American Chemical Society 130 (2008) 4007.

[96] O. E. Semonin, J. M. Luther, S. Choi, H.-Y. Chen, J. Gao, A. J. Nozik, and M. C. Beard, Science 334 (2011) 1530.

[97] J. Gao, J. M. Luther, O. E. Semonin, R. J. Ellingson, A. J. Nozik, and M. C. Beard, Nano Letters 11 (2011) 1002.

[98] R. M. Jain, R. Howden, K. Tvrdy, S. Shimizu, A. J. Hilmer, T. P. McNicholas, K. K. Gleason, and M. S. Strano, Advanced Materials 24 (2012) 4436.

[99] B. R. Saunders and M. L. Turner, Advances in Colloid and Interface Science 138 (2008) 1.

[100] J. E. Brandenburg, X. Jin, M. Kruszynska, J. Ohland, J. Kolny-Olesiak, I. Riedel, H. Borchert, and J. Parisi, Journal of Applied Physics 110 (2011) 064509.

[101] D. Xi, H. Zhang, S. Furst, B. Chen, and Q. Pei, The Journal of Physical Chemistry C 112 (2008) 19765.

[102] S. B. Jo, W. H. Lee, L. Qiu, and K. Cho, Journal of Materials Chemistry 22 (2012) 4244.

[103] J. M. T. Dustin K. James, in Topics in Current Chemistry, Vol. 257, 2005, p. 784.

[104] F. S. Kim, G. Ren, and S. A. Jenekhe, Chemistry of Materials 23 (2010) 682.

[105] C. R. Martin, Accounts of Chemical Research 28 (1995) 61.

[106] J. Tan, L. Jiang, L. He, H. Dong, and W. Hu, Applied Physics Letters 100 (2012) 173902.

[107] N. Haberkorn, J. S. Gutmann, and P. Theato, ACS Nano 3 (2009) 1415.

[108] J. I. Lee, S. H. Cho, S.-M. Park, J. K. Kim, J. K. Kim, J.-W. Yu, Y. C. Kim, and T. P. Russell, Nano Letters 8 (2008) 2315.

[109] S. Lee, G. D. Moon, and U. Jeong, Journal of Materials Chemistry 19 (2009) 743.

[110] M. Bognitzki, H. Hou, M. Ishaque, T. Frese, M. Hellwig, C. Schwarte, A. Schaper, J. H. Wendorff, and A. Greiner, Advanced Materials 12 (2000) 637.

[111] S. Berson, R. De Bettignies, S. Bailly, and S. Guillerez, Advanced Functional Materials 17 (2007) 1377.

[112] H. Xin, F. S. Kim, and S. A. Jenekhe, Journal of the American Chemical Society 130 (2008) 5424.

[113] S. Sun, T. Salim, L. H. Wong, Y. L. Foo, F. Boey, and Y. M. Lam, Journal of Materials Chemistry 21 (2011) 377.

[114] J. Xu, J. Hu, X. Liu, X. Qiu, and Z. Wei, Macromolecular Rapid Communications 30 (2009) 1419.

[115] A. L. Briseno, S. C. B. Mannsfeld, E. Formo, Y. Xiong, X. Lu, Z. Bao, S. A. Jenekhe, and Y. Xia, Journal of Materials Chemistry 18 (2008) 5395.

[116] S. Ren, L.-Y. Chang, S.-K. Lim, J. Zhao, M. Smith, N. Zhao, V. Bulović, M. Bawendi, and S. Gradečak, Nano Letters 11 (2011) 3998.

[117] F. Wang, R. Tang, J. L. F. Kao, S. D. Dingman, and W. E. Buhro, Journal of the American Chemical Society 131 (2009) 4983.

[118] D. A. Schwartz and D. R. Gamelin, (2003) 1.

[119] D. A. Schwartz, N. S. Norberg, Q. P. Nguyen, J. M. Parker, and D. R. Gamelin, Journal of the American Chemical Society 125 (2003) 13205.

[120] I. Lokteva, N. Radychev, F. Witt, H. Borchert, J. r. Parisi, and J. Kolny-Olesiak, The Journal of Physical Chemistry C 114 (2010) 12784.

[121] P. Sarkar and P. S. Nicholson, J. Am. Ceram. Soc. 79 (1996) 1987.

[122] O. O. Van der Biest and L. J. Vandeperre, Annu. Rev. Mater. Sci. 29 (1999) 327.

[123] J. H. Dickerson and A. R. Boccaccini, eds., Electrophoretic Deposition of Nanomaterials, Springer, New York, 2011.

[124] L. Besra and M. Liu, Progr. Mater. Sci. 52 (2007) 1.

[125] S. Jia, S. Banerjee, and I. P. Herman, J. Phys. Chem. C 112 (2008) 162.

[126] S. Banerjee, S. Jia, D. I. Kim, R. D. Robinson, J. Kysar, J. Bevk, and I. P. Herman, Nano Lett. 6 (2006) 175.

[127] S. Jia, S. Banerjee, D. Lee, J. Bevk, J. W. Kysar, and I. P. Herman, J. Appl. Phys. 105 (2009) art. no. 103513.

[128] C. Bullen and P. Mulvaney, Langmuir 22 (2006) 3007.

[129] J. E. B. Katari, V. L. Colvin, and A. P. Alivisatos, J. Phys. Chem. 98 (1994) 4109.

[130] G. Kalyuzhny and R. W. Murray, The Journal of Physical Chemistry B 109 (2005) 7012.

[131] X. Ji, D. Copenhaver, C. Sichmeller, and X. Peng, J. Am. Chem. Soc 130 (2008) 5726.

[132] R. Gomes, A. Hassinen, A. Szczygiel, Q. Zhao, A. Vantomme, J. C. Martins, and Z. Hens, The Journal of Physical Chemistry Letters 2 (2011) 145.

[133] P. J. Flory, The Journal of Chemical Physics 10 (1942) 51.

[134] M. L. Huggins, Journal of the American Chemical Society 86 (1964) 3535.

[135] S. Alexander, J. Phys. France 38 (1977) 983.

[136] M. Manciu and E. Ruckenstein, Langmuir 20 (2004) 6490.

[137] G. N. Greaves, A. L. Greer, R. S. Lakes, and T. Rouxel, Nature Mater. 10 (2011) 823.

[138] E. G. Herbert, W. C. Oliver, and G. M. Pharr, J. Phys. D: Appl. Phys. 41 (2008) 074021.

[139] G. M. Odegard, T. S. Gates, and H. M. Herring, Exp. Mech. 45 (2005) 130.

[140] W. C. Oliver and G. M. Pharr, Journal of Materials Research 7 (1992) 1564.

[141] R. S. Lakes and A. Wineman, Journal of Elasticity 85 (2006) 45.

[142] G. D. Scott, Nature 188 (1960) 908.

[143] G. Y. Onoda and E. G. Liniger, Phys. Rev. Lett. 64 (1990) 2727.

[144] V. M. Huxter, A. Lee, S. S. Lo, and G. D. Scholes, Nano Lett. 9 (2009) 405.

[145] R. M. Christensen, Proc. R. Soc. Lond. A 440 (1993) 461.

[146] L. J. Cohen and O. Ishai, J. Composite Mat. 1 (1967) 390.

[147] J. C. H. Affdl and J. L. Kardos, Polymer Engineering & Science 16 (1976) 344.

[148] J. C. Halpin and J. L. Kardos, Polymer Eng. Sci. 16 (1976) 344.

[149] J. C. Halpin and J. L. Karoos, Polymer Engineering & Science 18 (1978) 496.

[150] D. Lee, S. Jia, S. Banerjee, J. Bevk, I. P. Herman, and J. Kysar, Phys. Rev. Lett. 98 (2007) 0126103.

[151] R. M. Christensen, J. Mech. Phys. Solids 38 (1990) 379.

[152] K. E. Mueggenburg, X. M. Lin, R. H. Goldsmith, and H. M. Jaeger, Nature Mater. 6 (2007) 656.

[153] P. Podsiadlo, G. Krylova, B. Lee, K. Critchley, D. J. Gosztola, D. V. Talapin, P. D. Ashby, and E. V. Shevchenko, J. Am. Chem. Soc., 132 (2010) 8953.

[154] L. B. Freund and S. Suresh, Thin Film Materials: Stress, Defect Formation, and Surface Evolution, Cambridge University Press, Cambridge, 2003.

[155] J. W. Hutchinson and Z. Suo, Adv. Appl. Mech. 29 (1992) 63.

[156] A. Salant, M. Shalom, I. Hod, A. Faust, A. Zaban, and U. Banin, ACS Nano 4 (2010) 5962.

[157] T. J. Kramer, S. K. Kumar, M. L. Steigerwald, and I. P. Herman, The Journal of Physical Chemistry B 117 (2012) 1537.

[158] J. Asua, Polymer Reaction Engineering, Wiley, 2007.

[159] J.-D. Cho, H.-T. Ju, and J.-W. Hong, Journal of Polymer Science Part A: Polymer Chemistry 43 (2005) 658.

[160] P. J. Flory, Principles of Polymer Chemistry, Cornell University Press, Ithaca, 1953.

[161] K. G. Budinski and M. K. Budinski, Engineering Materials: Properties and Selection, Prentice Hall PTR, 2010.

[162] H. S. Fogler and M. N. Gurmen, University of Michigan, 2013.

[163] D. I. Bower, An Introduction to Polymer Physics, Cambridge University Press, 2002.

[164] C. D. Han and B. F. Goodrich, Rheology and Processing of Polymeric Materials, Oxford University Press, 2007.

[165] O. Ozer, A. Ince, B. Karagoz, and N. Bicak, Desalination 309 (2013) 141.

[166] M. E. Dokukin and I. Sokolov, Macromolecules 45 (2012) 4277.

[167] IAS, Indian Academy of Science, 2003.

[168] J. Hay and E. Herbert, Experimental Techniques 37 (2013) 55.

[169] E. G. Herbert, W. C. Oliver, and G. M. Pharr, Journal of Physics D: Applied Physics 41 (2008) 074021.

[170] R. Foschia and M. Jobin, Journal of Physics: Conference Series 61 (2007) 307.

[171] L. H. Sperling, Introduction to Physical Polymer Science, Wiley, 2005.

[172] P. J. Flory, Principles of Polymer Chemistry, Cornell University Press, Ithaca, 1970.

[173] F. Bai, X. Yang, and W. Huang, Macromolecules 37 (2004) 9746.

[174] Z. Xu, L. Yang, and Q. Wang, Journal of Chromatography A 1216 (2009) 3098.

[175] H. P. Gregor, F. Gutoff, and J. I. Bregman, Journal of Colloid Science 6 (1951) 245.

[176] S. Balog, U. Gasser, K. Mortensen, H. Ben youcef, L. Gubler, and G. G. Scherer, Polymer 53 (2012) 175.

[177] B. P. Tripathi and V. K. Shahi, Progress in Polymer Science 36 (2011) 945.

[178] V. M. Huxter, A. Lee, S. S. Lo, and G. D. Scholes, Nano Letters 9 (2008) 405.

[179] S. C. Tan, Stress Concentrations in Laminated Composities, Technomic Publishing Company, 1994.

[180] B. A. M. Venhoven, A. J. de Gee, and C. L. Davidson, Biomaterials 14 (1993) 871.

[181] L. B. Freund and S. Suresh, Thin Film Materials: Stress, Defect Formation and Surface Evolution, Cambridge University Press, 2003.

[182] C. Chen, R. S. Justice, D. W. Schaefer, and J. W. Baur, Polymer 49 (2008) 3805.

[183] J. T. Han and K. Cho, Journal of Materials Science 41 (2006) 4239.

[184] Y. Shengyi, Z. Na, Z. Li, Z. Haizheng, L. Ruibin, and Z. Bingsuo, Nanotechnology 23 (2012) 255203.

[185] Y. Liang, Z. Xu, J. Xia, S.-T. Tsai, Y. Wu, G. Li, C. Ray, and L. Yu, Adv. Mater. 22 (2010) E135.

[186] X. Gong, M. Tong, F. G. Brunetti, J. Seo, Y. Sun, D. Moses, F. Wudl, and A. J. Heeger, Adv. Mater. 23 (2011) 2272.

[187] E. H. Sargent, Nature Photon. 3 (2009) 325.

[188] N. Obata, Y. Sato, E. Nakamura, and Y. and Matsuo, Japanese J. Appl. Phys. 50 (2011) 121603.

[189] A. Kongkanand, K. Tvrdy, K. Takechi, M. Kuno, and P. V. Kamat, J. Am. Chem. Soc. 130 (2008) 4007.

[190] J. Gao, J. M. Luther, O. E. Semonin, R. J. Ellingson, A. J. Nozik, and M. C. Beard, Nano Lett. 11 (2011) 1002.

[191] J. E. Brandenburg, X. Jin, M. Kruszynska, J. Ohland, J. Kolny-Olesiak, I. Riedel, H. Borchert, and J. Parisi, J. Appl. Phys. 110 (2011) 064509.

[192] N. C. Greenham, X. Peng, and A. P. Alivisatos, Phys. Rev. B 54 (1996) 17628.

[193] B. R. Saunders and M. L. Turner, Adv. Coll. Int. Sci. 138 (2008) 1.

[194] D. Xi, H. Zhang, S. Furst, B. Chen, and Q. Pei, J. Phys. Chem. C 112 (2008) 19765.

[195] J. R. Tumbleston, D.-H. Ko, E. T. Samulski, and R. Lopez, Phys. Rev. B 82 (2010) 205325.

[196] S. B. Jo, W. H. Lee, L. Qiu, and K. Cho, J. Mater. Chem. 22 (2012) 4244.

[197] D. K. James and J. M. Tour, in Top. Current Chem., Vol. 257, 2005, p. 33.

[198] F. S. Kim, G. Ren, and S. A. Jenekhe, Chem. Mater. 23 (2010) 682.

[199] S. S. van Bavel, M. Bärenklau, G. de With, H. Hoppe, and J. Loos, Adv. Funct. Mater. 20 (2010) 1458.

[200] S. S. van Bavel, E. Sourty, G. de With, and J. Loos, Nano Lett. 9 (2009) 507.

[201] T. Schiros, S. Mannsfeld, C.-Y. Chiu, K. G. Yager, J. Ciston, A. A. Gorodetsky, M. Palma, Z. Bullard, T. Kramer, D. M. DeLongchamp, D. A. Fischer, I. Kymissis, M. F. Toney, and C. Nuckolls, Adv. Funct. Mater. 22 (2012) 1167.

[202] W. C. Tsoi, P. G. Nicholson, J. S. Kim, D. Roy, T. L. Burnett, C. E. Murphy, J. Nelson, D. D. C. Bradley, J.-S. Kim, and F. A. Castro, Energy & Environment. Sci. 4 (2011) 3646.

[203] M. Campoy-Quiles, T. Ferenczi, T. Agostinelli, P. G. Etchegoin, Y. C. Kim, T. D. Anthopoulos, P. N. Stavrinou, D. D. C. Bradley, and J. Nelson, Nature Mater. 7 (2008) 158.

[204] J. S. Kim, J. H. Lee, J. H. Park, C. Shim, M. Sim, and K. Cho, Adv. Functional Mater. 21 (2011) 480.

[205] W. Ma, C. Yang, X. Gong, K. Lee, and A. J. Heeger, Adv. Functional Mater. 15 (2005) 1617.

[206] J. Peet, J. Y. Kim, N. E. Coates, W. L. Ma, D. Moses, A. J. Heeger, and G. C. Bazan, Nature Mater. 6 (2007) 497.

[207] N. D. Treat, M. A. Brady, G. Smith, M. F. Toney, E. J. Kramer, C. J. Hawker, and M. L. Chabinyc, Adv. Energy Mater. 1 (2011) 82.

[208] R.-Q. Png, P.-J. Chia, J.-C. Tang, B. Liu, S. Sivaramakrishnan, M. Zhou, S.-H. Khong, H. S. O. Chan, J. H. Burroughes, L.-L. Chua, R. H. Friend, and P. K. H. Ho, Nature Mater. 9 (2010) 152.

[209] P. Sonar, J. P. Fong Lim, and K. L. Chan, Energy & Environment. Sci. 4 (2011) 1558.

[210] N. C. Cates, R. Gysel, Z. Beiley, C. E. Miller, M. F. Toney, M. Heeney, I. McCulloch, and M. D. McGehee, Nano Lett. 9 (2009) 4153.

[211] C. R. Martin, Acc. Chem. Res. 28 (1995) 61.

[212] J. H. Tan, L. Jiang, L. F. He, H. L. Dong, and W. P. Hu, Appl. Phys. Lett. 100 (2012)

[213] J. I. Lee, S. H. Cho, S.-M. Park, J. K. Kim, J. K. Kim, J.-W. Yu, Y. C. Kim, and T. P. Russell, Nano Lett. 8 (2008) 2315.

[214] S. Lee, G. D. Moon, and U. Jeong, J. Mater. Chem. 19 (2009) 743.

[215] M. Bognitzki, H. Hou, M. Ishaque, T. Frese, M. Hellwig, C. Schwarte, A. Schaper, J. H. Wendorff, and A. Greiner, Adv. Mater. 12 (2000) 637.

[216] S. Berson, R. De Bettignies, S. Bailly, and S. Guillerez, Adv. Funct. Mater. 17 (2007) 1377.

[217] H. Xin, F. S. Kim, and S. A. Jenekhe, J. Am. Chem. Soc. 130 (2008) 5424.

[218] S. Sun, T. Salim, L. H. Wong, Y. L. Foo, F. Boey, and Y. M. Lam, J. Mater. Chem. 21 (2011) 377.

[219] J. Xu, J. Hu, X. Liu, X. Qiu, and Z. Wei, Macromolecular Rapid Comm. 30 (2009) 1419.

[220] A. L. Briseno, S. C. B. Mannsfeld, E. Formo, Y. Xiong, X. Lu, Z. Bao, S. A. Jenekhe, and Y. Xia, J. Mater. Chem. 18 (2008) 5395.

[221] S. Ren, L.-Y. Chang, S.-K. Lim, J. Zhao, M. Smith, N. Zhao, V. Bulović, M. Bawendi, and S. Gradečak, Nano Lett. 11 (2011) 3998.

[222] L. Qiu, J. A. Lim, X. Wang, W. H. Lee, M. Hwang, and K. Cho, Advanced Materials 20 (2008) 1141.

[223] L. Qiu, J. A. Lim, X. Wang, W. H. Lee, M. Hwang, and K. Cho, Adv. Mater. 20 (2008) 1141.

[224] R. N. Wenzel, J. Phys. Coll. Chem. 53 (1948) 1466.

[225] A. B. Cassie and S. Baxter, Trans. Far. Soc. (1944) 546.

[226] M. Miwa, A. Nakajima, A. Fujishima, K. Hashimoto, and T. Watanabe, Langmuir 16 (2000) 5754.

[227] S. Pal and A. K. Nandi, Macromolecules 36 (2003) 8426.

[228] R. J. Kline, D. M. DeLongchamp, D. A. Fischer, E. K. Lin, L. J. Richter, M. L. Chabinyc, M. F. Toney, M. Heeney, and I. McCulloch, Macromolecules 40 (2007) 7960.

[229] K. H. Lee, P. E. Schwenn, A. R. G. Smith, H. Cavaye, P. E. Shaw, M. James, K. B. Krueger, I. R. Gentle, P. Meredith, and P. L. Burn, Adv.Mater. 23 (2011) 766.

[230] B.-Y. Yu, W.-C. Lin, W.-B. Wang, S.-I. Iida, S.-Z. Chen, C.-Y. Liu, C.-H. Kuo, S.-H. Lee, W.-L. Kao, G.-J. Yen, Y.-W. You, C.-P. Liu, J.-H. Jou, and J.-J. Shyue, ACS Nano 4 (2010) 833.

[231] M. D. Heinemann, K. Ananthanarayanan, L. N. S. A. Thummalakunta, C. H. Yong, and J. M. Luther, Green 1 (2011) 291.

[232] B. A. Collins, J. R. Tumbleston, and H. Ade, J. Phys. Chem. Lett. 2 (2011) 3135.

[233] B. A. Collins, E. Gann, L. Guignard, X. He, C. R. McNeill, and H. Ade, J. Phys. Chem. Lett. 1 (2010) 3160.

[234] L. G. Kaake, P. F. Barbara, and X. Y. Zhu, J. Phys. Chem. Lett. 1 (2010) 628.

[235] R. C. I. MacKenzie, T. Kirchartz, G. F. A. Dibb, and J. Nelson, J. Phys. Chem. C 115 (2011) 9806.

[236] S. R. Cowan, N. Banerji, W. L. Leong, and A. J. Heeger, Adv. Funct. Mater. 22 (2012) 1116.

[237] L. G. Kaake, P. F. Barbara, and X. Y. Zhu, The Journal of Physical Chemistry Letters 1 (2010) 628.

[238] R. C. I. MacKenzie, T. Kirchartz, G. F. A. Dibb, and J. Nelson, The Journal of Physical Chemistry C 115 (2011) 9806.

[239] N. Radychev, I. Lokteva, F. Witt, J. Kolny-Olesiak, H. Borchert, and J. Parisi, J. Phys. Chem. C 115 (2011) 14111.

[240] N. C. Anderson and J. S. Owen, Chemistry of Materials 25 (2012) 69.

[241] O. Inganas, Nat Photon 5 (2011) 201.

[242] D. Josell, C. R. Beauchamp, S. Jung, B. H. Hamadani, A. Motayed, L. J. Richter, M. Williams, J. E. Bonevich, A. Shapiro, N. Zhitenev, and T. P. Moffat, Journal of The Electrochemical Society 156 (2009) H654.

[243] J. Zou, H.-L. Yip, S. K. Hau, and A. K.-Y. Jen, Applied Physics Letters 96 (2010) 203301.

[244] K. Tvingstedt and O. Inganäs, Advanced Materials 19 (2007) 2893.

[245] S. Sorgenfrei, I. Meric, S. Banerjee, A. Akey, S. Rosenblatt, I. P. Herman, and K. L. Shepard, Applied Physics Letters 94 (2009) 053105.

[246] M. Albota, D. Beljonne, J.-L. Brédas, J. E. Ehrlich, J.-Y. Fu, A. A. Heikal, S. E. Hess, T. Kogej, M. D. Levin, S. R. Marder, D. McCord-Maughon, J. W. Perry, H. Röckel, M. Rumi, G. Subramaniam, W. W. Webb, X.-L. Wu, and C. Xu, Science 281 (1998) 1653.

[247] N. Hammer, T. Emrick, and M. Barnes, Nanoscale Research Letters 2 (2007) 282

[248] R. C. Severance, E. S. Rountree, M. D. Smith, and H.-C. zur Loye, Solid State Sciences 14 (2012) 1512.

[249] Y. Park and R. C. Advincula, Chemistry of Materials 23 (2011) 4273.

[250] Y. Zhang, Y. Chen, H. Niu, and M. Gao, Small 2 (2006) 1314.

[251] H. Skaff, K. Sill, and T. Emrick, Journal of the American Chemical Society 126 (2004) 11322.

[252] J. M. Kroon, N. J. Bakker, H. J. P. Smit, P. Liska, K. R. Thampi, P. Wang, S. M. Zakeeruddin, M. Grätzel, A. Hinsch, S. Hore, U. Würfel, R. Sastrawan, J. R. Durrant, E. Palomares, H. Pettersson, T. Gruszecki, J. Walter, K. Skupien, and G. E. Tulloch, Progress in Photovoltaics: Research and Applications 15 (2007) 1.

[253] G. I. Koleilat, L. Levina, H. Shukla, S. H. Myrskog, S. Hinds, A. G. Pattantyus-Abraham, and E. H. Sargent, ACS Nano 2 (2008) 833.